# Design and Testing of a Novel Neutron Survey Meter


Matthew James Ian Balmer

Department of Engineering

University of Lancaster

A thesis submitted for the degree of

*Doctor of Philosophy*

1 February 2016

For my daughter.

# Acknowledgements

I would like to thank my industrial supervisor Graeme Taylor. The idea of this project was born with Graeme and I have been constantly encouraged by his belief in this idea. Never forceful, Graeme has provided me with guidance, encouragement and support, for which I am very grateful. I would like to thank my academic supervisor, Kelum Gamage. In particular for his unwavering enthusiasm, being responsive and providing reassurance throughout the course of this project.

I would like to thank colleagues and friends in the Engineering Department, in particular; Jonathan Beaumont, Ashley Jones, Alex Grievson, Sarah Jackson, Bethany Colling and Helen Parker.

I am indebted to my parents for their guidance and help. Without my wife I would never have had the courage to begin this PhD. To my daughter, your smile is the greatest encouragement I could ever need.

I gratefully acknowledge financial support from the Engineering and Physical Sciences Research Council (EPSRC), the National Physical Laboratory and the Department of Engineering, Lancaster University.

Finally, a principle that has remained at the forefront of my mind for the entirety of this research:-

*"The first principle is that you must not fool yourself - and you are the easiest person to fool"* - Richard P. Feynman.

# Abstract

This thesis reports on the development of an instrument which can estimate the effective dose of a neutron field, accounting for both direction and energy of the field. This work represents a novel, real-time, approach to workplace directional neutron dosimetry.

A $^{6}$Li-loaded scintillator based detector system was developed. This detector system was then used to perform neutron assays at a number of locations in a water phantom. The $^{6}$Li-loaded plastic scintillator which was used in this research was sensitive to both gamma and neutron fields. Experimental data were obtained for a number of neutron fields and a comparative analysis of three pulse shape discrimination techniques was performed. A novel technique was identified to perform simultaneous thermal and fast neutron assays using this detector system. The importance of these techniques extends beyond the instrument in this work, and is an important step forward in the identification of a replacement for $^{3}$He detectors in neutron detection applications.

The variation in thermal and fast neutron response to different energies and field directions was exploited. The modelled response of the instrument to various neutron fields was used to train an artificial neural network (ANN). Experimental results were obtained for a number of radionuclide source based neutron fields to test the performance of the system. The results of experimental neutron assays at 25 locations in a 20x20x17.5 cm$^{3}$ water phantom were fed into the trained ANN. A correlation between neutron counting rates in the phantom and neutron fluence rates was experimentally found. The resulting estimates of effective dose rate differed by 45% or less from the calculated dose value, regardless of energy distribution or direction. The ANN was also trained to learn ambient dose equivalent and the resulting ambient dose equivalent rate for the experimental results was found to be 60% or less for the 14 experimental fields investigated. All the experimental measurements were carried out at the low scatter facility at the National Physical Laboratory (NPL), London, UK. It is believed that in the research presented in this thesis, for the first time, a single instrument has been able to estimate effective dose in real-time.

Prior to the work described above, an instrument based on a single loaded liquid scintillator was also studied in this research. By observing the distribution of light

collected from a number of neutron captures in a loaded scintillator, an ANN was trained to estimate the effective dose of the field. A number of difficulties must still be overcome to realise this second instrument studied. The primary difficulty being detecting and localising neutron capture within the scintillator.

# Declarations

I, Matthew James Ian Balmer, hereby certify that this thesis has been written by me and has not been submitted in any previous application for a higher degree. The work presented here was carried out at the University of Lancaster between February 2013 and February 2016. It must be noted that Matthew J.I. Balmer contributed ideas to the work described in chapter 8, section 8.3.2. However, the simulations were performed by Graeme C. Taylor at the National Physical Laboratory.

Signed .....

Date .....

I, Doctor Kelum Asanga Akurugoda Gamage, hereby certify that the candidate has fulfilled the conditions of the resolution and regulations appropriate for the degree of Doctor of Philosophy in the University of Lancaster and that the candidate is qualified to submit this thesis in application for that degree.

Signed .....

Date .....

# Contents

# List of Figures

# List of Tables

# Chapter 1

# Introduction

Human exposure to ionising radiation is a health risk which radiation protection practices attempt to reduce. Depending on the type of ionising radiation, a differing risk is experienced. Therefore, the dose from each type of radiation (such as gamma, neutron, beta) should be considered when assessing this risk. The calculation and assessment of these risks is described by the term radiation dosimetry. The need for neutron dosimetry spans across a number of nuclear sectors.

In 1956, the United Kingdom (UK) pioneered the world's first civil nuclear power station, and currently, around 18% of the UK's electricity production comes from nuclear power [1]. Presently, the UK remains committed to nuclear power. In 2015, it was announced that Hinkley C, the first of a series of planned nuclear new-builds, was expected to be producing electricity by 2023 [2]. Beyond the UK, the World Nuclear Association lists 29 countries worldwide which produced electricity from nuclear power in 2014 [3]. Within the UK, the Ionising Radiations Regulations 1999 states it must be ensured that ionising radiation is adequately monitored in controlled or supervised areas within these plants, using suitable and sufficient equipment [4]. Thus, it is clear that within these nuclear facilities there is a need to monitor, understand and control the risks associated with the everyday exposure experienced by nuclear workers.

Radiation dosimetry is of great importance in the aftermath of nuclear disasters and incidents. On Friday 11 March 2011, a major earthquake occurred off the coast of Japan. The ensuing tsunami and the following chain of events, led to a disaster at the Fukushima Daiichi nuclear power plant on the east coast of Japan. Following the

release of radioactive materials into the air, members of the public living within 30 km of the site were evacuated from their homes. Radiation dosimetry instruments were used to aid these decisions [5]. Alongside the Chernobyl (Ukraine) disaster in 1986, the Fukushima disaster is widely considered to be one of the most serious nuclear accidents to have ever occurred. The long term health effects to the public within this area are still unknown, however, dose measurements performed in the aftermath will no doubt aid future studies on this matter.

The use of ionising radiation in cancer treatments means that there is also a need for neutron dosimetry in medical facilities. An example of such treatment is boron neutron capture therapy. This uses a focussed low energy neutron beam to target tumours loaded with a boron agent. Other higher energy ionising radiation treatments also exist. In October 2014, planning permission was granted for the build of The Christie Proton Beam Therapy Centre [6], Manchester, UK. Secondary neutrons as a result of high energy hadron interactions will likely demand neutron dosimetry assessment within these facilities [7].

It can be seen that there is a wide ranging need to monitor and understand the risk associated with neutron exposure. In the next section, some of the deficiencies of the existing neutron dosimetry instruments and methods are discussed.

## 1.1 Current deficiencies

In neutron dosimetry, the overall risk to the human body is classified as the sum of the risks to individual tissue/organs. However, when considering males and females, they have a different overall risk weighting due to anatomical differences. Neutron radiation exposure risk to a human is a complex problem to quantify. Considering these factors, from an instrumentation standpoint, estimating the risk for a specific individual is a difficult task, if not currently impossible.

Existing neutron dosimetry instruments measure the quantity *ambient dose equivalent* (*H*(10)*). The quantity is supposed to estimate the human health risk due to exposure to a neutron field, in a conservative manner. That is, the quantity does not account for the direction of the neutron field (unlike the protection quantity, *effective dose (E)*). The response of *H*(10)* against energy follows a non-linear trend. A number of commercial instruments to measure *H*(10)* were examined in a study

by the Health Protection Agency, UK [8]. The response of these instruments to the *H*(10)* response was shown to vary depending on the energy and directional distribution of the neutron field. In these situations, it is therefore important to understand how well the instrument provides a conservative estimate of the protection quantity. The most accurate method of performing area dosimetry is the method of detecting thermal neutrons within a range of hydrogenous moderators, known as a Bonner Sphere Spectrometer (BSS) system. It is a well-established technique for neutron spectroscopy and the response of this instrument has been well-characterised [9]. Combining this response with unfolding techniques, reasonably reliable neutron spectroscopy can be achieved. However, the time consuming nature and complexity of taking such field measurements make it counterproductive. This technique also does not permit real-time neutron surveys to be achieved.

It is important that personal dosimetry methods are also a conservative estimate of the protection quantity. In some cases, area survey measurements are used to improve the accuracy of these personal dosimetry methods [10]. The 'Evaluation of Individual Dosimetry in Mixed Neutron and Photon Radiation Fields' (EVIDOS) project investigated the effectiveness of personal dosimetry instruments in workplace fields [11]. In this study both energy and direction dependence of the field were considered. Two directional neutron dosimetry instruments were developed during this project. The first was a telescope design directional neutron spectrometer [12], the second a directional spectrometer which could be likened to a collection of personal dose meters around a phantom [13]. For optimal results, prior information on the energy spectrum under investigation was required to aid the unfolding process [11]. This presents challenges when working in an unknown field where an instrument such as a Bonner Sphere Spectrometer system is not available. This restricts the instruments usage as a true real-time neutron dosimetry meter.

A number of neutron area survey instruments use $^{3}$He based neutron detectors, this is due to its high thermal neutron sensitivity [14, 15, 8]. In the aftermath of the terrorists attacks of September 11, 2011, there was a surge in deployment of $^{3}$He detectors for homeland security. This, combined with an increase use of $^{3}$He for medical imaging, led to a global shortage of $^{3}$He [16]. Dwindling $^{3}$He stocks mean that there is an ever present need to identify alternatives for these detectors [17].

Ignoring the deficiencies of existing instruments, a pitfall is apparent, with regard

to *H*(10)*. When estimating the health risk of exposure to neutron fields, the term *Effective Dose* can be used [18]. Using this quantity, the risk estimate accounts for both the energy distribution and direction of incidence of a neutron field. Effective dose is calculated from a number of averaged parameters (sex, body shapes, age etc.). This non-isotropic quantity cannot be measured, only estimated. Hence, the use of *H*(10)* for neutron area survey measurements. However, the current UK industry values for *H*(10)* are not always more conservative than the effective dose [19]. Hence, in some energy regions the operational quantity is less conservative than the quantity deemed inappropriate for operational dosimetry (by the International Commission on Radiological Protection).

## 1.2 Novel digital approach to neutron dosimetry

The overall aim of the research presented in this thesis was to design and test a novel neutron survey meter that takes account of both neutron energy and direction, in order to provide an estimate of effective dose. Throughout the research, the focus was a design that was capable of being portable and able to estimate the effective dose of workplace neutron fields in real-time.

The instrument designed and built consisted of a two linear rails and actuators to move a neutron detector within a 20x20x17.5 $cm^3$ water phantom. An automated control system was developed to move the detector to 25 locations within the phantom. At each of these locations, the signals from the detector were processed by a bespoke field-programmable gate array (FPGA) based pulse digitiser system developed in this research. These digitised signals were then processed using novel neutron assay algorithms developed in this research. The variation in thermal and fast neutron response (across the water phantom) to different energies and field directions was then exploited. The modelled response of the instrument to various neutron fields was used to train an artificial neural network (ANN) to learn the effective dose and ambient dose equivalent of these fields.

Effective dose is not recommended for operational neutron dosimetry. However, in the absence of a more suitable directional dosimetry standard, it has been used in this research. One of the more salient features of the instrument is that the response lies in software. If the present ICRP74 dose conversion factors were ever

to change then existing neutron area survey meters would require re-designing as their response is a function of the hardware. However, with this instrument, if new dosimetry standards were proposed, no modifications to the hardware would be necessary.

All experimental data presented in this work were measured at the National Physical Laboratory (NPL) in Teddington, London, UK. The experimental measurements were compared against, well understood, prior measurements and models of the low-scatter facility within NPL. For all fields, the resulting estimates of effective dose rate differed by 45% or less from the calculated dose value, regardless of energy distribution or direction for measurement times greater than 25 minutes. For the same experimental fields, the estimate of ambient dose equivalent was found to be 60% or better.

A novel technique has been developed to perform thermal neutron assay in mixed radiation fields, using current state-of-the-art, $^{6}$Li plastic scintillators. These scintillators are sensitive to gamma radiation, fast and thermal neutrons. Using pulse shape discrimination (PSD) techniques, it is possible to attempt to classify an event as a gamma or neutron interaction. However, thermal neutron signals were found to be located within the fast neutron region. Pulse shape discrimination techniques were not sufficient to classify thermal neutron detections. In this research a new technique for thermal assay was developed to remove the fast neutron background count within the pulse-height range of detected thermal neutrons. The total integral of the neutron pulse-height spectrum was removed from an estimated fit of a fast neutron only pulse-height spectrum. This subtraction produced the thermal neutron assay.

With liquid scintillators, such as BC-501A, excellent neutron/gamma separation is observed and a line of separation on a PSD scatter plot is sufficient to classify these events [20]. Typically, neutron and gamma pulse shape variations for a given pulse height, follow a Gaussian distribution. However, as the quality of separation between neutron and gamma interactions reduces, these Gaussian regions overlap. Three algorithms for discriminating between fast neutrons, thermal neutrons and gamma rays in a $^{6}$Li-loaded plastic scintillator were compared. All three methods resulted in overlapping neutron and gamma Gaussian regions. With only a line of separation for event classification, in high gamma fluence environments this can lead to an over

estimate of the neutron fluence with non-ideal neutron/gamma separation. In this research a statistical technique, Gaussian mixtures model, was used to perform fast neutron assay.

The algorithms described for fast and thermal neutron assay were extensively tested and validated in the work presented in chapter 8. A good agreement between computer modelled and experimental neutron assays was observed using these algorithms. This can be found in section 8.4.1. The algorithms are such that after calibration, no user input is required. The algorithms lend themselves well to implementation into a portable real-time neutron detection systems. Scintillators for thermal neutron detection such as $Cs_2LiYCl_6$:Ce (CLYC) and $^{10}$B-loaded plastic scintillators appear to be suitable to use this technique for fast and thermal neutron assay [21, 22]. The importance of these techniques extends beyond the instrument in this work, and is an important step forward in the identification of a replacement for $^3$He detectors in neutron detection applications.

In summary, a novel neutron survey meter has been designed, built and tested. The instrument has the potential to provide a much needed, greater understanding of the directional properties of workplace neutron fields. This will greatly improve the understanding of the risk associated with neutron exposure.

## 1.3 Awards

Dean's award for excellence in PhD studies, Faculty of Science and Technology, Lancaster University, UK, December 2015.

## 1.4 Peer-reviewed journal publications

1. *M.J.I. Balmer, K.A.A. Gamage, and G.C. Taylor. A novel approach to neutron dosimetry.* In submission.

2. *M.J.I. Balmer, K.A.A. Gamage, and G.C. Taylor. Neutron assay in mixed radiation fields with a $^6$Li-loaded plastic scintillator.* Journal of Instrumentation. 10(08):P08012-1-14, August 2015.

3. *M.J.I. Balmer, K.A.A. Gamage, and G.C. Taylor. Comparative analysis of pulse shape discrimination methods in a $^{6}$Li-loaded plastic scintillator.* Nuclear Instruments and Methods in Physics Research Section A Accelerators, Spectrometers, Detectors and Associated Equipment. 788:146-153, July 2015.

4. *M.J.I. Balmer, K.A.A. Gamage, and G.C. Taylor. Detecting energy dependent neutron capture distributions in a liquid scintillator.* Nuclear Instruments and Methods in Physics Research Section A Accelerators, Spectrometers, Detectors and Associated Equipment. 776:1-7, March 2015.

5. *M.J.I. Balmer, K.A.A. Gamage, and G.C. Taylor. An investigation into a suitable scintillator for localising neutron capture within a detector.* Journal of Instrumentation, 9(01):P01007-1-13, January 2014.

6. *M.J.I. Balmer, K.A.A. Gamage, and G.C. Taylor. Critical review of directional neutron survey meters.* Nuclear Instruments and Methods in Physics Research Section A Accelerators, Spectrometers, Detectors and Associated Equipment. 735:7-11, January 2014

## 1.5 Conferences and meetings

- *Using artificial intelligence to estimate neutron dose.* Christmas Conference, Faculty of Science and Technology, Lancaster University. 15 December 2015.
- *Design and test of an instrument for directional neutron dosimetry..* Neutron Users Club at the National Physical Laboratory, Teddington, London. 20 October 2015.
- *Development of a directional neutron survey meter.* Neutron Users Club at the National Physical Laboratory, Teddington, London. 30 September 2014.
- *Directional neutron dosimetry.* Christmas Conference, Faculty of Science and Technology, Lancaster University. 17 December 2013.
- *A comparison of Geant4 and MCNP for modelling liquid scintillators.* Neutron Users Club at the National Physical Laboratory, Teddington, London. 16 October 2013.

- *Critical review of directional neutron survey meters.* IEEE ANIMMA 2013, Marseilles, France. 23-27 June 2013

## 1.6 Definitions of terms used in this research

In this research, where the term error is used it describes the difference between the measured value and the 'true value' of the thing being measured [23]. To quantify this error, this has sometimes been expressed as a percentage difference as described in Equation 1.1 below.

$$Error = \frac{|Measured\ Value - True\ Value|}{|True\ Value|} \times 100 \tag{1.1}$$

The term uncertainty is defined as 'a quantification of the doubt about the measurement result' [23].

## 1.7 Outline of each chapter

- **Chapter 2**. This chapter provides the underpinning science of the research discussed in this thesis. These introductory topics include: interactions of radiation with materials, neutron dosimetry and methods of neutron detection.

- **Chapter 3**. This chapter documents a literary review which was performed to identify the existing research and technologies within the topic of directional area dosimetry. Instruments which could be adapted for use as directional neutron survey meters were also considered within this review. Possible adaptations to these instruments were suggested with a view to improving the portability of the instruments.

- **Chapter 4**. One of the most promising instruments reviewed in chapter 3 was a novel theoretical design for an instrument potentially capable of estimating effective dose. However in the theoretical design a number of unresearched areas needed further investigation. In this chapter, two Monte Carlo computer codes were compared to validate the design principles of this instrument. Following Monte Carlo modelling, it was concluded that for this

research, a lithium-loaded scintillator was the most promising of the detectors investigated.

- **Chapter 5**. This chapter describes a novel technique to estimate effective dose based upon light intensity from neutron capture events at a number of locations in a detector. Using back propagation Artificial Neural Networks (ANN) the energy and incident direction of the neutron field was predicted from the distribution of neutron captures within a $^{6}$Li-loaded scintillator.

- **Chapter 6**. Three algorithms for discriminating between fast neutrons, thermal neutrons and gamma rays in a $^{6}$Li-loaded plastic scintillator were compared. The performance of the charge comparison method, triangular filtering and frequency gradient analysis were investigated. All three methods were found to perform similarly in terms of neutron/gamma separation.

- **Chapter 7**. This chapter described a novel technique to perform thermal and fast neutron assay with a $^{6}$Li-loaded plastic scintillator. The technique was compared against an existing thermal neutron technique, capture gating. The new technique developed was found to have many advantages over capture gating.

- **Chapter 8**. The design, build and test of a novel directional neutron survey meter is described in this chapter. Using the algorithms developed in chapter 7 and utilising the principles of ANNs discussed in the chapter 5, a new instrument was designed. Experimental data were collected at the National Physical Laboratory (NPL) in Teddington, London, UK. For all fields, the resulting estimates of effective dose rate differed by 45% or less from the calculated dose value, regardless of energy distribution or direction for measurement times greater than 25 minutes.

- **Chapter 9**. A summary of the research and possible future directions of the work are presented in this chapter.

# Chapter 2

# Background

This chapter provides background information on interactions of radiation with materials, neutron dosimetry and methods of neutron detection.

## 2.1 Interaction of radiation with materials

### 2.1.1 Charged particles

A charged particle with a mass greater than that of the resting mass of an electron can be described as a heavy charged particle. Heavy particles, such as an alpha ($^4$He), interact primarily with the electrons of a target atom. The heavy, positively charged, particle is attracted to the orbiting, negatively charged, electrons in the target atom. This is known as Coulomb force attraction. The resulting impulse experienced by the electron in the target atom, can result in either raising the electron to a higher energy state (*excitation*) or the electron may be stripped from the atom (*ionisation*). The energy loss of the alpha particle in each individual collision is small. However, the rate of energy loss over its track length *(dE/dx)* is high. This is described by the approximation of the Bethe formula for an alpha particle, shown in Equation 2.1.

$$-\frac{dE}{dx} = \frac{4\pi e^4 z_e^2}{m_0 v^2} NB \tag{2.1}$$

where

$$B = Z\left[ln\frac{2m_0v^2}{I} - ln\left(1 - \frac{v^2}{c^2}\right) - \frac{v^2}{c^2}\right] \tag{2.2}$$

where $z_e$ is the charge of the charged particle with velocity $v$, $N$ and $Z$ are the number density and atomic number of the absorber atoms, $m_0$ is the resting mass of the electron with charge $e$, $I$ is the average excitation and ionisation potential of the absorber atom and $c$ is the speed of light.

All the particle energies of interest in this research are non-relativistic energies. That is, their velocities are much less than the speed of light and relativistic effects are considered negligible. For different particle masses, different rates of energy loss over the particle track length occurs. Therefore, an alpha will lose more energy over a given track length compared to a proton.

The most likely form of interaction for an electron is repulsion from a target atom via the Coulomb force between the atom electrons and the free electron. When compared to a heavy charged particle, the rate of energy loss is much lower. Scattering of the electron means that its path is likely to change direction frequently whilst travelling through a material. Another form of energy loss can occur over the path known as bremsstrahlung which is energy loss via electromagnetic radiation.

The assay of charged particles is not a primary motivation of this research. However, an uncharged particle (for example, a neutron or photon) interaction with matter is usually detected by means of a secondary charged particle.

### 2.1.2 Gamma interactions

A photon is a massless, uncharged, quantum of energy in the form of electromagnetic radiation, whose energy can be described by Equation 2.3.

$$E = hf \tag{2.3}$$

where $h$ is Planck's constant, 6.626x10$^{-34}$ J s, $f$ is the frequency (Hz) and $E$ is the energy of the photon. This is such that, the lower the frequency of the photon, the lower the energy of the photon. When discussing such low energies of particles and quanta, the electron volt (eV) is used (1.60217657x10$^{-19}$). This is the amount of energy gained (or lost) by the charge of a single electron moved across an electric

potential difference of one volt.

When a nucleus is in an excited state it may emit one or more photons as a result of de-excitation of the nucleus. The emission of these photons is known as gamma radiation. Due to the uncharged, massless nature of gamma rays, they have very little ionisation power. As such, travelling at the speed of light, they can penetrate deeply into a material before their energy is imparted. The three key interactions of gamma rays are photoelectric absorption, pair production and Compton scattering.

Photoelectric absorption is the process of a photon interacting with an absorber atom leading to the disappearance of this photon. A photoelectron is ejected from the atom in place of the photon.

Pair production occurs when the energy of the gamma ray is greater than the rest-mass energy of an electron (1.02 MeV). However, the most likely occurrence of this is at energies greater than 5 MeV. The process that occurs is the conversion of the gamma ray to a positron-electron pair.

Compton scattering is the interaction of a gamma ray photon with a stationary electron. Momentum is conserved and a portion of the energy of the incoming gamma ray photon is imparted to the electron. This is shown in Figure 2.1 and described by Equation 2.4.

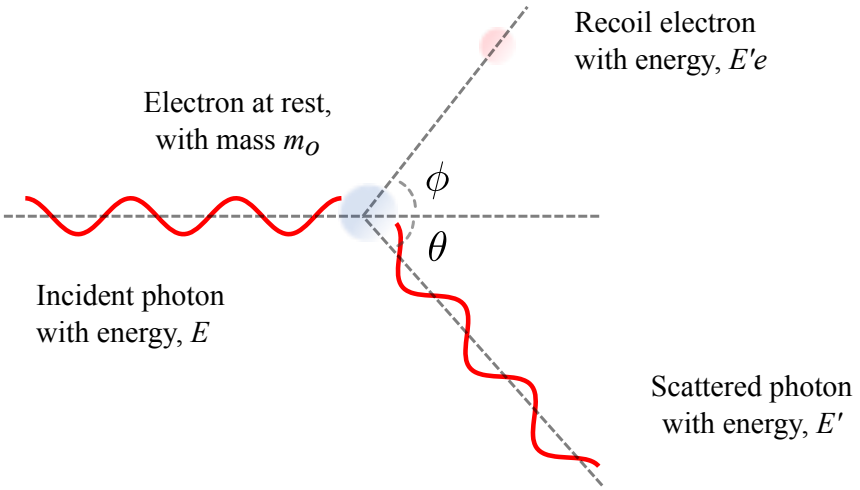


Figure 2.1: Schematic showing an incident photon interacting with a resting electron, and the resulting scattered photon and recoil electron.

$$E' = \frac{E}{1 + (\frac{E}{m_o c^2})(1 - cos\theta)} \tag{2.4}$$

where $E'$ is the energy of the scattered photon, $E$ is the energy of the incoming gamma ray photon, $c$ is the speed of light, $m_o c^2$ is the rest-mass energy of the electron (0.511 MeV), $\theta$ is the scatter angle (as shown in Figure 2.1).

In an organic substance, the low Z of the materials is such that pair production is not likely to occur [24]. This means that the maximal energy imparted is usually at the Compton scatter angle of $\pi$ radians. Substituting this angle into Equation 2.4, results in Equation 2.5, known as the Compton edge formula.

$$E' = \frac{E}{1 + 2(\frac{E}{m_o c^2})} \tag{2.5}$$

A summary of the most likely gamma interactions in a material at a given energy is shown in Figure 2.2.

Figure has been removed due to
Copyright restrictions

Figure 2.2: Relative importance of gamma interactions as a function of incident photon energy [25].

## 2.2 Neutron interactions

A neutron has a mass of 1.674927x10$^{-27}$ kg and it carries no charge. Depending on the energy of a neutron, the dominant interaction in matter will change. A number of classifications are given for neutrons depending on the neutron energy. These classifications are summarised in Table 2.1.

Table 2.1: Neutron classification based upon its energy [26]. Note, this definition of a thermal neutron assumes that at 0.025 eV the neutron is 'roughly in thermal equilibrium with its surrounding medium' [27].

| Neutron classification | Energy range |
|---|---|
| Fast | 1-20 MeV |
| Intermediate | 300 eV - 1 MeV |
| Resonance | 10 - 300 eV |
| Slow | 1 - 10 eV |
| Epicadmium | 0.6 - 1.0 eV |
| Cadmium | 0.4 - 0.6 eV |
| Epithermal | 0.025 - 0.4 eV |
| Thermal | 0.025 eV |
| Cold | 0.0 - 0.025 eV |

The dominant interaction of a neutron not only depends on the energy of the neutron, but also the atom with which it is interacting. The probability of a certain energy of neutron undergoing a certain interaction with a given target nucleus is described by its cross-section. Neutron cross-sections are given in the unit of barns, where one barn is equal to 10$^{-24}$ cm$^2$. A fast neutron interacting with a light nucleus, such as $^1$H, is most likely to undergo elastic scatter. Whereas, a thermal neutron interacting with $^{10}$B has a reasonable probability of being captured by the $^{10}$B nucleus. An example of the change in neutron elastic scatter cross-section with energy for a number of target atoms is shown in Figure 2.3. The most likely interaction for a given neutron energy interacting with a target nucleus will now be discussed.

### 2.2.1 Fast neutrons

When a neutron interacts with a nucleus and the target nucleus remains in its ground state, whilst the neutron remains with a reduced kinetic energy, it is said to

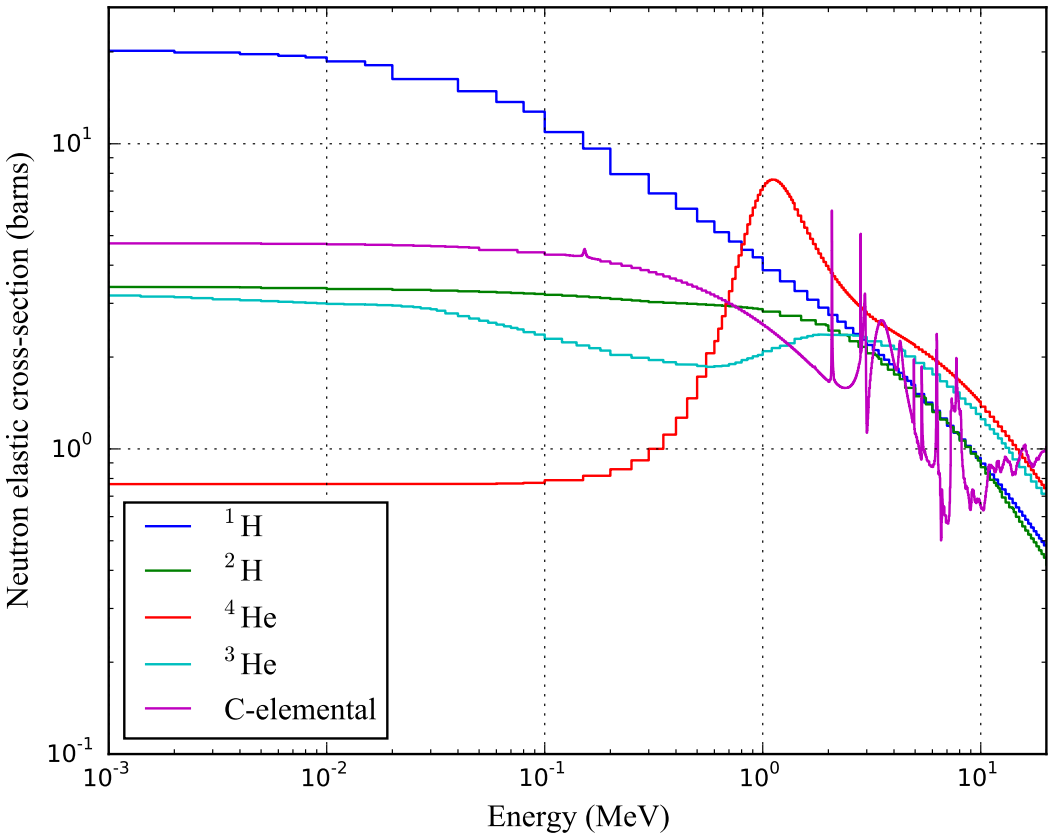


Figure 2.3: Elastic neutron cross-section for a selection of isotopes using data from ENDF/B-VII.r1.

have undergone elastic scattering. The resulting interaction with the target nucleus results in recoil nuclei. During this process, momentum is conserved (when considering neutrons in the energy range of thermal to fast). By assuming the nucleus with which the neutron interacts is at rest, the energy of the recoiled nucleus is described by Equation 2.6, and is shown in Figure 2.4.

$$E_r = \frac{4A}{(1+A)^2} cos^2\theta E_n \tag{2.6}$$

where $E_r$ is the energy of the recoil nucleus, $E_n$ is the energy of the incident neutron, $A$ is the atomic mass number of the target nucleus, $\theta$ is the scatter angle (as shown

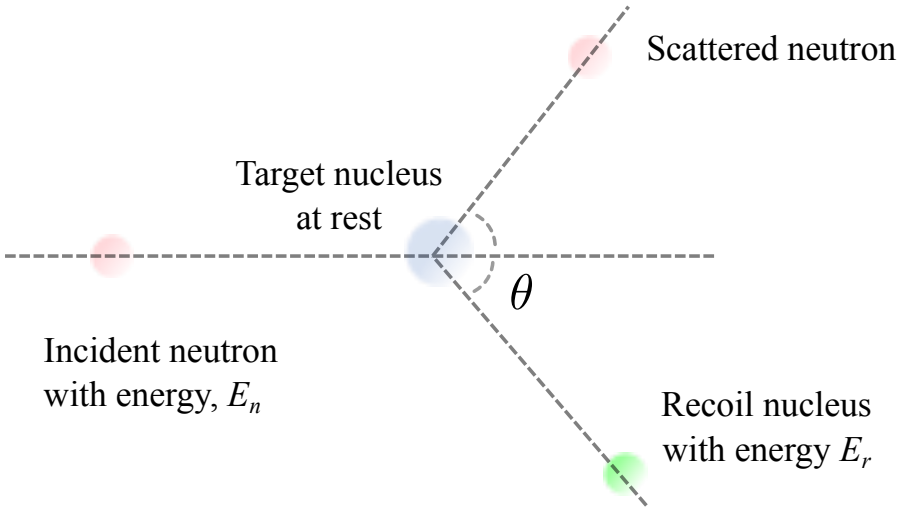


Figure 2.4: Schematic showing an incident neutron interacting with a target nucleus, and the resulting scattered neutron and recoil nucleus.

Table 2.2: Maximal possible energy loss for incident neutron interacting with different target nuclei.

| Target Nucleus | Atomic mass number | Maximal energy loss in a single interaction (%) |
|---|---|---|
| $^{1}$H | 1 | 100 |
| $^{2}$H | 2 | 89 |
| $^{3}$He | 3 | 75 |
| $^{4}$He | 4 | 64 |
| $^{12}$C | 12 | 28 |

in Figure 2.4).

A neutron is said to be moderated as a result of the fractional energy loss from elastic interactions. With a low atomic mass, hydrogen is a very efficient neutron moderator. A neutron can lose up to nearly all of its energy interacting with a hydrogen proton, depending upon the trajectories of the neutron and proton after collision. Neutron elastic scattering is abbreviated with the symbol (n,n). Using Equation 2.4 maximal energy losses for isotopes beyond hydrogen are calculated in Table 2.2.

However, when the energy of a neutron is sufficiently high enough, as a result of an interaction described above, the target nucleus may be left in an excited

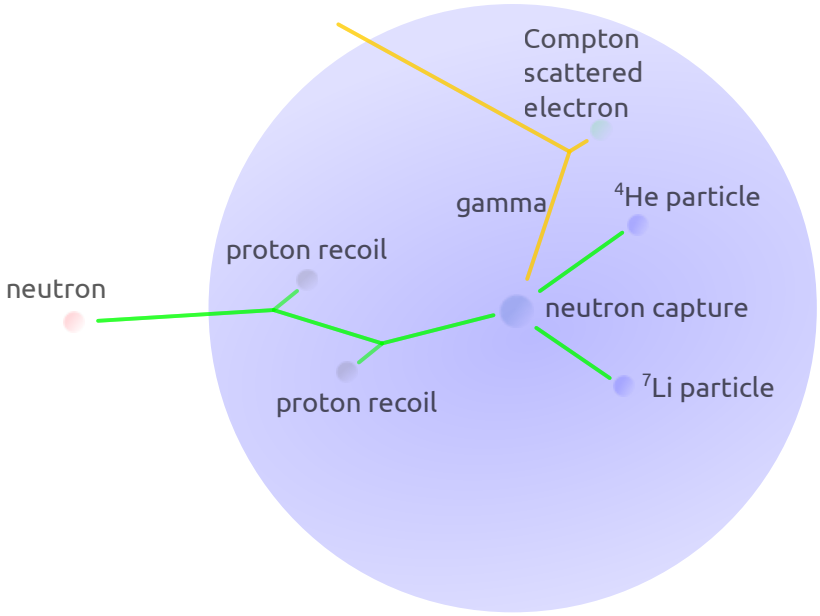


Figure 2.5: A simplified schematic of neutron capture within a $^{10}$B-loaded organic liquid.

state. The nucleus decays from its excited state by the emission of gamma rays. The energy loss of the neutron is greater than that compared to elastic scattering. Inelastic scattering is abbreviated with the symbol (n,n')

### 2.2.2 Thermal neutrons

With low energy neutrons, very little energy is transferred to a recoil nucleus as a result of neutron elastic scattering. This is due to the low kinetic energy of the neutron. When a neutron has been moderated or slowed to 0.025 eV, it is said to be thermal. Thermal neutrons can gain energy when interacting with a target nucleus in a thermal state. That is, the neutron gains a small amount of energy due to conservation of momentum from this elastic collision. This is known as upscattering.

However, when the neutron interacts with certain target nuclei, the most probable outcome is neutron capture. Secondary radiations arising from this capture can result in a number of possible secondary particles. An example of neutron capture in a boron loaded organic liquid is shown in Figure 2.5. The neutron interacts with

a number of protons, before losing enough energy to make it probable that the neutron is captured. Charged secondary particles and a gamma are emitted as result of this neutron capture.

## 2.3 Neutron dosimetry

Neutron dosimetry is performed in order to assess and control the biological effects of a human being exposed to a neutron field. These biological effects are investigated by the International Commission on Radiological Protection (ICRP) and as such, publishes recommendations based upon their assessment of these effects. The International Commission on Radiation Units and Measurements (ICRU) provides guidance and regulation of the physical facets of dosimetry. Hence, establishing methods and quantities which sufficiently represent the quantities outlined by the ICRP. Deleterious biological effects resulting from human exposure to ionising radiation which are considered by the ICRP can be described as stochastic effects (cancer and genetic) and deterministic effects (tissue effects). Stochastic effects are those for which there is a probability of a deleterious effect as a result of exposure, as such, for a certain exposure, the effects may or may not occur. Deterministic effects are based upon tissue damage, whereby a threshold exists and below this threshold, no deleterious effect will occur.

### 2.3.1 Absorbed dose

All dose quantities are based on the fundamental definition of absorbed dose. This is the mean energy imparted ($d\bar{\varepsilon}$) to an infinitesimal irradiated volume with mass $dm$, thus the absorbed dose ($D$) is defined in Equation 2.7 as:

$$D = \frac{d\bar{\varepsilon}}{dm} \tag{2.7}$$

The SI unit is Gray (Gy), expressed in joules per kilogram (J/kg) [28].

### 2.3.2 Mean absorbed dose

The absorbed dose $D_T$, averaged over the tissue or organ T, is defined as

$$D_T = \frac{\varepsilon_T}{m_T} \tag{2.8}$$

where $\varepsilon_T$ is the mean total energy imparted in a tissue or organ T and $m_T$ is the mass of that tissue or organ.

The SI unit is Gray (Gy), expressed in joules per kilogram (J/kg).

### 2.3.3 Equivalent dose

The nature of ionising radiation is that it changes the atoms and molecules it interacts with, which may result in cell damage. However, when exposed to radiation, if a number of cells absorb the same energy per unit mass, the biological effect will differ depending on the particle which deposited the energy in the cell. An alpha particle will tend to result in greater biological damage compared to a neutron for the same total energy deposited per unit mass. This difference is known as linear energy transfer (LET), with an alpha particle having a high LET.

ICRP103 describes equivalent dose ($H_T$) (in a human tissue or organ) as the absorbed dose ($D_T$) in the volume of a specified organ or tissue T due to radiation of type R, multiplied by the radiation weighting factor (due radiation of type R) $w_R$ [18]. This is shown in Equation 2.9.

$$H_T = \sum_R w_R D_{T,R} \tag{2.9}$$

The SI unit of measure for equivalent dose is the sievert (Sv). The radiation weighting factor accounts for the LET of a given type of particle and particle energy. For neutrons, this is a continuous function which is shown in Figure 2.6.

### 2.3.4 Effective dose

Effective dose, E, is the sum of the organ and tissue equivalent doses, $H_T$, each weighted by a specific tissue weighting factor, $w_T$ [28]. This is shown below in Equation 2.10.

$$E = \sum_T w_T H_T \tag{2.10}$$

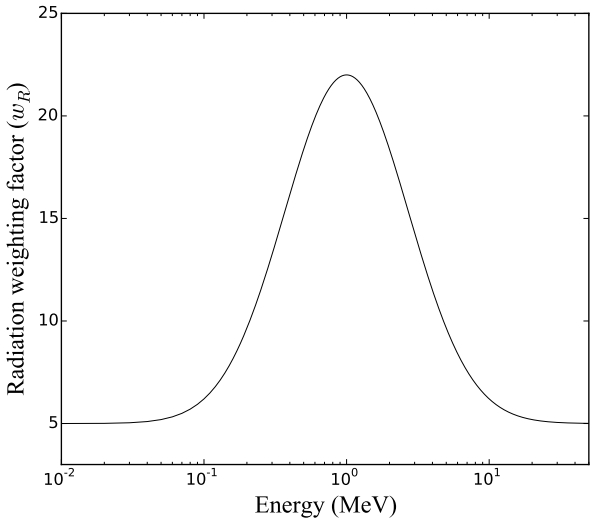


Figure 2.6: Radiation weighting factor, $w_R$, as a function of neutron energy according to ICRP103 [18].

A sample of tissue weighting factors from ICRP60 is shown in Table 2.3 [29]. Effective dose is derived from a number of averaged parameters (sex, body shapes, age etc.) The ICRP guidelines describe it as something that cannot be measured, and as such, one can only estimate effective dose. It cannot be considered as specific for any individual.

Table 2.3: Table denoting the weighting factors ($w_T$) for a selection of tissues from ICRP60 [29].

| Organ/Tissue | $w_T$ |
|---|---|
| Gonad | 0.20 |
| Colon, Bone Marrow (red), Lung, Stomach | 0.12 |
| Bladder | 0.05 |

Considering a 1 MeV neutron entering left-lateral (LLAT) or right-lateral (RLAT), the neutron will likely be moderated by the arms, before reaching an organ such as the lungs. However the same neutron entering the body from the front, experiences less moderation before reaching the same organ. Thus, for the same energy of neutron, it can be seen the angle of incidence of the neutron field is of importance to estimate the effective dose. A summary of the angles of incidence described in this

research is shown in Figure 2.7.

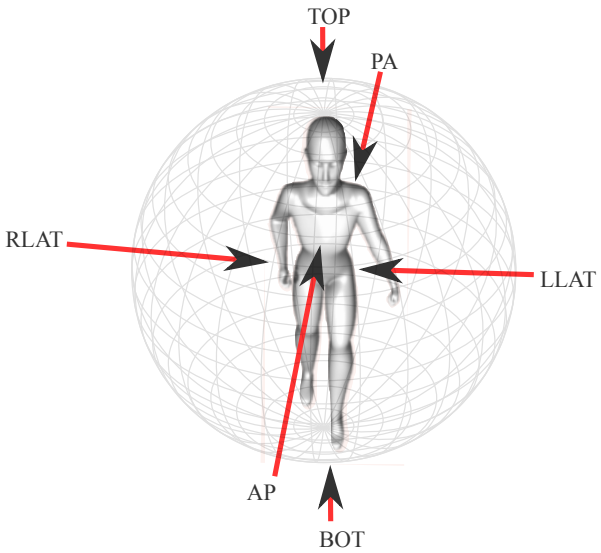


Figure 2.7: Diagram showing the abbreviations of angles of incidence used in this work.

For estimating the effective dose of a neutron workplace field conversion coefficients can be used. A neutron fluence can be transformed into an effective dose for a given incidence of the neutron field, by applying fluence to effective dose conversion coefficients that change with energy and angle [30]. Figure 2.8 shows how the effective dose coefficients change for antero-posterior (AP), postero-anterior (PA), left-lateral (LLAT) and right-lateral (RLAT) incident radiation. It can be seen that the greatest health risk is experienced with the AP direction of incidence, while the lowest risk is with RLAT incidence.

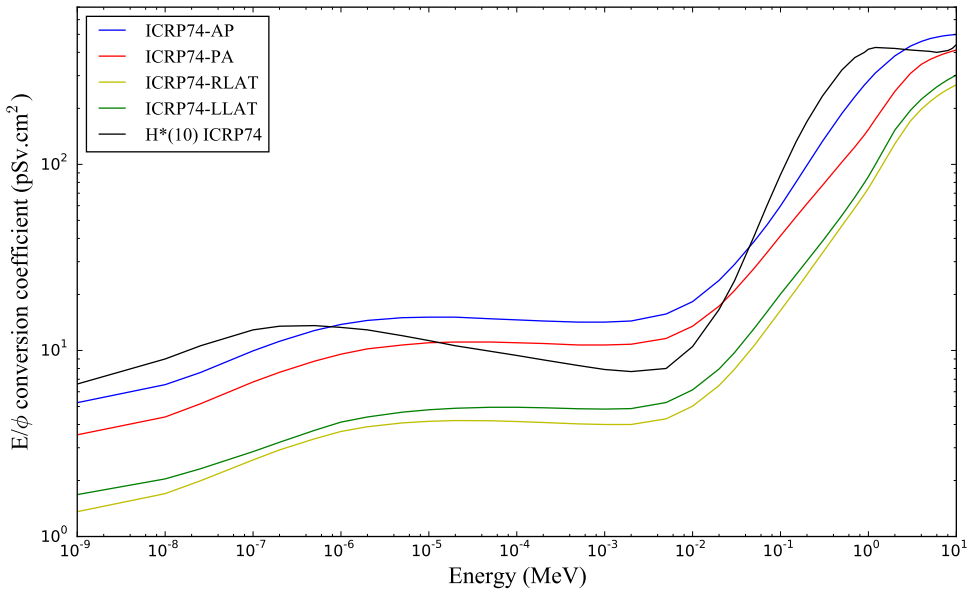


Figure 2.8: Effective dose coefficients for AP, PA, RLAT, LLAT are shown for ICRP74 [30]. In some energy regions, ambient dose equivalent (*H*(10)*) does not always provide a conservative estimate of the neutron dose.

### 2.3.5 Ambient dose equivalent

For operational neutron dosimetry, *ambient dose equivalent* (*H*(10)*) is used to perform area surveys. This quantity is based upon the dose at 10 mm depth in a 30 cm diameter ICRU sphere in an expanded and aligned field [28]. This quantity is isotropic and is supposed to be a conservative measure of the risk, carrying a higher conversion coefficient than the AP fluence to effective dose conversion coefficient. However, it can be seen in Figure 2.8 this is not the case for the values currently used in UK industry of ICRP74 [30]. ICRP116 provides an updated set of coefficients to improve upon this conservatism. However, it still falls short in some areas of the spectrum [19, 31]. In this research, the data from ICRP74 have been used as UK legislation is currently based upon this. Furthermore, it is the standard by which existing neutron area survey meters are calibrated [8].

## 2.4 Neutron detection methods applicable to neutron dosimetry

### 2.4.1 Gas detectors

Most gas based neutron detectors work by detecting secondary particles arising from thermal capture or recoil reactions within the gas. These secondary reaction products undergo gas multiplication and the amplified charge is detected. A common gas used in neutron detectors is $^{3}$He which has a very high thermal neutron capture cross-section of 5330 barns. This capture reaction is shown in Equation 2.11

$$^{1}n +^{3} He \rightarrow ^{3}H\ (0.191\ MeV) +^{1} p\ (0.573\ MeV), \tag{2.11}$$

However, it is well-documented that $^{3}$He is a high cost, limited supply solution [17]. An alternative is the boron-containing gas, $BF_3$. These gases will usually contain a high enrichment of the high neutron capture cross-section isotope, $^{10}$B. The $^{10}$B capture reaction for 6% branching ratio and 94% branching ratio are shown in Equation 2.12 and Equation 2.13 respectively.

$$^{1}n +\ ^{10}B \rightarrow ^{7}Li +^{4} He\ (Q - value = 2.79MeV) \tag{2.12}$$

$$^{1}n +\ ^{10}B \rightarrow ^{7}Li +^{4} He + \gamma\ (0.477\ MeV)(Q - value = 2.31MeV) \tag{2.13}$$

If the reaction takes place close to the walls of the detector, the $^{7}$Li or $^{4}$He will interact with the detector walls. This results in a non-constant energy deposit in the detector. This is known as the wall effect. Other such drawbacks include; sensitivity to mechanical vibrations, operating temperature constraints and degradation over the lifetime of the detector [32].

Instead of using a gas with a high neutron capture cross-section, a coating can be put on the inside of the gas chamber (for example, boron-lined proportional counters). A gas with fewer of the problems (such as high temperature operation) associated with $BF_3$ can be used. However, the efficiency of these detectors is 7

times lower than that of a $^{3}$He detector of the same size [17].

A limitation of gas based detectors which rely on neutron capture is the capture reaction provides no information with regard to the energy of the neutron before it was captured.

### 2.4.2 Thermoluminescent dosimeters

Thermoluminescent dosimeters (TLD) are a passive neutron detector which are commonly used in personal dosimetry applications. When a thermoluminescent material is exposed to ionising radiation, free electrons move to other areas within the material, where they become trapped. This leads to electron-hole pairs being created. When the thermoluminescent material is heated, these trapped electrons are freed and the electron returns to ground state. This release of energy results in an emission of light, where the intensity of the light is proportional to the radiation exposure. For neutron detection, $^{6}$LiF is used for an efficient thermal neutron detector. The resulting lithium capture reaction products deposit their energies on the thermoluminescent material. However, the primary limitation of TLDs for dosimetry applications is that they are a non real-time device. A fatal dose would only be realised after the TLD has been processed. For this reason, other passive detection methods such as gold foils are also not considered in this thesis.

### 2.4.3 Coated semiconductors

By reverse biasing a PN junction Si diode, charged particles can be detected by the charge arising from electron-hole pair collection in the semiconductor media. Using a neutron conversion layer coating on the body of the diode, neutron detection can be achieved, even in mixed radiation fields [33]. High thermal neutron capture cross-sections for $^{10}$B and $^{6}$LiF make them a very suitable coating for diode based detectors [34, 35, 36, 37, 38]. For detection of neutrons at higher energies, a thin polyethylene layer can employed, to allow for detection of charged particles produced by proton recoil events [13]. Coated semiconductor detectors are discussed further in chapter 2.

### 2.4.4 Bonner sphere spectrometers

In order to perform neutron dosimetry, an instrument with a response that varies with neutron energy must be used. One of the most widely used instruments for performing accurate neutron spectrometry is the Bonner sphere spectrometer [39, 40, 9]. Using a thermal neutron detector at the centre of a spherical moderator, typically polyethylene, a thermal neutron response is obtained for that sphere size. By changing the size of sphere, different thermal neutron responses are observed, Figure 2.9 shows a number of these spheres with the thermal detectors.


Figure 2.9: A range of Bonner sphere spectrometers for use with thermal neutron detectors [41].

An example of these responses for different sizes spheres can be seen in Figure 2.10. Typically, the sphere size is changed in 2.54 cm increments. The thermal neutron response for each of these different sizes is then processed using a mathematical technique known as unfolding [43, 9]. A general review of neutron spectrum unfolding techniques is given by by Matzke [43]. Unfolding codes such as GRAVEL, MIEKE and FRUIT require *a priori* information of the field to achieve accurate results [44, 45, 46]. Although recent developments in unfolding codes shows potential for unfolding without *a priori* information of the field [47, 48]. The time consuming nature and complexity of Bonner sphere spectrometers does not make

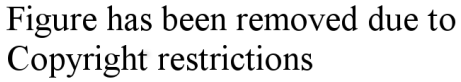


Figure 2.10: Response of Bonner spheres of various sizes to monoenergetic neutrons [42].

them attractive for neutron area survey purposes.

### 2.4.5 Scintillator

Scintillation based detectors are one of the most established neutron detection techniques. A typical organic scintillator consists of a hydrogen-carbon based solution, which detects light arising from proton recoil from the elastic scattering of a neutron with a hydrogen nucleus. The proton excites the $\pi$-electrons in the scintillator. The de-excitation of these $\pi$-electrons results in a pulse of visible light. Depending on the chemistry of the scintillator, this can result in a detected fast pulse of around 30 to 40 ns in length. A scintillator is also sensitive to electrons, arising from gamma interactions. However, the ionising densities of the electron and proton are different, resulting in different pulse shapes. By detecting the pulse of light with a light detector such as a photomultiplier tube, an electrical signal can be observed which is proportional to the magnitude and temporal properties of the scintillation event. Using pulse shape discrimination techniques, it is possible to determine the type of interacting particle. This is further described in chapter 5.

## 2.5 Neutron detection electronics

Scintillation based neutron detectors are discussed extensively in this thesis. Experimental work utilising these devices is described in chapters 6,7 and 8. A short discussion of some of the associated electronics required for these detectors now follows.

### 2.5.1 Photomultiplier tubes

The conversion of the weak light from a scintillation event to an electrical signal is most commonly performed by a device known as a photomultiplier tube (PMT). A schematic drawing of a PMT is shown in Figure 2.11.

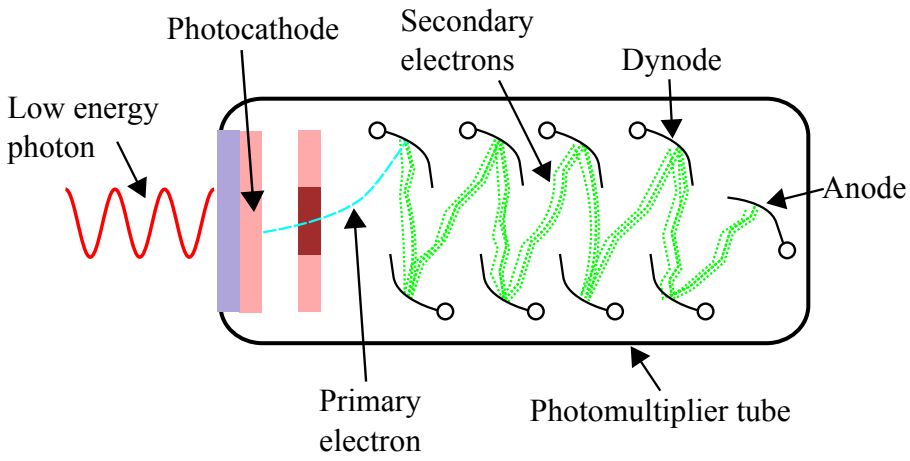


Figure 2.11: A schematic overview of the operation of a photomultiplier tube (PMT).

When an incident photon hits the photocathode, it is converted to a electron by the photoelectric effect. Electrons accelerate from the photocathode towards the first dynode, directed by focussing electrodes. This acceleration is because of the electric field caused by the large potential difference (typically 1-2 kV) between the cathode and anode in the PMT. As each electron hits the metal plate, more than one secondary electron is emitted. With sufficient dynode stages, a current gain occurs by the time the electron beam reaches the anode in the PMT. This gain is typically in the order $10^7$ to $10^8$.

The efficiency of a photocathode stage is typically around 20-30%. This efficiency is also a function of the wavelength of the incident photon. As a result, a PMT must

be matched to a given scintillator. This is to ensure a good matching of wavelength of light as a result of scintillation to the PMT wavelength sensitivity.

### 2.5.2 Digitising electronics

With the advances in semiconductor technology in the last decade, there has been an increased focus towards digital approaches to neutron detection [49, 50, 51, 52]. This approach is particularly of benefit to portable real-time applications such as the one considered in this research. Prior to FPGA based systems, the traditional approach relied on large rack-mounted arrays of equipment. An example of such equipment installed at the National Physical Laboratory, Teddington can be seen in Figure 2.12.

In order to transform a pulse from an analogue signal to a discrete digitised signal an analogue-to-digital converter (ADC) is used. The incoming waveform is sampled at a certain frequency with a set resolution.

The Nyquist Sampling Theorem explains that a waveform should be sampled at a rate of at least twice its frequency. However, the nature of typical pulses of interest in radiation detection is that they are transient-like. Therefore, aliasing becomes less of a problem, and, to find an optimal ADC specification for a system, experimental work is usually required [53].

As well as considering the sample rate, ADC bandwidth should also be considered. ADC bandwidth is defined as the upper frequency at which a sinusoidal signal at the input is attenuated by 3 dB at the output of the ADC.

ADC resolution can play an important role in the performance of a nuclear instrumentation system. Considering the potentially large span of energy ranges of interest in radiation detection systems, the energy resolution of a system will be impacted by the ADC resolution. For nuclear instrumentation (although this depends upon the type of neutron detector), a typical ADC will be sampling at a rate, in the order of, 100 to 1000 Mega-samples-per-second (MS/s). ADC resolutions for nuclear instrumentation are typically between 8 and 14 bits [54].

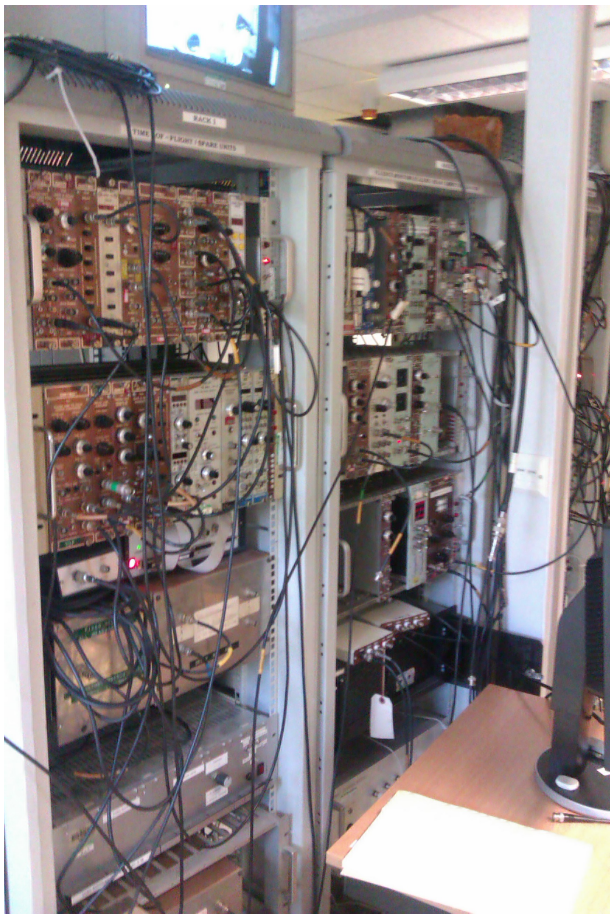

Figure 2.12: Analogue radiation measurement electronic hardware at National Physical Laboratory, Teddington.

### 2.5.3 Field Programmable Gate Arrays

A digitised signal from an ADC is typically fed to processing logic. A Field Programmable Gate Array (FPGA) allows custom logic blocks to be created within an integrated circuit. These logic circuits can operate at very high speeds. When compared to a microprocessor system, the true advantage of FPGAs can be seen when considering the parallel processing capabilities. A microprocessor executes single machine instructions sequentially. An FPGA can perform potentially thousands of operations in parallel logic blocks. As a result of this, fast, real-time digital signal processing can be performed [55]. Indeed, the use of FPGAs in nuclear instrumentation systems is widely reported [56, 57, 58, 59, 60, 61, 62]. After performing the

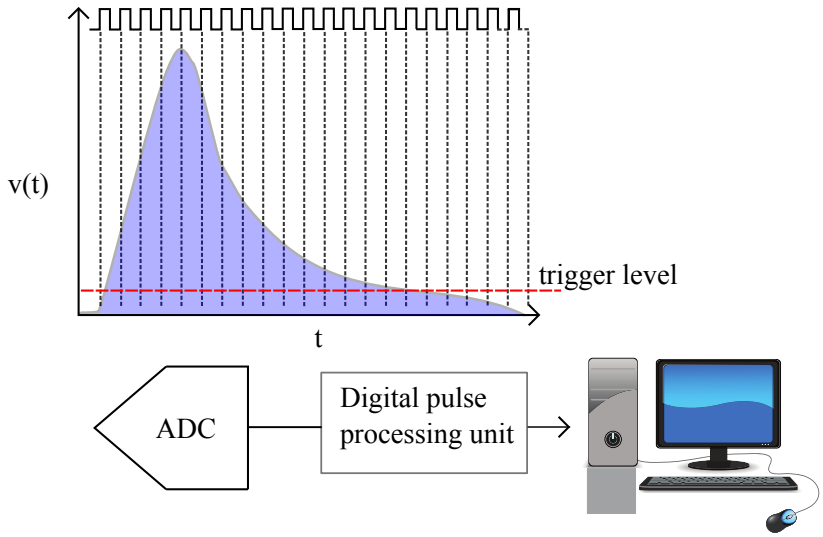


Figure 2.13: A typical pulse processing system based upon an ADC and FPGA configuration.

timing critical pulse processing in custom written logic blocks, the processed pulses can be then passed to a microprocessor at lower data rates than the ADC sample rate. Licensed central processing unit (CPU) architectures (such as an ARM 32 bit processor) can be used in the FPGA to allow a complete pulse processing system, with a CPU running an embedded operating system. This allows whole solutions to be housed within a single chip package to allow for compact, portable, pulse processing systems.

The operation of such a pulse processing system typically relies on an incoming signal having a greater amplitude than a given trigger threshold, as shown in Figure 2.13. Once the signal does become greater than the trigger, the pulse is then sampled. However, it is usually beneficial to record a number of samples before the trigger time. As such, a small buffer is usually used to hold the current and a number of previous samples at any given sample time. The pulse is then usually sampled for a fixed number of samples. The whole pulse can then be sent to a further processing system, in this example, a PC.

A bespoke FPGA based pulse processing system using a 14 bit 150 Ms/s ADC has been developed during this research and is described in chapter 7. Further supporting information is also provided in Appendix B.

## 2.6 Data processing techniques

### 2.6.1 Artificial neural networks

Traditionally, to perform neutron spectroscopy a characteristic set of responses are unfolded with a measured neutron spectrum. This technique has already been discussed with its use with Bonner sphere spectrometers in section 2.4.5. The essence of this problem is one of pattern recognition. Artificial neural networks (ANN) are well proven in their pattern recognition abilities [63]. ANNs have been implemented to learn the response of neutron instrumentation and estimate the resulting neutron spectrum [64, 65, 66, 67, 48, 68].

The first stage of usage of an ANN is to convert the problem into a format which can be understood by the ANN. An example of such a problem is shown in Figure 2.14. In this example, the ANN is trained to learn a set of handwritten numbers, in a 28x28 pixel image. A simplified example of data manipulation which could be used will now be described. Within this pixel grid, each pixel could be sampled; if a pixel was blue, that grid value is 1, if it was white, the grid value is 0. In this case, 784 input neurons can be used to correspond to each of the pixels. Next, the output value for each of these images should be decided. In this example, the output numbers are normalised to 10, such that a handwritten "1" has an output of 0.1. Therefore, the ANN now consists of 784 inputs and a single output. However, the optimisation of the number of hidden neurons in the network does not have an exact prescription. With too many neurons, there is potential for the network to be poor at generalising unknown problems. As such, a common methodology is to start with a low number of hidden neurons and increase the number until a desired error is observed.

Typically, the patterns recognised by ANNs are non-linear and cannot be solved using linear mathematical equations. An example of an ANN architecture suited to such problems is the backpropagation learning algorithm, which learns a desired output from a given input value [69]. The use of a known set of input training data means that backpropagation networks are usually considered a supervised learning method.

In the example considered above, using a backpropagation algorithm for training,

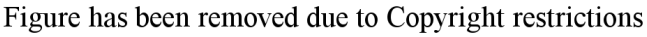


Figure 2.14: An example of a pattern recognition problem where an ANN can be used [63].

random weights are assigned (at the start of training) at each neuron in the ANN and the training data are fed forward through the network, through the activation function. Based upon the error between the output value and the desired value, adjustments are made to the weights. An iterative procedure is usually used to modify the weights based upon an error function. Gradient descent is an example of an iterative error minimisation technique. The change in error (E) for a weight update is calculated using the partial derivative shown in Equation 2.14.

$$\frac{\delta E}{\delta w_{ij}} = \left(\frac{\delta E}{\delta s_i}\right)\left(\frac{\delta s_i}{\delta net_i}\right)\left(\frac{\delta net_i}{\delta w_{ij}}\right) \tag{2.14}$$

where $w_{ij}$ is the weight from neuron $j$ to neuron $i$, $s_i$ is the output, and $net_i$ is the weighted sum of the inputs of neuron $i$.

After the partial derivative of the error with respect to the neuron weight is known, gradient descent is used to update the weights. The gradient based descent function shown in Equation 2.15 is used to find the new weight at time *t+1*. The update of these weights is controlled by the learning rate, $\epsilon$.

$$w_{ij}(t+1) = w_{ij}(t) - \epsilon\frac{\delta}{\delta w_{ij}}E(t) \tag{2.15}$$

The training pattern is fed through the network again and this weight update process is continued until the network training is stopped. This is either based upon a maximum number of epochs or a resulting mean squared error at the output of the network for a given set of input data.

### 2.6.2 Electrical noise

Random unwanted fluctuations of an electrical signal, known as noise, are a characteristic of all electronic circuits. In radiation instrumentation, the desired signal is typically transient-like and of small magnitude, such that an understanding of noise plays an important role in successful radiation measurements [70].

At temperatures other than absolute zero, thermal noise is unavoidable. This noise arises from the random thermal vibration of charge carriers within an electrical conductor. Thermal noise is noise that is of equal amplitude at all frequencies (except very high frequencies). Flicker noise, also known as 1/f noise, is a noise that reduces in amplitude as the frequency increases. It dominates at lower frequencies and flicker noise occurs in almost all circuits carry a direct current. Shot noise is caused by current fluctuations due to the discrete nature of charge carriers. Unlike thermal and flicker noise, it is not frequency dependent.

### 2.6.3 Signal filtering

To reduce the impact of noise in digital radiation detection systems, filtering is used. The purpose of the filter should be to remove unwanted signals from the detected signal whilst, preserving as much of the original information about the detected pulse as possible.

Traditional analogue radiation detection instrumentation system usually relied on some form of resistor-capacitor circuit based integrator within the front end stages of the detector electronics. These circuits can take tens of micro seconds to collect the total charge from a scintillation event. These circuits act as a low pass filter and suppress high frequency noise. In a digital system, typically, the fast digital pulses are preserved and the filtering takes place in software within the FPGA or in post processing on a PC. In a real-time system, with the processing of the signals taking place in the FPGA logic, processing overhead of the filter becomes an important consideration.

In detectors where the signal has proportionality to the energy deposited by a particle, the filter should attempt to retain this sensitivity. In scintillator based detector systems pulse shape discrimination takes place on the falling edge of the pulse. This feature must, in some way, be retained in the output of the filter. It can

be seen that the choice of filter is usually different for each given application.

The moving average filter is one of the simplest forms of signal filtering. As shown in Equation 2.16, at each sample time, the filter averages sample $n$ and following *n+(m-1)* samples.

$$y[n] = \frac{1}{m} \sum_{k=0}^{m-1} x[n+k] \tag{2.16}$$

A finite impulse response (FIR) filter is a more advanced form of feed-forward filter. It is similar to a moving average filter, however, filter coefficients ($h_k$) are applied to the moving average filter. This is shown in Equation 2.17.

$$y[n] = \sum_{k=0}^{n-1} h_k x[n-k] \tag{2.17}$$

For high resolution spectroscopy, trapezoidal and triangular shaped filtering has been shown to have potential advantages [71]. An example of a triangular filter is shown in Equation 2.18.

$$z[n] = z[n-1] + y[n] - 2y[n-k] + y[n-2k], \tag{2.18}$$

where $z$ is the filtered pulse, $y$ is the modified pulse (pulse from peak onwards), $n$ is the current sample bit and $k$ is an integer for the time constant of the filter.

To demonstrate some simple filter responses, two pulse shapes have been modelled. These pulse shapes were derived using the Marronne model for neutron and gamma pulse shapes arising from a liquid scintillator, shown in Equation 2.19 [72].

$$v(t) = A(e^{-(t-t_0)/\theta} - e^{-(t-t_0)/\lambda_s} + Be^{-(t-t_0)/\lambda_l}) \tag{2.19}$$

where t is time, A, B, $\theta$ and $\lambda$ are all parameters to define the pulse characteristics. The two pulse shapes shown in Figure 2.15 used experimental values published by Aspinall et al. for pulse shapes within an organic liquid scintillator [73]. A thorough evaluation of these filtering techniques would demand a full noise analysis in a system to be performed, to find the resulting noise spectrum. However, for the purposes of demonstrating some simple filtering methods, random noise has been propagated onto each time sample. The two pulses with this added noise are shown

in Figure 2.15. The results of filtering these pulses using FIR, moving average and triangular filters are also shown in Figure 2.16.

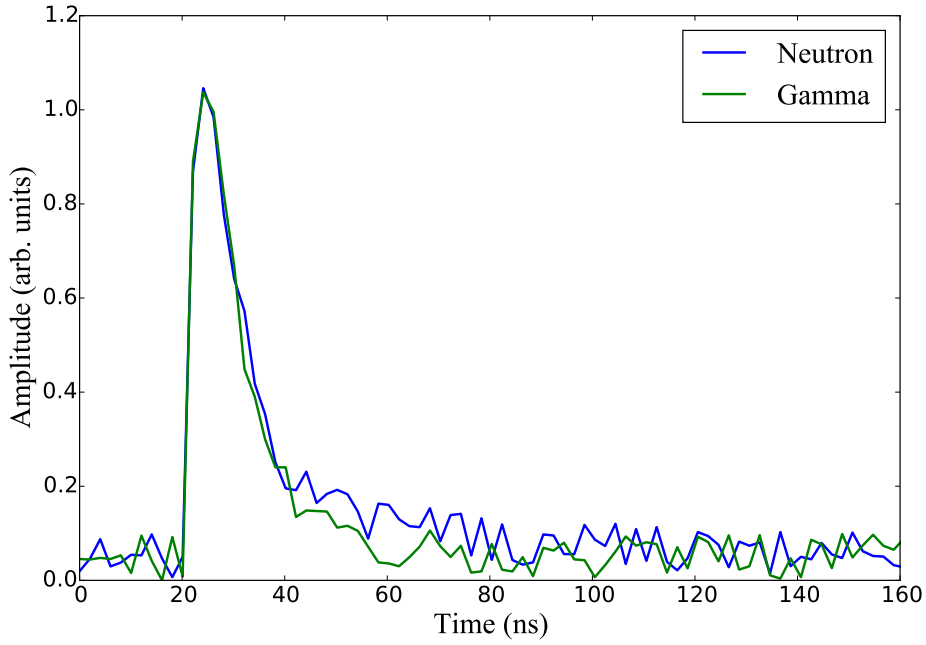


Figure 2.15: Raw pulses synthesised using a Marrone model [73, 72].

It is interesting to note the differences between the filters show in Figure 2.16. The triangular filter changes the original pulse shape the most. The parameter $k$ from Equation 2.18 is varied to be most sensitive to the difference between the neutron and gamma pulse. In the pulses in Figure 2.15 this is around 60 ns. The peak of the output of the triangular filter is used to determine if the signal originates from a gamma or neutron [74]. Although this algorithm does not rely on complex mathematics, it induces a delay on the signal, which may impact some applications.

The FIR filter and moving average filter both perform similarly in terms of their ability to highlight a positive difference between the two signals. Further analysis of these and other filtering methods can be found in the research published by Kamleitner et al. [75].

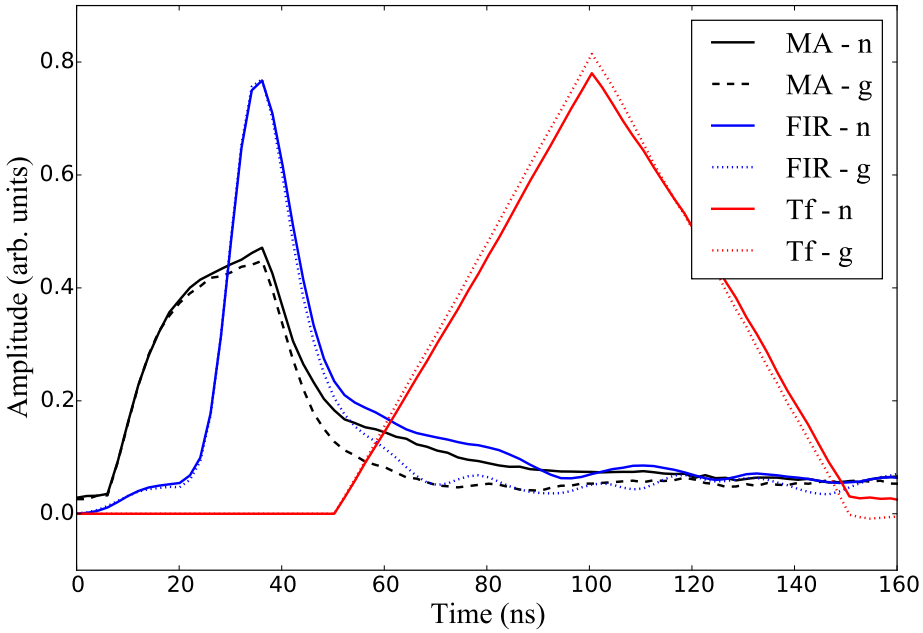


Figure 2.16: Example of signal filtering using a moving average (MA), triangular (Tf) and FIR filter.

### 2.6.4 Summary

This chapter has introduced heavy charged particle, gamma and neutron interactions. An introduction to a number of neutron detection methods has been provided. Some of these methods are discussed further in the next chapter, 2. FPGA based scintillator detector systems have been discussed. The application of these systems in this research is further discussed in chapters 6 and 7. Finally, artificial neural networks have been introduced. The use of neural networks in this research is discussed further in chapters 5 and 8.

# Chapter 3

# Critical review of directional neutron survey meters

*Balmer, M.J.I, Gamage, K.A.A and Taylor, G.C.*

*Reprinted from Nuclear Instruments and Methods in Physics Research Section A Accelerators, Spectrometers, Detectors and Associated Equipment. 735:7-11, January 2014 with permission from Elsevier.*

## 3.1 Abstract

Having been overlooked for many years, research is now starting to take into account the directional distribution of the neutron work place field. The impact of not taking this into account has led to overly conservative estimates of dose in neutron workplace fields. This paper provides a critical review of this existing research into directional survey meters which could improve these estimates of dose. Instruments which could be adapted for use as directional neutron survey meters were also considered within this review. Using Monte Carlo techniques, two of the most promising existing designs are evaluated; a boron-doped liquid scintillator and a multi-detector directional spectrometer. As an outcome of these simulations, possible adaptations to these instruments are suggested with a view to improving the portability of the instrument.

## 3.2 Introduction

When estimating the health risk of exposure to neutron fields, the term *effective dose* can be used [18]. This provides a weighted sum of the absorbed dose across the human body. This non-isotropic quantity is not measurable.

Usually, *ambient dose equivalent H*(10)* is used to provide an operational quantity for area surveys. This considers the risk of a neutron field in an area, in a conservative manner, by being independent of the incident direction of the radiation field and approximating effective dose for the direction of incidence that has the greatest risk, i.e antero-posterior (AP). In order to quantify the risk to a person exposed to the neutron field, *personal dose equivalent* is used. Personal dose meters are typically worn on the front of the torso and effects of shielding by the body can affect the readings. This reading is also considered a conservative estimate of the risk making the dose recorded likely to be under-estimated for predominantly postero-anterior (PA) exposure. In 2002 Barlett et al. highlighted a potential limitation of existing neutron survey techniques, due to the lack of consideration to the direction of the field [76]. In some organisations, neutron survey measurements are used for establishing work practices. Due to the conservative nature of the operational quantities, there is potential to over restrict these work practices. Furthermore, although effective dose is not recommended to be used for epidemiological studies, if such an instrument could estimate the effective dose within an area, such studies could only be improved. Research undertaken to assess the effectiveness of the measurement of these quantities in workplaces identified that both energy and direction of the neutron field should be considered [8]. Furthermore, from these studies it can be seen that ambient dose equivalent is not always a conservative estimate of the effective dose. This highlights the need for an instrument that can accurately measure energy and directional dependence of a neutron field.

## 3.3 Existing Neutron Survey Techniques

The method of detecting thermal neutrons within a range of hydrogenous moderators, known as a Bonner Sphere Spectrometer (BSS) system, is a well-established technique for neutron spectroscopy. As such, the response of this instrument has

been well-characterised [9]. Combining this response with unfolding techniques, reasonably reliable neutron spectroscopy can be achieved. However, the time consuming nature and complexity of taking such field measurements make it counterproductive. This technique also does not permit real-time neutron surveys to be achieved.

Existing neutron survey instruments measuring *H*(10)* which are commonly used, including the Leake Detector, NM2 and Studsvik instrument [8], are typically single detector instruments. Inferring the direction of the field using such instruments would present a tough challenge due to the single detector design of these instruments. However, such instruments have been in operation for many years and can be used as a basis for establishing the requirements of a practical directional neutron survey instrument that is portable. For daily area survey measurements to be taken in a workplace, an instrument needs to be portable and allow real-time data capture to take place. It is anticipated that it would be powered by batteries to allow for maximum portability of such an instrument.

With a portable battery powered directional neutron survey instrument, it is anticipated that accurate data sets for work places could be obtained, and would have potential to improve work practices. This would also improve health studies on the effects of neutron radiation.

A broad range of neutron detection techniques have been employed to develop numerous instruments that could be used for directional neutron spectrometry. These instruments are reviewed and their required additional improvements, for use as a real-time portable directional neutron survey meter, are considered.

Perhaps the most comprehensive work undertaken to date in the field of directional neutron dosimetry is the 'Evaluation of Individual Dosimetry in Mixed Neutron and Photon Radiation Fields' (EVIDOS) project. The EU funded EVIDOS campaign was undertaken to attempt to understand the effectiveness of personal dosimetry instruments in workplace fields, considering both energy and direction dependence of the field. In this project, to enable a number of workplace fields to be characterised in a timely manner, two very different instruments were developed. The first was a telescope design directional neutron spectrometer [12], the second a directional spectrometer which could be likened to a collection of personal dose meters around a phantom [13].

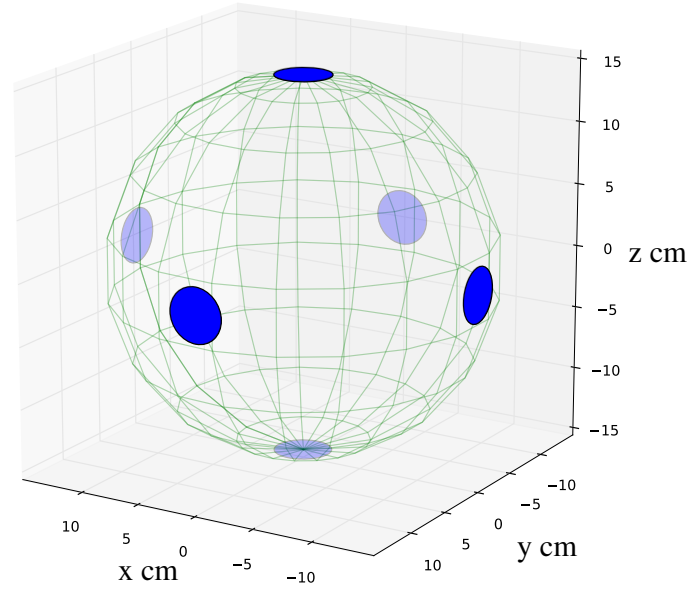


(a)

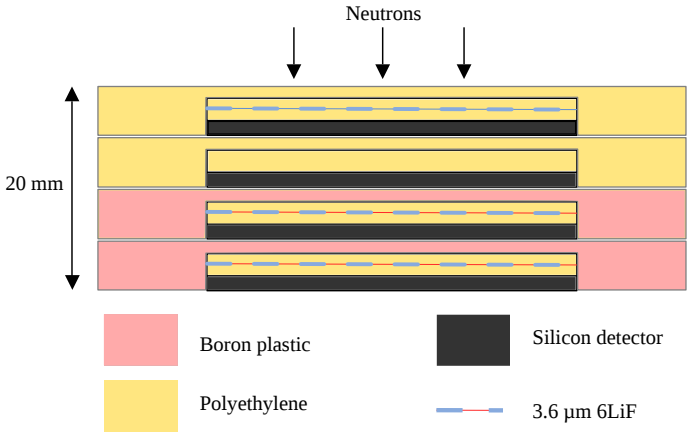


(b)

Figure 3.1: Detector developed by PTB as part of the EVIDOS campaign. (a) The 6 detectors are located around the perimeter of the 30 cm diameter polyethylene sphere. (b) Each detector consists of 4 sandwiched silicon detectors, each optimised for detection at different energy levels. Figure replicated from [13].

### 3.3.1 Multi-Detector Directional Spectrometer

The instrument developed by Physikalisch-Technische Bundesanstalt (PTB), as a part of the EVIDOS project consists of 6 neutron detectors located on the outer circumference of a polyethylene phantom (Figure 3.1). In order to achieve high

sensitivity detection with a flat response across the range of 0-20 MeV poses a challenge in a single diode package. To achieve these goals, multi-element detectors consisting of 4 sandwiched silicon detectors within a single aluminium housing were used in this design. For detection at lower neutron energy levels, boron-doped plastic surrounds the $^{6}$LiF coated silicon diode. For higher energy neutrons, a 30 $\mu$m polyethylene layer is employed to allow for detection of charged particles produced by proton recoil events.

The response for each of the 24 detectors at different energies and directions presents a complex matrix for the response function of the instrument. This matrix was then used for unfolding the neutron spectrum. As a part of the EVIDOS campaign this detector was successfully used to characterise a number of work place fields. This characterisation was verified in conjunction with BSS measurements.

By considering the dose rates experienced by each detector and calibrated data, it could perhaps be worthwhile to investigate if these data could train a neural network to predict the effective dose. Such a technique could be implemented on an FPGA and promote itself well to real-time operation. However, with only 6 detectors it could prove difficult to achieve a good angular resolution with a neural network. A 30 cm polyethylene sphere is used in this design which has a mass of around 13.6 kg. When coupled with digitising electronics this would present a challenge to make this device a portable instrument. For optimal results, prior information on the energy spectrum under investigation was required to aid the unfolding process [11]. This presents challenges when working in an unknown field where an instrument such as a Bonner Sphere Spectrometer system is not available. This restricts the instruments usage as a true real-time neutron dosimetry meter.

### 3.3.2 Superheated Emulsion Detectors

The 'directional telescope' developed for the EVIDOS project [12], presents a novel instrument using a superheated emulsion detector. The instrument consists of a 30 cm moderating sphere with a window subtending from the outer perimeter of the sphere through the detector located at the centre of the detection. When neutrons enter the detector, a superheated emulsion of dichlorotetrafluoroethane (R-114), bubbles form. These bubbles are then detected acoustically using piezo detectors.

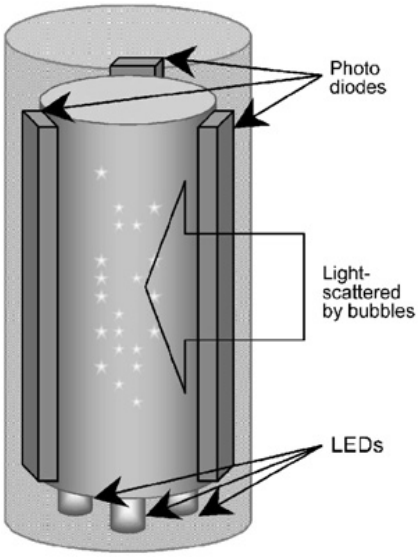


Figure 3.2: An example of a Superheated Emulsion Detector using optical detection of the bubbles [77].

By controlling the temperature of this superheated emulsion, different neutron detection thresholds can be set. The superheated detector is located within the centre of a 30 cm nylon-6 sphere. This neutron moderator means that the only neutrons being detected should be those which have travelled the telescope window to the centre of the sphere. By rotating the sphere and controlling the temperature, energy and direction of the neutron field can be understood using a suitable unfolding technique.

Due to its time consuming data collection process, this instrument was not used for the EVIDOS campaign [11]. As a result of these limitations, the instrument does not have the same proven ability in an experimental capacity in a workplace field as the PTB spectrometer. When considering the practical implication of the design of a neutron survey meter, the portability is a strong influencing factor on the design. Power drain for the complex temperature cycling and detector rotation would restrict this instruments operating time using batteries as well as impacting on the mass of the instrument.

Using optical readout of bubbles instead of acoustic readout presents another interesting option for directional neutron dosimetry [77]. The instrument consists of a beam of light crossing a superheated emulsion (Figure 3.2). As this beam of light

crosses the detector, the bubbles formed due to detection of neutrons cause scattering of light can be detected in real-time, using silicon photodiodes. This information on the bubble distribution could be used to estimate the direction and energy of the neutron field entering the detector. The development of such techniques within a practical detector is still in their early stages and issues such as life span of these detectors are still under investigation [78].

### 3.3.3 Single Bonner Sphere Spectrometers

Several instruments [79, 80] have been developed incorporating multiple detectors within a single moderating sphere, thus eliminating the need for multiple BSS instruments when characterising a neutron field. Such instruments were not specifically designed for the purpose of directional neutron dosimetry, but could be adapted to be used in such an application. However, the design of many of these instruments relies on $^{3}$He, which has gone into short supply in the last 10 years following increased concern over nuclear security, following the events of September 2001 [17]. Work has begun to attempt to develop these designs with alternatives to the hard to source $^{3}$He [81], however many of these methods of detection remain in their early stages of development.

A passive spectrometer for workplace monitoring with a quasi-isotropic response to neutrons, from thermal to fast energies, was designed by Gómes Ros et al. [82]. Earlier developments [83] of this instrument used $^{6}$LiF and $^{7}$LiF thermoluminescent detectors embedded within a single polyethylene sphere. These detectors were replaced by Dysprosium activation foils to improve photon insensitivity. Following experimentation with a 14 MeV neutron beam, the resulting Dy-foils-based Single Sphere Spectrometer (Dy-SSS) showed promising results with an overall uncertainty of the spectrometer response matrix of $\pm 3$ %. The goal of such instruments is to eliminate any directional bias in the instrument, by averaging the response readings along each axis of the instrument. With careful characterisation such an instrument could perhaps be used for directional dosimetry. However, the response matrix such a complex array of instruments would pose a tough challenge to permit real-time unfolding of the neutron spectrum.

### 3.3.4 Boron-Doped Spherical Scintillator Detector

A theoretical design of a directional neutron survey meter was carried out by Taylor in 2010 [84]. This instrument is a boron-doped spherical scintillator of 20.32 cm diameter interrogated by multiple photomultiplier tubes (PMT). The boron-doped scintillator allows for neutron detection from thermal up to energy ranges of the order of tens of MeV (depending on dimensions of the scintillator). When a neutron enters the scintillator, the elastic collisions causing proton recoil events allow high energy neutrons to be detected. This proton recoil event can then be detected through a scintillation event as a result of this elastic collision. The boron loading of the BC-523A scintillator allows for detection of thermal neutrons through the $\alpha$ particle emitted as a result of the neutron capture. The capture distribution of scintillation events within the detector can then be analysed to provide an estimate of effective dose.

Through Monte Carlo modelling, Taylor obtained a series of capture distributions for different energies and locations of monoenergetic neutron sources. An artificial neural network was then trained with these capture distributions to learn the pattern of the distribution for a given energy. With preliminary training of the neural network, promising results were achieved when the model was bench marked with a $^{252}$Cf source. However, in this proof of concept localising the scintillation event within the detector remains unproven.

Localising the scintillation event within the detector will present a challenge. It is thought that using an array of PMTs coupled to a suitable digital signal processing algorithm, the scintillation event in the detector can be localised. Although the 2x2x2 cm$^3$ voxels used for the simulation present what could be considered a practical size of voxel for a modern multi-channel analyser, it is unknown if this resolution of localisation can be achieved.

Training the artificial neural network will present many challenges. Training with only modelled results could lead to possible inaccuracies. However, to best train the network, a large number of energy levels and directions would be needed to be experimentally obtained, doing this through practical experiments could be prohibitively expensive and/or time consuming.

The flash point of the BC-523A scintillator is a potential cause for concern from a

practical perspective of developing such an instrument. A more practical alternative for similar performance is the EJ-309B5 scintillator, which has a much safer flash point above one hundred degrees centigrade [85]. In such boron-loaded scintillators, the $\alpha$ particle emitted during boron capture events, causes a strong quenching of the scintillation event [86]. Within a scintillator of the size proposed, this could perhaps lead to difficulties detecting such low amplitude pulses. Promising recent developments in the field of crystal scintillators makes $Cs_2LiYCl_6$:Ce (CLYC) a scintillator worthy of consideration for use in this instrument [87].

## 3.4 Investigating Possible Improvements To Existing Designs

### 3.4.1 Simulating Different Moderator Sizes

When considering the upper energy detection range of a neutron detector, a trade off has to be considered between neutron moderation and portability. Typically designs utilise a 30 cm polyethylene phantom to moderate the incoming neutrons and such a phantom has a mass of 13.6 kg. By reducing the size of this phantom, the difference in fluence between the detectors at the front and back of the phantom will be lessened. This reduction in fluence differential will impact on the directional resolution of the detector. However, a reduction to a 20 cm sphere equates to a mass of 4 kg, an attractive mass reduction. In order to investigate the relationship between this upper energy limit and sphere mass, a typical detector was modelled using a Monte Carlo radiation transport code package, MCNP v5.0 [88].

A 30 cm polyethylene sphere (density 0.96 g/cm$^3$) was modelled with two discs (2.5 cm diameter, 1 mm thickness) embedded diametrically opposite each other at a depth of 1 cm within the sphere. On the front face of the moderator detector 1 was closest to the neutron source. Within the back of the moderator, furthest from the source, detector 2 was located along the same axis. The detector was irradiated by monoenergetic, mono-directional neutrons. Sphere diameters of 20 cm and 30 cm were modelled, each being sequentially radiated by a 10 MeV and 20 MeV neutron source. The fluence within each detector was recorded in discrete energy bins and

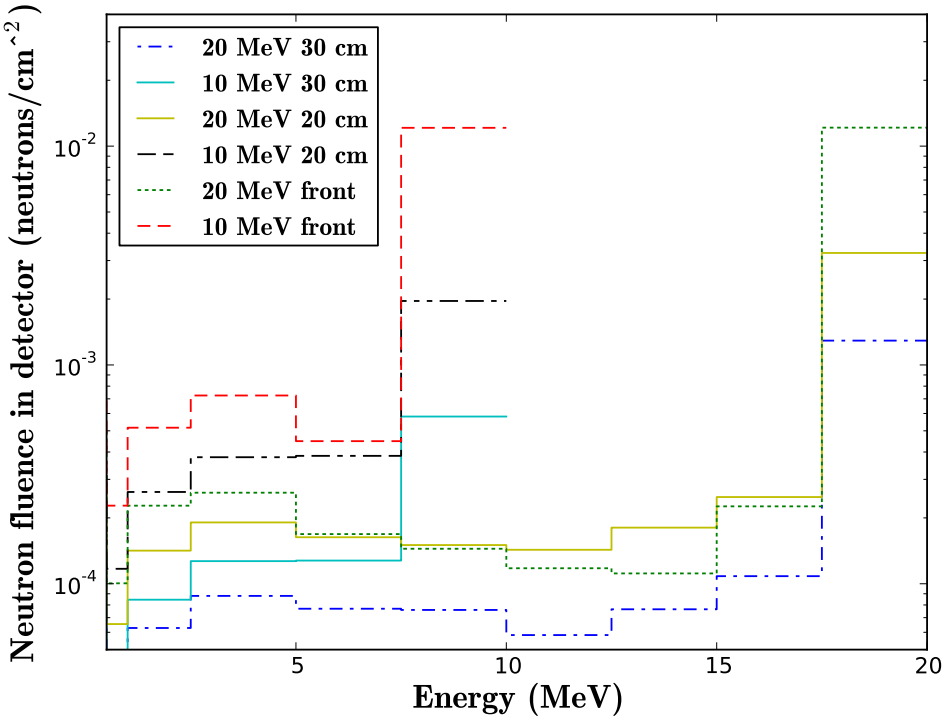


Figure 3.3: Investigating reducing the size of polyethylene moderator shows that by reducing the diameter of the sphere to 20 cm, an upper limit of 10 MeV is set to achieve a similar performance of a 30 cm diameter sphere at 20 MeV.

the fluence between the front and back detector was compared. The results can be seen in Figure 3.3.

By reducing the sphere to 20 cm diameter, an improvement in fluence difference to that at 20 MeV with a 20 cm diameter sphere can be achieved. However, this difference in fluence is still smaller than that of a 30 cm diameter sphere at 20 MeV. This reduction in fluence difference could impact on the performance of the unfolding codes.

### 3.4.2 Neutron Capture Distribution Within A Scintillator

The artificial neural network used by Taylor [84] for the scintillator detector relies on there being directional information within the pattern of the capture distribution.

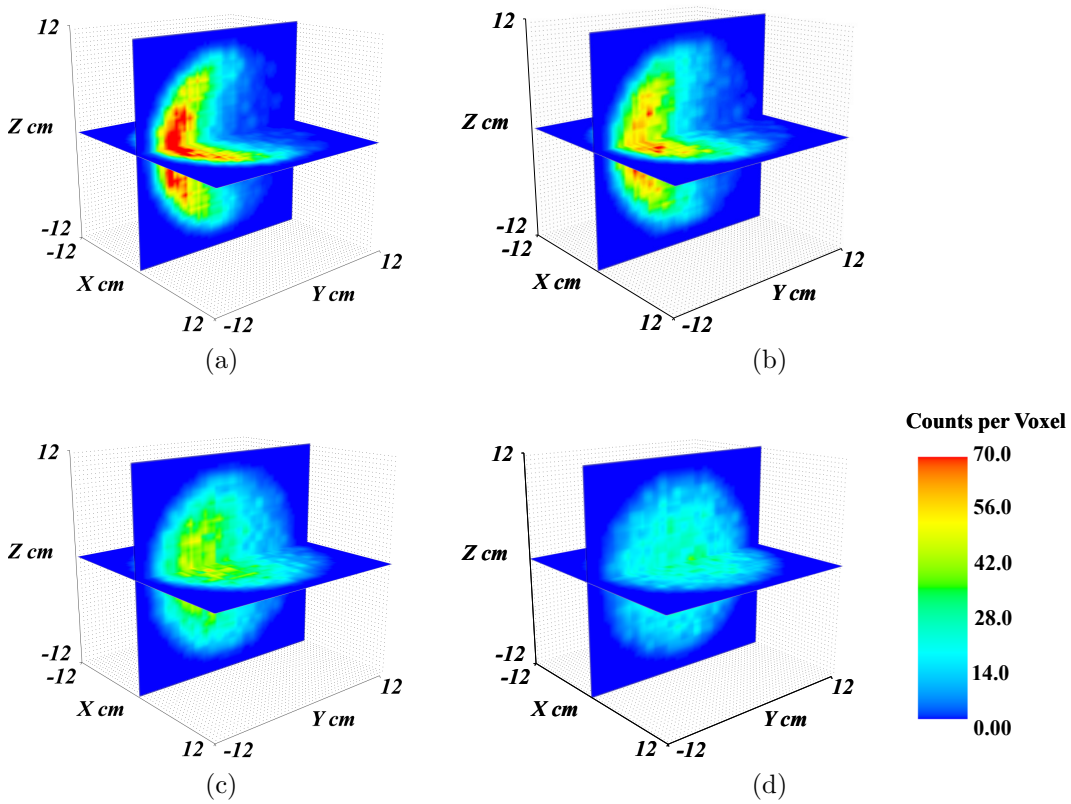


Figure 3.4: Distribution of neutron captures within a 20.32 cm diameter boron loaded BC-523A scintillator exposed to four different monoenergetic neutron energies, (a) 10 keV, (b) 100 keV, (c) 1 MeV and (d) 10 MeV

The detector was modelled in MCNP with a BC-523A scintillator, to investigate these distributions at different energies. The detector was irradiated with AP radiation from a monoenergetic neutron source, for four different energies over the range of 10 keV to 10 MeV. Using the PTRAC output, the coordinates of $10^5$ capture events were binned into 1 $cm^3$ voxels. Using the Mayavi [89] package, the capture distribution of the events within the detector are shown in Figure 3.4.

At 10 keV it can be seen that there is a strong directional indication of direction from the distribution of captures. However, at 1 MeV it can be seen that there is a weaker indication of capture distribution, and as 10 MeV is approached, it is not possible to visually distinguish the direction of the source.

By increasing the size of the scintillator to 30 cm diameter and considering $10^6$

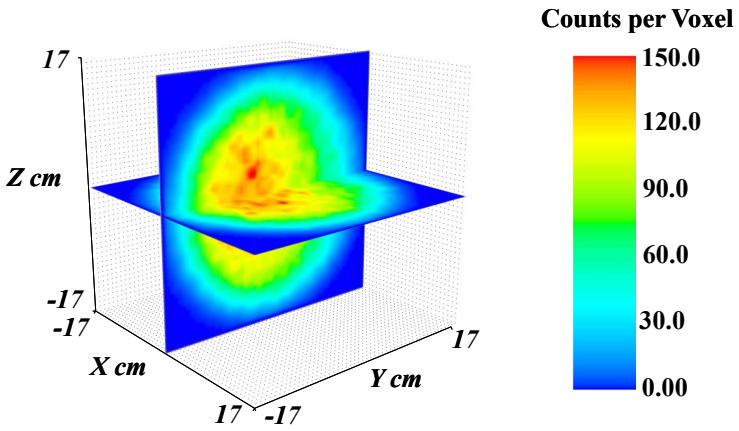


Figure 3.5: Distribution of neutron captures with a 30 cm diameter boron-loaded BC-523A scintillator exposed to a monoenergetic beam of 10 MeV

neutron capture events, the detector was remodelled. By increasing the scintillator to this size it would increase the mass from 4.8 kg to 12.9 kg. It can be seen in Figure 3.5 that the increase in size of the scintillator has not improved the directional information, within the pattern of the capture distribution. For this significant increase in mass of the scintillator, no improvement to the upper energy limit of detection is achieved.

## 3.5 Discussion

Existing neutron dosimetry techniques have been reviewed within this paper and their suitability to application within a portable neutron dose meter has been reviewed. When considering the practical aspects using existing instruments for portable applications, the heavy mass of large moderators restricts their usage. It has been shown that by reducing the upper energy range of the detector, a much lighter mass of moderator can be used with an estimated upper limit of 10 MeV for detection. The detector developed by PTB design could be reduced in size and a much lighter portable instrument could be realised. However, the pre-information required for the unfolding restricts the instruments usage as a true real-time instrument.

Although only theoretical, the design proposed by Taylor presents an attractive option for a portable digitised neutron dosimeter. This instrument holds promise to be a lightweight instruments which could be coupled with a portable digital analyser. Using such digital detection techniques could offer a large degree of versatility through software. With a digital architecture neutron/gamma discrimination techniques could be implemented onto an FPGA multi-channel analyser. Furthermore, with careful selection of scintillator, it could be possible to implement gamma dosimetry within the same hardware. Also as has been highlighted within the paper, the proposed BC-523A scintillator not only limits the upper range of detection, but also outputs a very low amplitude pulse of light as a result of a capture event.

Being able to reliably detect these pulses of light, as a result of the neutron capture, presently remains an unproven concept. The resolution and reliability of this capture localisation will have a big impact on the efficiency and accuracy of the detector.

# Chapter 4

# An investigation into a suitable scintillator for localising neutron capture within a detector

*Balmer, M.J.I, Gamage, K.A.A and Taylor, G.C.*

*Journal of Instrumentation. 9(01):P01007-1-13, January 2014. This is an author-created, un-copyedited version of an article accepted for publication/published in Journal of Instrumentation. IOP Publishing Ltd is not responsible for any errors or omissions in this version of the manuscript or any version derived from it. The Version of Record is available online at doi: 10.1088/1748-0221/9/01/P01007.*

## 4.1 Abstract

Using Monte Carlo modelling, an investigation into a suitable loaded scintillator for localising neutron capture in a novel neutron survey meter has been undertaken. A comparison of estimated neutron capture location in a scintillator with Geant4 and MCNP simulations was undertaken and a good general agreement between the two models was observed. The interactions of gamma emissions from neutron capture in the scintillator are investigated. The results show that the gamma emission from neutron capture will not aid neutron capture localisation and will only inhibit it.

It is observed that the lithium-loaded scintillator has the lowest neutron capture efficiency when compared with boron and gadolinium scintillators. However, it is the most promising of the detectors investigated in this research for use in a novel neutron survey meter design.

## 4.2 Introduction

Previous work has highlighted that by taking into account the direction of incidence of a neutron field, a better estimate of the health risk to an individual exposed to the dose can be achieved [76]. A number of instruments have been previously developed to measure the directional component of a neutron field [90]. However, these instruments do not lend themselves well to portable, real-time applications. It has been identified that a theoretical design proposed by Taylor [84] could be realised into a portable, real-time instrument. The instrument proposed consists of a boron-loaded spherical scintillator of 20.32 cm diameter interrogated by multiple photomultiplier tubes (PMTs). A neutron entering the scintillator will undergo many elastic collisions, before finally coming to rest and being captured by boron.

By recording a large number of neutron capture events within the scintillator, a pattern related to energy and direction of incidence of the neutron field to the detector can be observed. An artificial neural network was trained with data obtained through Monte Carlo simulations and in this proof-of-concept it was shown that an estimate of effective dose could be achieved using this instrument.

However, this proof-of-concept has not yet been realised into a physical instrument. To allow the instrument to be realised into a working detector, a novel technique will need to be identified to localise the neutron capture within the scintillator.

A high photon yield from the scintillator is highly desirable to obtain a good signal to noise ratio of photons from scintillation as a result of neutron capture. The strong quenching in a boron-loaded scintillator greatly reduces the photon yield [86], to a light intensity of 60 keVee (*electron equivalent*). It is anticipated that the interior of the detector would be non-reflective and so considering a typical PMT of around 1-2 cm radius, only a small portion of the scintillation light will be collected by the light detectors around the perimeter of the detector.

In recent developments in the field of crystal scintillators, $Cs_2LiYCl_6$:Ce (CLYC) is perhaps the most promising [87]. CLYC has been shown to have high photon yield, good light transmittance and a lithium loading for neutron capture. However, growing these crystals to the desired sizes is not currently possible [91, 92].

Plastic scintillators are advantageous in many ways, boasting fast response times,

significantly less hazardous materials, low cost of fabrication, and high light yields [93]. However, scaling a plastic detector to a large size has associated problems, a heavier mass compared to that of a liquid scintillator and poor light transmittance due to the loading element [93]. A number of smaller crystal or plastic scintillators could be configured into an array to create a larger detector capable of estimating dose at high energies. However, such an instrument would as well as being significantly more complex, probably prove cost-prohibitive.

A liquid scintillator with a suitable loading for neutron capture shows the most promise for use in this design. The three main choices of loading for neutron capture within a liquid scintillator are boron, lithium and gadolinium due to their high cross-section allowing for efficient neutron capture. This paper will investigate the suitability of a liquid scintillator with each of these loading elements in, with a view to localising neutron capture within the scintillator.

## 4.3 Liquid scintillators for neutron capture

### 4.3.1 Boron-loaded scintillator

Boron-loaded scintillators are typically loaded with up to 5% boron. The boron capture reaction is shown in Equation 4.1 (6% branching ratio) and Equation 4.2 (94% branching ratio).

$$^{1}n + \ ^{10}B \rightarrow \ ^{7}Li + ^{4}He \ (Q - value = 2.79MeV) \tag{4.1}$$

$$^{1}n + \ ^{10}B \rightarrow \ ^{7}Li + ^{4}He + \gamma \ (0.477 \ MeV)(Q - value = 2.31MeV) \tag{4.2}$$

A boron-loaded scintillator presents a promising detector for use in this application with a reasonably high energy $^{4}$He ($\alpha$) emitted as a result of neutron capture. However, as has previously been mentioned, the strong quenching within the scintillator due to the heavy lithium particle from the capture reaction, means that only 60 keVee of light is emitted from neutron capture. For the commercially available BC-523A (with 5% boron loading), this equates to approximately 670 photons being

spread isotropically from the neutron capture location. More recent development of EJ-309:B5 [94] has a higher photon yield of around 120 keVee from neutron capture, equating to around 1380 photons.

Another consideration for a boron-loaded scintillator is the possibility of the 477 keV gamma Compton scattering within the scintillator and presenting a false signal to a capture localising algorithm. It has been noted that in smaller detectors of a 5 cm diameter, this is not a problem [95]. However, for the larger detector volumes being considered within this design, this is worthy of consideration.

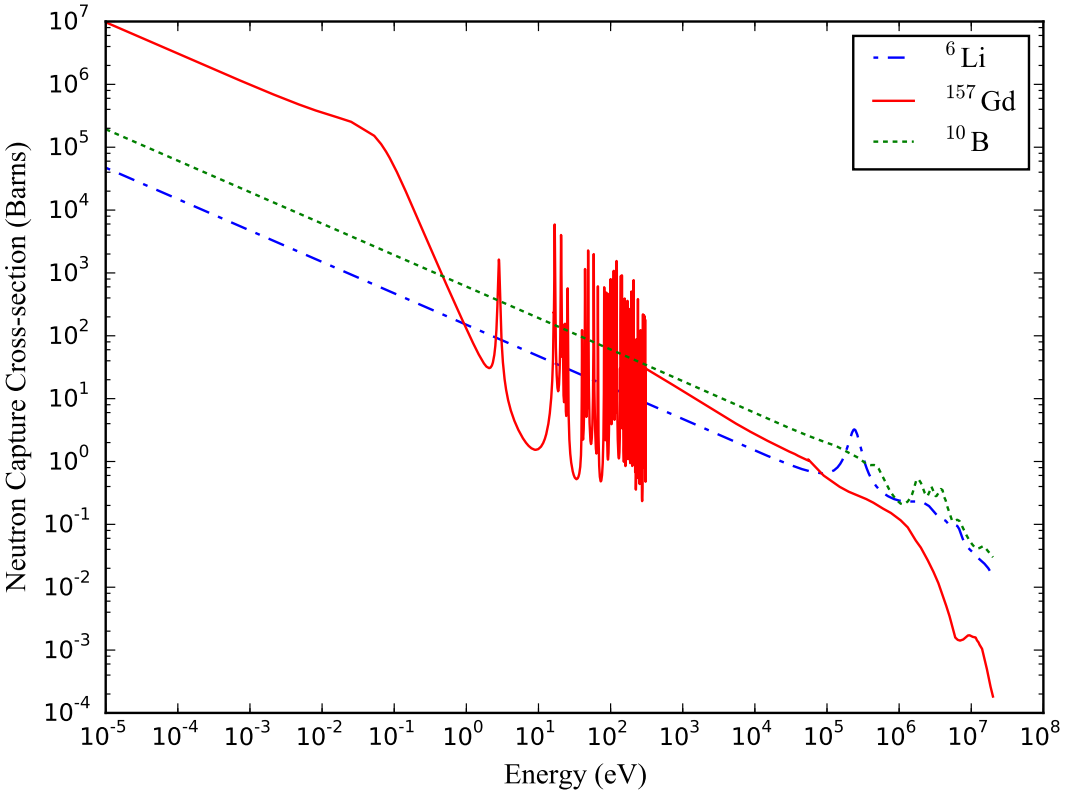


Figure 4.1: Neutron capture cross-section for lithium, boron and gadolinium using data from ENDF/B-VII.r1.

### 4.3.2 Gadolinium-loaded scintillator

With a high cross-section (as shown in Figure 4.1), gadolinium allows for efficient neutron capture detection. Within the scope of this work, the prompt emission of high energy gamma from neutron capture may cause problems with localising neutron capture. This gamma will travel away from the capture location before Compton scattering with an electron. The location of this Compton scattering could be a considerable distance from the location of the neutron capture. With the original proposed design, the capture was voxelised into 2x2x2 $cm^3$ voxels. If a sufficient number of high energy Compton scatters occur less than 2 cm from the neutron capture location, this could make the scintillator worthy of consideration.

### 4.3.3 Lithium-loaded scintillator

The two previous liquid scintillators discussed, emit a gamma as a result of neutron capture. As shown in Equation 4.3, there is no gamma emission from the lithium neutron capture reaction.

$$^1n +^6 Li \rightarrow t\ (2.73\ MeV) + \alpha\ (2.05\ MeV) \tag{4.3}$$

The lack of gamma from neutron capture makes $^6$Li a promising candidate for use in this design. The lighter tritium and $\alpha$ particles from the capture reaction mean that there is less quenching of the scintillation from neutron capture. As a result of this it is estimated ten times as much light is emitted from neutron capture [96].

Of the three loading elements considered within this paper, it can be seen in Figure 4.1 $^6$Li has a significantly lower cross-section. The impact of this is that the previously observed limit of directional capture pattern observed with BC-523A could be much lower. Although no lithium-loaded scintillators are commercially available, previous research has shown that such a scintillator could be manufactured [96, 97].

## 4.4 Detector modelling and simulation

### 4.4.1 Establishing a suitable model of the detector

Monte Carlo simulation codes allow experimental situations to be modelled and evaluated before experimental work is undertaken. These codes are used in a wide range of applications including, high energy physics, medicine, nuclear reactor design through to dosimetry estimations. Arguably, one of the most commonly used Monte Carlo codes for low energy neutron transportation simulation is MCNP [88]. This well established code is considered well bench marked for these low energy neutron simulations. However, the current version of MCNP does not allow for transport of low energy photons (i.e. visible light). Within the scope of this work, modelling of scintillation and low energy photons is highly desirable. Geant4 [98, 99] can be used to simulate both transport of neutrons and photons in a scintillator. The Geant4 toolkit uses the object-orientated programming language C++ and allows the user to write fully customised code.

By using the photon transport models within Geant4, it has previously been possible to model liquid scintillators and to investigate photon production and pulse shapes [100, 101]. However, the detectors that were modelled were concerned with proton recoil energy and did not use loaded scintillators for neutron capture. At lower neutron energies for thermal neutron simulations, there are conflicting results when compared to simulations performed with MCNP [102]. However, no further results have been published since Geant4 v4.9.2. The latest stable release of Geant4 is at v4.9.6.p02. It was felt that for this work, before proceeding with simulations written using Geant4, some comparison should be undertaken between Geant4 and MCNP, focusing on thermal neutrons. By considering the location of neutron capture within the scintillator, this would provide a good comparison of both the higher energy physics models for proton recoil, as well as the lower energy thermal transport of the neutrons.

All simulations under consideration in this work were run on a 3.2 GHz processor running the Linux based operating system, Ubuntu 12.04. The codes used were Geant4 version 4.9.6.p02 and MCNP5 v1.60.

The geometry of the detector simulated can be seen in Figure 4.2. A typical

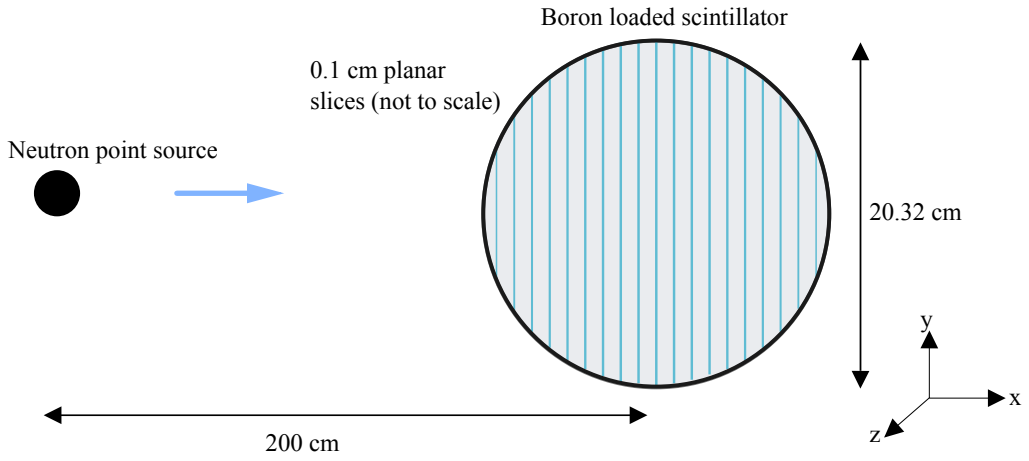


Figure 4.2: Detector geometry under simulation with neutrons emitted in the direction of the x-axis.

boron-loaded scintillator with a density of 0.92 g/cm$^3$ and a diameter of 20.32 cm was placed inside a vacuum. The material fractional masses listed in Table 4.1 were chosen to be that of a typical boron-loaded scintillator used for neutron capture such as BC-523A. The centre of the spherical scintillator was at coordinate (0,0,0) cm. A monoenergetic, mono directional source was located at (-200, 0, 0) cm, emitting neutrons in the direction of the x-axis.

Table 4.1: Fractional mass composition of a typical boron-loaded liquid scintillator of density 0.92 g/cm$^3$.

| Element | C | H | O | $^{10}$B | $^{11}$B |
|---|---|---|---|---|---|
| Fractional mass | 0.624 | 0.09 | 0.236 | 0.045 | 0.005 |

Geant4 allows for full customisation of the simulation through a series of compulsory and non-compulsory C++ classes. A custom physics list was created for the simulations. The high-precision neutron physics models were chosen for the simulation of neutrons from thermal to an upper energy range of 20 MeV. The following Geant4 physics was included; *G4NeutronHPElastic*, *G4NeutronHPInelastic*, *G4NeutronCaptureAtRest* and *G4NeutronHPCapture*. The neutron cross-section data in the Geant4 G4NDL4.2 library, is largely based on ENDF/B-VII.r1.

*G4NeutronThermalScattering* was used with a thermal treatment of hydrogen using the *G4Element TS_H_of_Polyethylene*. A minimum energy of 4 eV was set

for the elastic scattering and maximum energy of 4 eV for thermal scattering.

In MCNP materials were simulated using the ENDF/B-VII.0 neutron cross-section tables at temperature 293.13 K. To handle low energy thermal scattering of neutrons below 5 eV, MCNP has thermal treatment for hydrogen in polyethylene. For s($\alpha$, $\beta$) thermal treatment, *poly.01t* was included in the MCNP input file. It was observed that all simulations using MCNP had a statistical uncertainty of less than 0.01%. Using the particle tracking file (PTRAC), neutron capture events were counted, recording the (x, y, z) location in cm of the neutron capture within the detector. It is noted that Geant4 and MCNP interpolate the ENDF neutron cross-section data with a different number of data points.

### 4.4.2 A comparison of neutron capture location using Geant4 and MCNP

Identical geometries and material specifications were modelled to allow comparison of the two codes. Both simulation codes were configured to record the three dimensional neutron capture location within the scintillator. To minimise statistical variation, every simulation recorded at least $10^6$ neutron capture events. Planar slices 0.1 cm thick along the x-axis of the detector were created and neutron capture within these slices was counted.

Table 4.2: The table shows testing correlation of the polynomial fitting function to the data. The $r^2$ value is provided to show the closeness of fit of Geant4 and MCNP at each neutron source energy simulated.

| Energy keV | Pearson correlation coefficient between fit and data | | $r^2$ value |
|---|---|---|---|
| | Geant4 | MCNP | |
| 100 | 0.9909 | 0.9911 | 0.9929 |
| 300 | 0.9922 | 0.9919 | 0.9954 |
| 600 | 0.9914 | 0.9913 | 0.9964 |
| 900 | 0.9904 | 0.9904 | 0.9966 |
| 1200 | 0.9897 | 0.9894 | 0.9972 |

Figure 4.3 shows the neutron capture location along the x-axis, for 100 keV, 300 keV, 600 keV, 900 keV and 1200 keV neutron sources, using MCNP and Geant4. A $17^{\text{th}}$ order polynomial fitting function was used for the data sets. An example

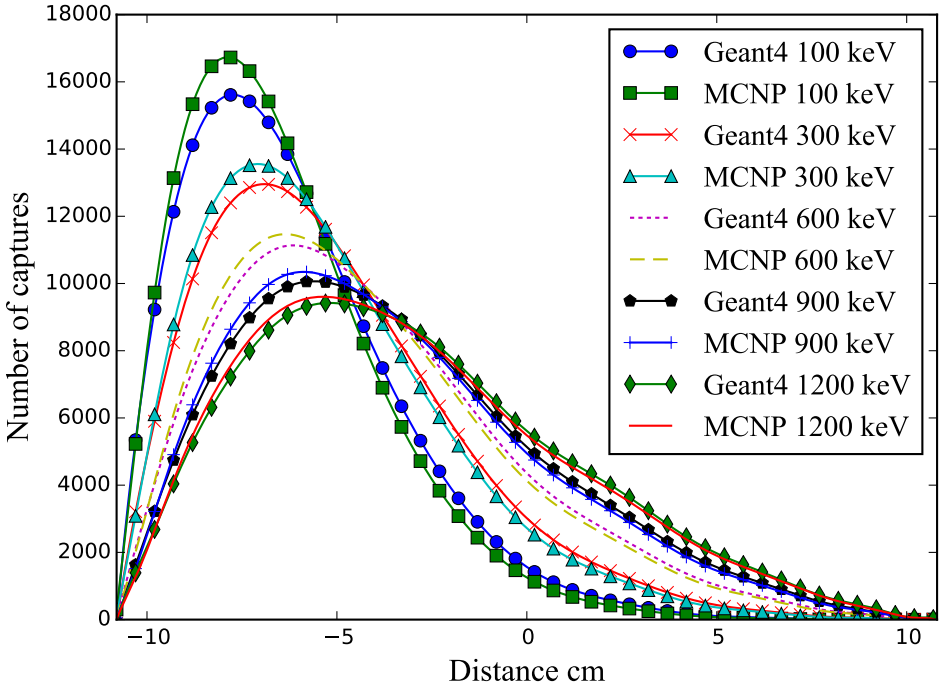


Figure 4.3: A comparison between MCNP and Geant4 of neutron captures recorded in 0.1 cm slices for 100 keV, 300 keV, 600 keV, 900 keV and 1200 keV neutron sources.

of the spread of the data can be seen in Figure 4.4. Lower order polynomials were investigated but a satisfactory fit was not found. Due to the non linear nature of the data set a Pearson correlation coefficient test was used to ensure that the fitting function had a suitable fit with each data set. The outcome of a Pearson correlation coefficient test is a coefficient between 0 and 1, where a number approaching 1 signifies a strong correlation between the two variables and 0 signifies no correlation. It can be seen from Table 4.2 that for each of the neutron energies a good polynomial fit has been achieved.

For numerical analysis of the fit between Geant4 and MCNP, at each energy, a linear regression test was performed for each neutron source energy. Figure 4.5 shows an example of the linear regression test undertaken for each neutron source energy. The number of neutrons captured in each slice was plotted on the x-axis for MCNP and the y-axis for Geant4. If the two models were to output exactly

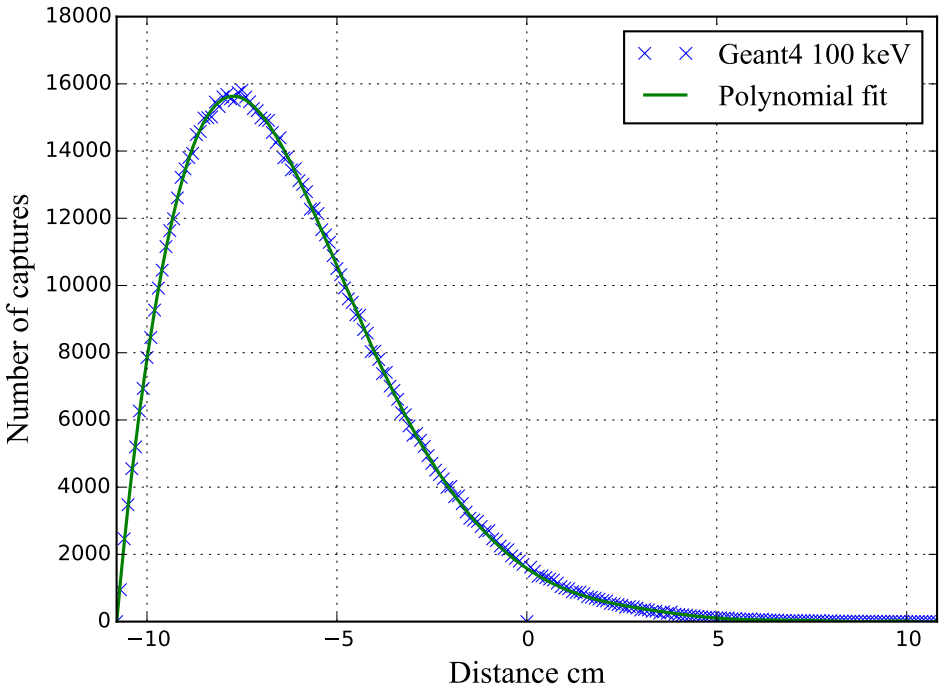


Figure 4.4: Neutron captures recorded in 0.1 cm slices for 100 keV. The data was fitted using a polynomial fitting function.

the same data, the graph would perfectly fit the line of y=x. Linear regression was tested between the two variables (MCNP and Geant4 data) and the expected value of y=x. The $r^2$ value for each neutron source energy can be seen in Table 4.2.

From Table 4.2 and Figure 4.3 it can be seen that Geant4 and MCNP are in general agreement in terms of neutron capture with respect to depth in the detector. From the $r^2$ values in Table 4.2 it can be seen that at lower energies there is less agreement between the two models. It can be seen in Figure 4.3 that the location along x-axis of the neutron capture are in agreement, however, it can be seen that Geant4 estimates fewer neutron captures at this peak capture location. Geant4 estimates that more neutrons will be captured further along the x-axis into the scintillator.

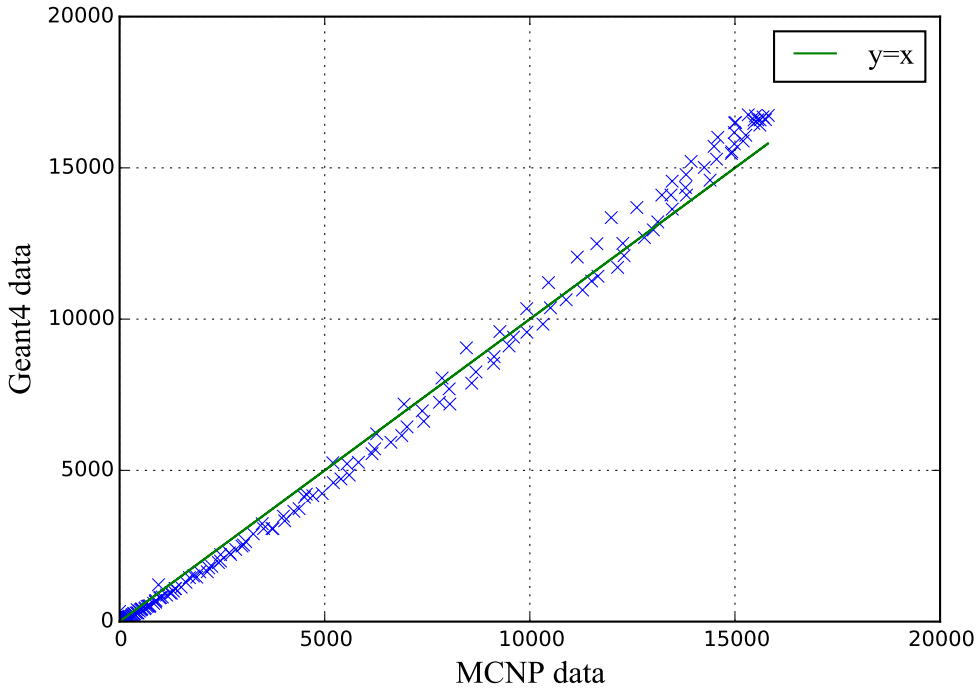


Figure 4.5: A comparison of neutron captures in 0.1 cm slices through the detector models in Geant4 and MCNP for a 100 keV source. The line y=x is set as the ideal, whereby both models respond with the same number of neutron captures. The magnitude of the difference between this observed and ideal response was tested using linear regression techniques.

## 4.5 Investigating a suitable liquid scintillator

In order to assess the suitability of different loading materials in a scintillator for this application, a number of factors must be taken into consideration. Perhaps the most important factor is the investigation of gamma ray emission from capture. It has previously been noted that for boron-loaded scintillators investigating neutron capture, with a detector of size under consideration in this study, there is a 78% chance of a gamma interaction in the scintillator resulting in greater than 50 keV being deposited [95]. Within the scope of this work, it is necessary to not only understand the probability of a gamma interaction, but also to understand the likelihood of where this event will occur, and the likely energy that will be deposited.

The impact of a Compton scatter of a gamma within a detector impeding the ability to localise neutron capture is not currently fully understood. However, within the scope of this work it has been decided to investigate which scintillator exhibits the lowest frequency of gamma interaction within the scintillator as a function of distance from the neutron capture location.

Capture efficiency of the detector is also of importance, particularly in a large size detector. A low capture efficiency may impede the instrument's ability to detect the energy and/or direction of the neutron field under investigation. It can be seen in Figure 4.1 that the neutron capture cross-section of $^{6}$Li is significantly lower than the two other loading elements considered in this research. It was felt necessary to investigate the impact of this on the neutron capture efficiency of the scintillator.

### 4.5.1 Simulation parameters

Table 4.3: Fractional mass composition of lithium and gadolinium scintillators simulated in this work.

| Element | Fractional mass % for Gd loading | Fractional mass % for $^{6}$Li loading |
|---|---|---|
| C | 0.8525 | 0.858 |
| H | 0.1228 | 0.105 |
| O | 0.0144 | 0.0304 |
| N | 0.0003 | 0.0026 |
| Loading | 0.01 | 0.004 |

The same model detailed in Figure 4.2 was used for the simulations undertaken in this section. The boron-loaded scintillator used was the same as that shown in Table 4.1. The gadolinium and lithium-loaded scintillators were based on cocktails described in [97, 103], these are shown in Table 4.3. These scintillator compositions were chosen as ones which have proven ability and could be suited for use in this work. Each of the scintillators were given a density of 0.92 g/cm$^3$. Differences in neutron capture efficiency have previously been noted between MCNP and Geant4 simulations [102]. It was decided, for neutron capture efficiency simulations, to use both codes to ensure that the general trend was the same between the two codes.

### 4.5.2 Neutron capture efficiency

To investigate the capture efficiency of the detector, a neutron was emitted from a point source at -200, 0, 0 towards the detector in a single event, where 2x10$^6$ events were simulated for each detector. Neutron energies of 100 keV, 1 MeV and 10 MeV were simulated for the three different scintillators. The number of neutrons captured were recorded using Geant4 and MCNP. The neutron capture efficiency was defined as number of captures, divided by the total number of neutrons simulated (including neutrons which escaped without capture). The statistical uncertainties were observed to be less than 0.001% for these simulations.

### 4.5.3 Gamma interaction in scintillator

The Geant4 *General Particle Source* was used to generate the source particle a gamma, with isotropic emission for investigation of gamma interactions in the scintillator. For each scintillator loading, a different gamma energy was simulated. In 94% of neutron capture events by boron, a gamma is emitted, making this the most important gamma energy to consider for this scintillator.

In a lithium-loaded scintillator, although a significantly lower cross-section (0.33 Barns), hydrogen capture will lead to emission of a 2.2 MeV gamma. The resultant 2.2 MeV gamma from this hydrogen neutron capture was used for the lithium simulations. With gadolinium a number of prompt gamma emissions occur as a result of neutron capture, 1 MeV, 2 MeV and 7.5 MeV gamma energies were chosen for simulation this scintillator loading.

The location of the particle source was chosen at (0, 0, -5) and 2x10$^6$ events were simulated for each detector. Previous work [90] has shown that for neutron energies from 10 keV to 1 MeV this front region of the detector is the most likely location for neutron capture to take place. The number of gamma escaping the detector without any interaction within the detector was recorded. When a gamma did Compton scatter in the detector, the resulting electron energy was recorded as well as the distance from the origin of the gamma.

## 4.6 Results

The capture efficiency of the different scintillators can be seen in Table 4.4. It can be seen that the higher loading by mass of boron equates to a similar loading capture efficiency of the lower percentage loading of gadolinium. As would be expected, with the lowest cross-section of the three loading elements, lithium, has the lowest capture efficiency. As has previously been observed [102] there is a difference of around 5% between MCNP and Geant4 in terms of neutron capture efficiency. Although the absolute efficiencies are observed to be different between the two codes, it can be seen that there is a good agreement between the two codes in terms of the trend for neutron capture efficiency against energy, for each scintillator simulated. The reason for these differences is thought to be in the way the two codes handle weight cut off of neutrons.

Table 4.4: Neutron capture efficiency for neutron energies of 100 keV, 1 MeV and 10 MeV. All values given are percentages.

| Loading | Simulation Code | 100 keV | 1 MeV | 10 MeV |
|---|---|---|---|---|
| Lithium | MCNP | 40.4 | 49.7 | 18.1 |
| | Geant4 | 34.4 | 38.2 | 21.2 |
| Boron | MCNP | 63.4 | 52.7 | 17.0 |
| | Geant4 | 56.7 | 48.5 | 20.3 |
| Gadolinium | MCNP | 50.9 | 55.9 | 23.7 |
| | Geant4 | 53.5 | 57.6 | 29.8 |

Table 4.5: Percentage of gamma particles escaping the detector without under going a Compton scattering event.

| Scintillator loading | gamma energy used for simulation | Percentage of gamma escaping without interaction |
|---|---|---|
| Boron | 478 keV | 42 ± 0.11 |
| Gadolinium | 1 MeV | 52 ± 0.10 |
| Gadolinium | 2 MeV | 64 ± 0.09 |
| Gadolinium | 7.5 MeV | 80 ± 0.08 |
| Lithium | 2.2 MeV | 66 ± 0.09 |

Within the boron-loaded scintillator, it can be seen in Table 4.5 that 42% of the 478 keV gamma emitted from neutron capture by boron escape without interactions.

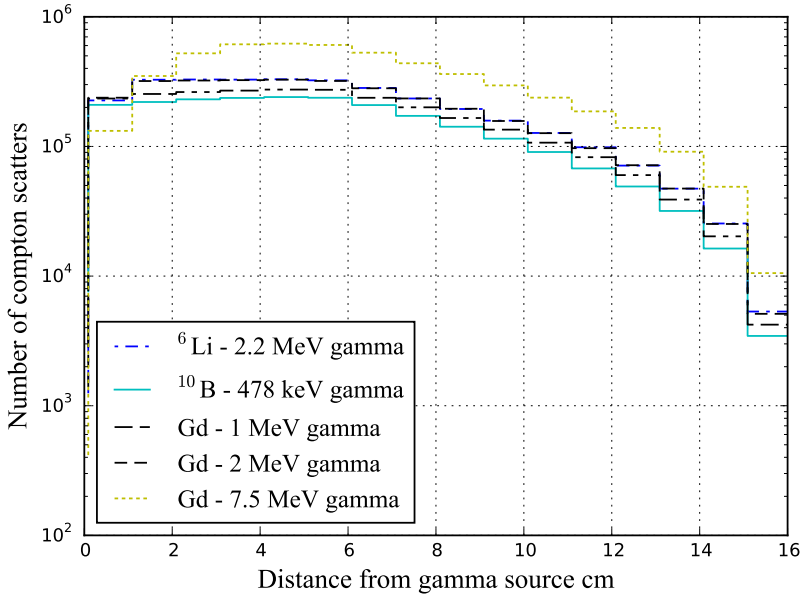


Figure 4.6: Investigating distance of Compton scatter from the gamma source within a liquid scintillator with three different loadings; boron, lithium and gadolinium.

Figure 4.6 and 4.7 show there is a high probability of this particle interacting and depositing a significant amount of energy greater than 2 cm away from the neutron capture location. As a result of these gamma interactions in the scintillator, multiple scintillations will occur in the scintillator. It may not be possible to localise neutron capture from multiple scintillation events.

For a gadolinium-loaded scintillator, it can be seen that as the gamma emission energy increases the probability of the gamma interacting in the detector reduces. However, it can be seen in Figure 4.6 and 4.7 that there is a high probability of this gamma interacting more than 2 cm from the neutron capture location. It can be seen that it would be impossible to localise neutron capture in a gadolinium scintillator from the gamma Compton scattering in the scintillator.

In the lithium-loaded scintillator hydrogen capture is a low probability. It can be seen that the unwanted 2.2 MeV gamma from this capture reaction escapes the scintillator 66% of the time without interaction. This further reduces the impact of a low probability neutron capture by hydrogen.

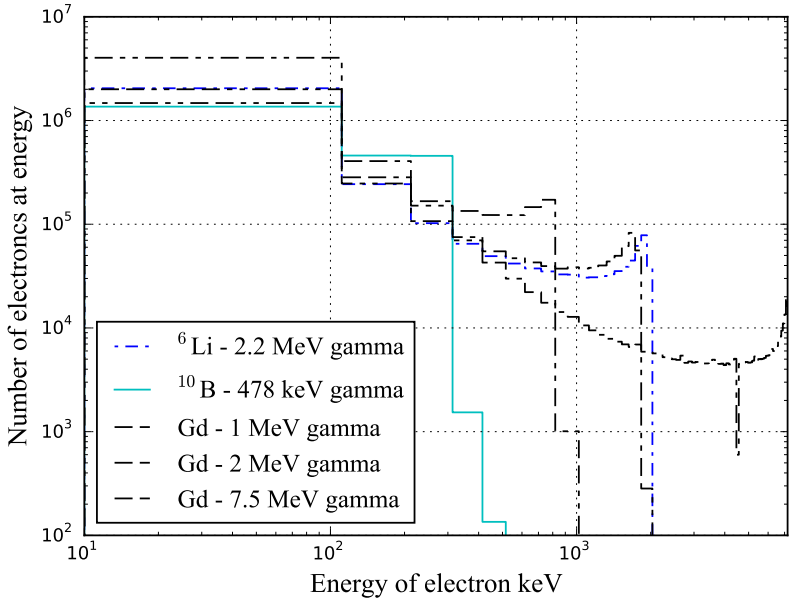


Figure 4.7: Energy of electron Compton scattered by gamma within a liquid scintillator with three different loadings; boron, lithium and gadolinium.

## 4.7 Conclusion

In this work, three different loading elements have been considered for use in a scintillator suitable for localising neutron capture. Before any simulations were undertaken to investigate the suitability of these detectors, a comparison of Geant4 was undertaken against MCNP to validate the detector model written within Geant4. It was shown that the two models were in general agreement with each other, when considering the neutron capture against depth in the scintillator. In future work when establishing a method of localising neutron capture in the scintillator, comparisons of predicted neutron capture location against simulated data will be crucial. Comparison will be able to now be undertaken with confidence in the simulated data due to the general agreement of the two models.

Although gadolinium has a high cross-section for neutron capture, the prompt gamma emission from neutron capture has been shown to Compton scatter too far away from the neutron capture location to allow the capture to be localised. With a boron-loaded scintillator a major disadvantage is that the gamma emission from

94% of captures, of which 42% of these will Compton scatter within the detector. In such cases, the impact would either be false location of the neutron capture, or if a suitable pulse height gating algorithm could be employed, a reduced efficiency of the detector. Achieving good pulse shape discrimination on such small pulses of light could prove difficult which would also reduce the detector efficiency.

The most promising of the three scintillators investigated in this work is the $^{6}$Li-loaded liquid scintillator. The lack of gamma from a neutron capture reaction and high energy, light, particles emitted from this reaction make it a promising choice for this work. It has also been shown that although lithium has a lower cross-section, compared with boron, it still has satisfactory neutron capture efficiency. However, it is worth noting that currently no commercially available $^{6}$Li-loaded liquid scintillator exists. Developing a suitable scintillator and characterising such a scintillator would need to take place to establish its suitability.

# Chapter 5

# Detecting energy dependent neutron capture distributions in a liquid scintillator

*Balmer, M.J.I, Gamage, K.A.A and Taylor, G.C.*

*Nuclear Instruments and Methods in Physics Research Section A Accelerators, Spectrometers, Detectors and Associated Equipment. 776:1-7, March 2015.*

## 5.1 Abstract

A novel technique is being developed to estimate the effective dose of a neutron field based on the distribution of neutron captures in a scintillator. Using Monte Carlo techniques, a number of monoenergetic neutron source energies and locations were modelled and their neutron capture response was recorded. Using back propagation Artificial Neural Networks the energy and incident direction of the neutron field was predicted from the distribution of neutron captures within a $^{6}$Li-loaded liquid scintillator. Using this proposed technique, the effective dose of $^{252}$Cf, $^{241}$AmBe and $^{241}$AmLi neutron fields was estimated to within 30% for four perpendicular angles in the horizontal plane. Initial theoretical investigations show that this technique holds some promise for real-time estimation of the effective dose of a neutron field.

## 5.2 Introduction

The radiation protection quantity *effective dose* can be used to provide an estimation of the health risk due to exposure to a neutron field [18]. Using this quantity, the risk estimate accounts for both energy and direction of incidence of a neutron field. Using conversion coefficients, a neutron fluence can be transformed into an effective dose for a given incidence of the neutron field, by applying fluence to effective dose conversion coefficients that change with energy and angle [18].

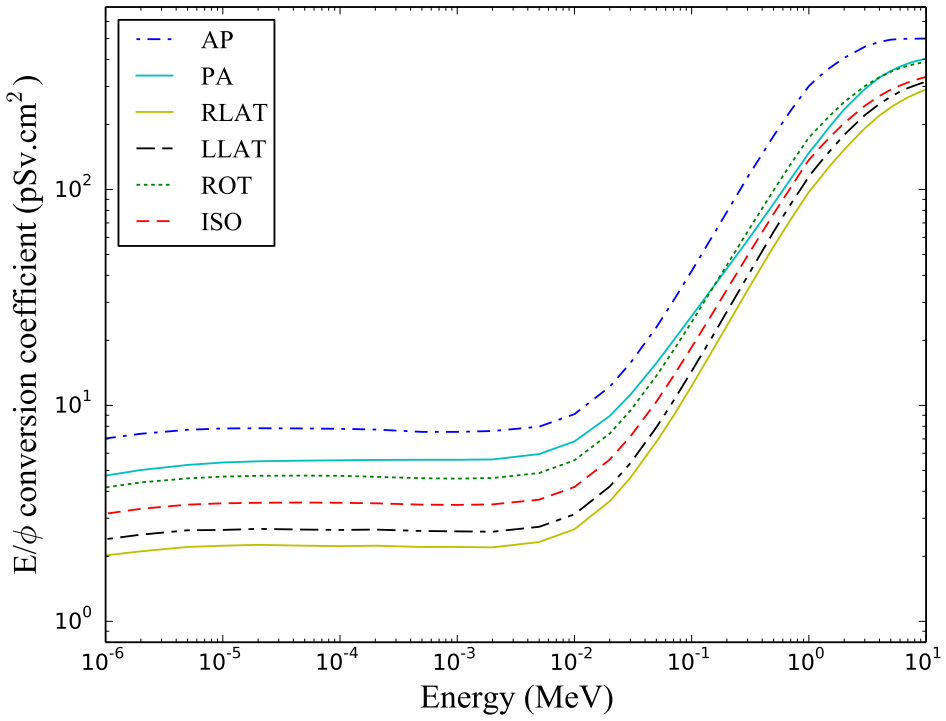


Figure 5.1: Effective dose coefficients for AP, PA, RLAT, LLAT, ROT (rotational) and ISO (isotropic) are shown. The coefficients used were taken from the latest ICRP recommendations [18].

Figure 5.1 shows how the effective dose coefficients change for antero-posterior (AP), postero-anterior (PA), left-lateral (LLAT) and right-lateral (RLAT) incident radiation. It can be seen that the greatest health risk is experienced with the AP direction of incidence, while the lowest risk is with RLAT incidence. Existing neu-

tron survey techniques measure the isotropic dose quantity, *ambient dose equivalent H*(10)*. This dose quantity is used for neutron surveys as it is designed to account for the worst case of the health risk. Although effective dose cannot be measured, previous research has discussed the possibility of using instrumentation to *estimate* effective dose in real-time to understand the human health risk accounting for the anisotropic nature of a neutron field [84].

A proof of concept for an instrument consisting of a boron-loaded spherical scintillator of 20.32 cm diameter interrogated by multiple photomultiplier tubes (PMTs) has already been undertaken [84]. When a neutron interacts in a liquid scintillator it will undergo a number of elastic collisions. These elastic collisions can be detected by the particle recoil from the collision, causing scintillation of photons proportional to the energy lost to the recoiling particle. If a neutron loses enough energy in the scintillator through these collisions, it is likely it will be captured, if a high neutron capture cross-section element is present in the scintillator. The energy from this capture reaction remains constant for a given loading element, therefore the light production for a neutron capture remains constant.

By interrogating the scintillator with a number of PMTs, differing numbers of photons will be detected depending on the location of the neutron capture event in the scintillator. By making the interior of the scintillator non-reflective it is thought the detection of these differences will become easier. This novel concept is shown in Figure 5.2. Six photomultiplier tubes are shown, placed equidistantly around the perimeter of the spherical scintillator.

Using Monte Carlo simulation techniques, the location of a large number of neutron capture events within the scintillator was recorded. A pattern relating to energy and direction of incidence of the neutron field to the detector was observed. An example of the neutron capture distribution's dependency on energy can be seen in Figure 5.3. It can clearly be seen that differing energies of neutron source exhibit a different pattern of distribution of neutron capture within the scintillator. An artificial neural network was trained with data obtained through Monte Carlo simulations and in this proof-of-concept it was shown that an estimate of effective dose could be achieved using this instrument. However no investigation was undertaken to detect the locality of the neutron capture in the scintillator.

Initial investigations into the design of a novel technique to detect the pattern

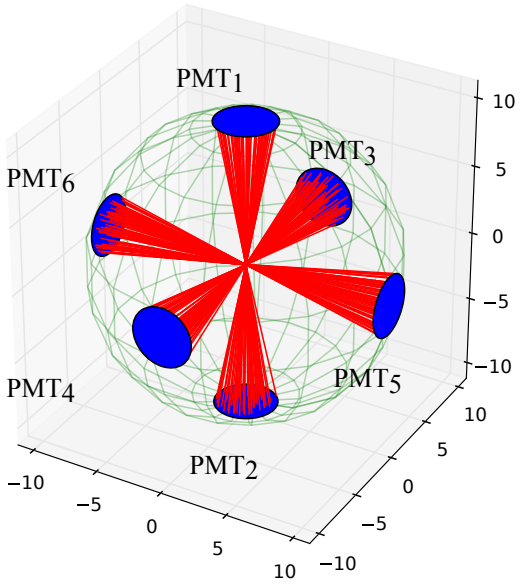


Figure 5.2: Scintillation from a neutron capture in the spherical scintillator described in this work. The six PMTs shown detect different amounts of light depending on the location of the neutron capture in the scintillator. The interior of the scintillator is coated with a non-reflective coating, so photons which do not hit a PMT are absorbed.

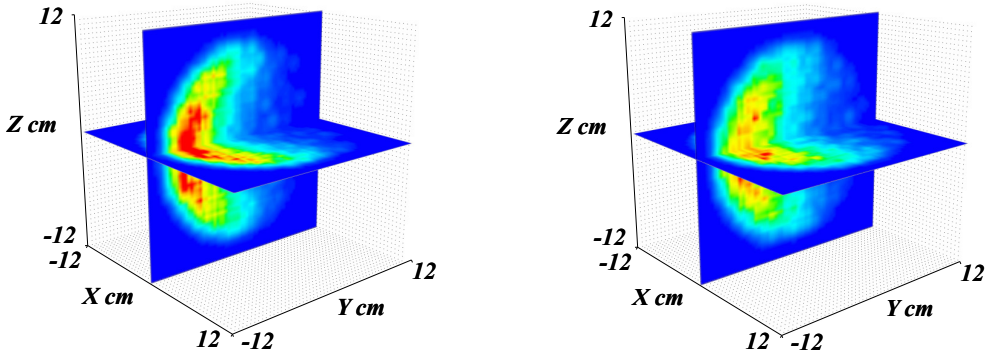


Figure 5.3: Distribution of neutron captures within a 10.8 cm radius $^{6}$Li-loaded scintillator exposed to two different monoenergetic neutron energies, (a) 10 keV and (b) 100 keV, plots drawn using the Mayavi software library [89].

of neutron capture has been undertaken [104]. This research investigated a suitable scintillator for use in this work, focusing on gadolinium, lithium and boron loaded

liquid scintillators. The most promising of the detectors considered was a $^{6}$Li-loaded liquid scintillator.

$$^{1}n + \ ^{6}Li \rightarrow t\ (2.73\ MeV) + \alpha\ (2.05\ MeV) \tag{5.1}$$

As shown in Equation 5.1, two light particles are emitted as a result of neutron capture. These ionising particles deposit their energy close to the capture location within the scintillator. These light particles mean that less quenching of the scintillation will occur when compared to the light yield of a boron loaded liquid scintillator. It is also of note that there is no gamma emission from the lithium neutron capture reaction. Therefore all products of the capture reaction can be considered useful signals.

Previous investigations into $^{6}$Li-loaded scintillators have shown the detected capture signal to be around 470 keVee (*electron equivalent*) [97]. However, the design of the detector proposed in the scope of this research is such that only a fraction of this light will be collected. It is anticipated that the interior of the detector would be non-reflective and so considering six PMTs of 2.5 cm radius, located equidistantly around the perimeter of a 10.8 cm radius detector (as shown in Figure 5.2) only eight percent of the light will be detected for a scintillation event at the centre of the scintillator. This equates to a detected signal of 44 keVee. The anticipated low light level collection will hinder the ability to discriminate desired detection events (neutron captures), from gamma and proton recoil interactions in the scintillator. It is therefore of interest to investigate a smaller sized scintillator to maximise light collection for pulse shape discrimination (PSD).

This paper looks at the design of a novel method to translate a number of neutron captures in a scintillator into an effective dose. Two different scintillators of radii 7.5 cm and 10.8 cm were investigated. The larger size was chosen as it was the original proposed size, similar to that of existing neutron survey instruments. The smaller 7.5 cm was chosen for the improved light collection from neutron capture. The ability to determine neutron source energy and incidence are investigated, as well as the effective dose for PA, AP, LLAT and RLAT incident radiation.

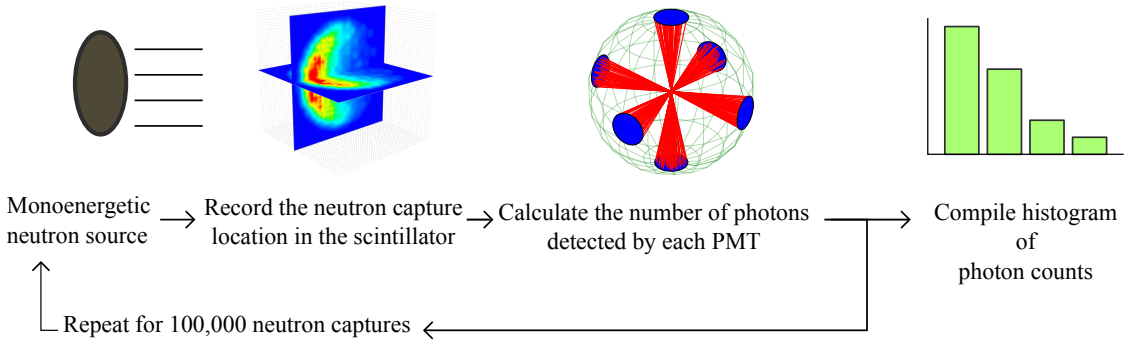


Figure 5.4: System level schematic diagram of the simulations undertaken. Using Monte Carlo simulation tools, a monoenergetic neutron source emitted a neutron towards the scintillator, if this neutron was captured, the light detected by each PMT was estimated. This was repeated for multiple capture events to build a directional, energy dependent response.

## 5.3 Methodology

Early investigations into the design of this instrument attempted to localise every individual neutron capture event. However, no satisfactory method was found to localise individual neutron captures. These investigations did however provide the basis for the novel method proposed in this paper. This research investigates the potential for utilising the different light level distributions recorded by each PMT for a number of neutron capture events in a scintillator without attempting to reconstruct the capture locations. In this work, 100,000 neutron capture events were investigated for each neutron source energy and location. The method holds promise to be robust with regard to noise on each individual scintillation pulse by collecting a large number of neutron capture events. This simple approach also lends itself well to deployment into a portable real-time system using a field programmable gate array (FPGA) to carry out the processing. This approach is shown in Figure 5.4.

### 5.3.1 Monte Carlo simulation parameters

For investigation of a large number of neutron source energies the Monte Carlo radiation transport code package, MCNP v5.0, was used to simulate neutron capture within a $^{6}$Li-loaded scintillator [88]. The composition of the scintillator is shown in

Table 5.1: Fractional mass composition of a typical $^{6}$Li-loaded liquid scintillator of density 0.92 g/cm$^3$.

| Element | C | H | O | N | $^{6}$Li |
|---|---|---|---|---|---|
| Fractional mass | 0.858 | 0.105 | 0.0304 | 0.0026 | 0.004 |

Table 5.1. Previous simulations using MCNP to investigate neutron capture location in a scintillator have been shown to be in agreement with the results obtained using a second simulation package, Geant4 [99, 98, 104].

In MCNP materials were simulated using the ENDF/B-VII.0 neutron cross-section tables at temperature 293.13 K. To handle low energy thermal scattering of neutrons below 5 eV, MCNP has thermal treatment for hydrogen in polyethylene. For s($\alpha$, $\beta$) thermal treatment, *poly.01t* was included in the MCNP input file. Using the particle tracking file (PTRAC), neutron capture events were counted, recording the (x, y, z) location of the neutron capture within the detector. The simulations were run for 100,000 neutron capture events. A planar disc, equal to the radius of the scintillator, was used to simulate 22 monoenergetic neutron sources of differing energy, ranging from 15 keV to 5 MeV. The upper energy range was selected due to the isotropic pattern observed in a scintillator of this size as these energy limits are approached [90], when using a 10.8 cm radius detector. For the same reasons, for the 7.5 cm radius detector an upper energy limit of 1 MeV was set, thereby reducing the number of monoenergetic neutron source energies to 14. For each monoenergetic neutron source energy investigated, the source was rotated around the centre of the scintillator at (0, 0, 0) on a radius of 200 cm, to 28 locations in the $4\pi$ region around the sphere.

### 5.3.2 Photon transport simulation

It is approximated that a neutron capture at the centre of the spherical scintillator (at the Cartesian coordinate shown in Equation 5.2) will yield 470 keVee of light.

$$(x_{capture},\ y_{capture},\ z_{capture}) = (0, 0, 0) \tag{5.2}$$

This light yield is approximated to 1200 photons, which are spread isotropically from the cartesian coordinate shown in Equation 5.2). After travelling distance $r$,

each photon will either be absorbed in the non-reflective coating on the interior of the scintillator housing, or detected by a PMT, at spherical coordinate ($\theta$, $\phi$ and $r$). The azimuthal angle is denoted by $\theta$ and the polar angle $\phi$, for example, for PA incidence the spherical angles are ($\pi$, 0). To specify the isotropic spreading of these photons over the $4\pi$ surface of the sphere, 1200 equidistant points were created. This was acheived using a probability density function sampling $\theta$ and $\phi$ over the ranges [0, $2\pi$] and [0, $\pi$] respectively. Each of these $n$ locations were then be found using Equations 5.3, 5.4 and 5.5.

$$x_n = r\ sin\ \theta\ cos\ \phi \tag{5.3}$$

$$y_n = r\ sin\ \theta\ sin\ \phi \tag{5.4}$$

$$z_n = r\ cos\ \theta \tag{5.5}$$

Consider a PMT at the coordinate given in Equation 5.6. This PMT is located on the plane described by Equation 5.7 described by the arbitary coefficients *(a,b,c)*.

$$(x_{pmt},\ y_{pmt},\ z_{pmt}) \tag{5.6}$$

$$ax + by + cz + d = 0 \tag{5.7}$$

The point of intersection of the photon trajectory with the plane occurs at the coordinates given in Equations 5.8, 5.9, 5.10, where t is an arbitary variable.

$$x_{intersect} = x_{capture} + (t(x_n - x_{capture})) \tag{5.8}$$

$$y_{intersect} = y_{capture} + (t(y_n - y_{capture})) \tag{5.9}$$

$$z_{intersect} = z_{capture} + (t(z_n - z_{capture})) \tag{5.10}$$

By solving the simultaneous Equations 5.8, 5.9 and 5.10, $t$ is found. The distance between the point of the photon trajectory intersection with the plane and the PMT location is calculated. If the distance is less than the radius of the PMT viewing window, this is recorded as a detected photon. The quantum efficiency of the PMT

is assumed to be accounted for in the photon yield estimation.

The algorithm described above was implemented using a custom written C program. This algorithm was automated to record the number of photons detected by a given number of PMTs for a given location of scintillation event within the spherical detector. For the investigations in this work a PMT radius of 2.2 cm was chosen. It is assumed that the PMT is directly coupled to the scintillator and no light guide is used.

The number of photons detected by each PMT was normalised to half the photon yield, as this is the theoretical maximum number of photons that can be detected by each PMT (given a capture infinitessimally close to the PMT). The frequency distribution of this normalised photon count was then placed into 8 data bins of 0.01 (20 photons) intervals, the 9th data bin covered 0.09 to 1.0. It was felt that in the detection region of fewer than 20 photons for a single PMT could be problematic during experimental situations. For this reason the data bin covering 0 to 0.01 was also omitted.

Figure 5.3(b) visualised 100,000 neutron captures for a 100 keV monoenergetic source the number of photons detected by each PMT for this simulation is shown in Figure 5.5. It can be seen there is a large difference between $PMT_3$ and $PMT_4$ therefore it can be assumed that a large number of neutron captures occurred closer to $PMT_4$ than $PMT_3$. Inspection of $PMT_5$ and $PMT_6$ shows similar number of photons detected by each PMT respectively. From this information, the direction of incidence of the neutron field can be correlated to the number of photons counted by each PMT.

## 5.4 Artificial neural network approach

Artificial neural networks (ANNs) are well proven for their abilities in pattern recognition systems. Once a neural network has been trained, the trained network can be deployed into a fast real-time system. Given the benefits of an ANN it was decided to use the C based software library FANN, version 2.2.0 for the investigations in this work [105].

For complicated pattern recognition in multiple dimensions, the back propagation neural network is the most widely applied neural network technique [69]. The

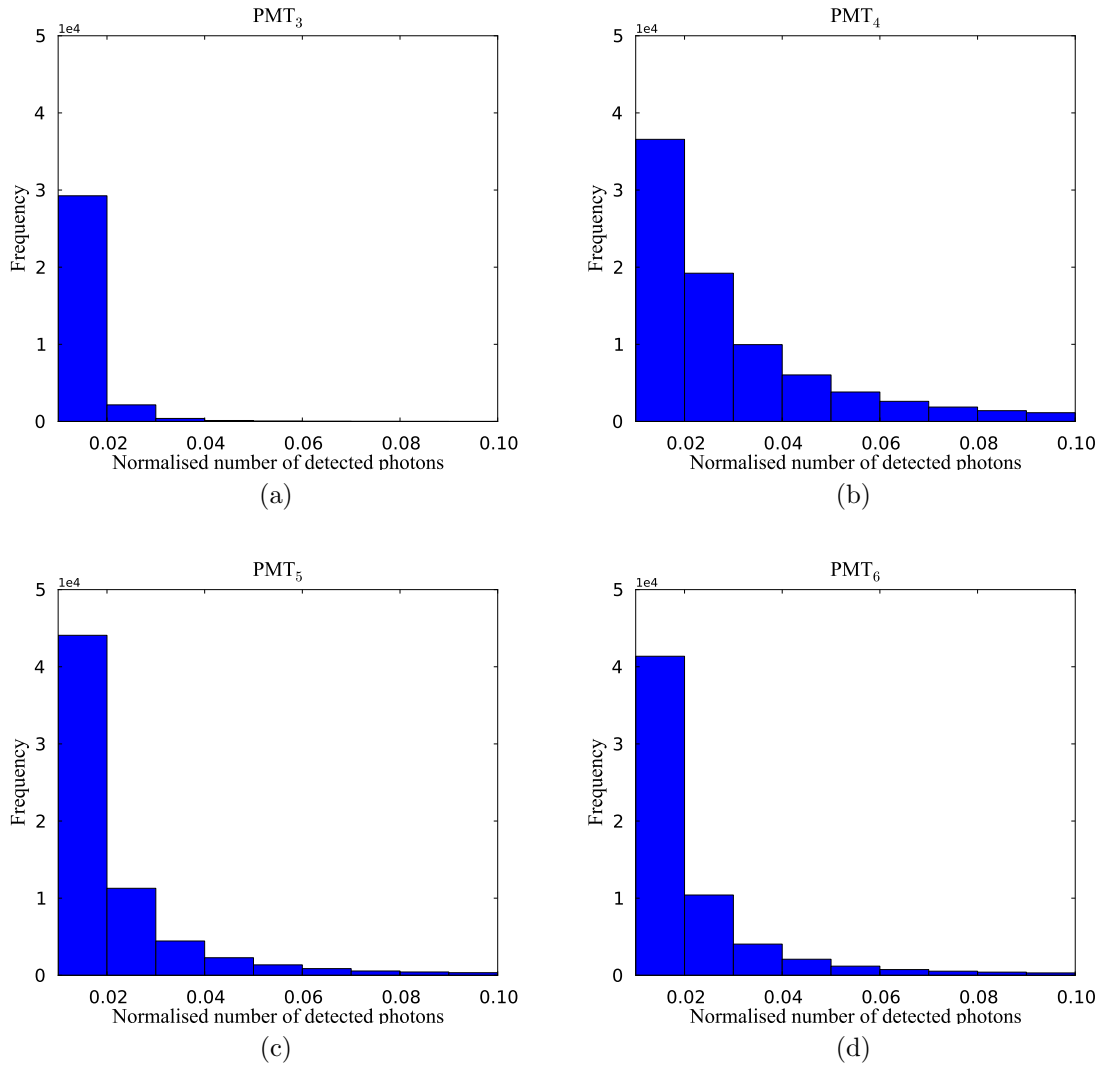


Figure 5.5: Histogram of the number of photons detected by each PMT. It can be seen that $PMT_5$, $PMT_6$ show similar numbers of photons detected by each PMT. Examining the area of the detector furthest from the neutron source $PMT_3$, exhibits the lowest count. Although $PMT_1$ and $PMT_2$ are not shown, the histograms are similar to those of $PMT_5$, $PMT_6$.

network is flexible and can be adapted to different situations by changing the network configuration. Learning coefficients, number of layers, number of neurons and activation functions can all be changed for a given set of input data to optimise the learning of the pattern. Early investigations using an ANN to predict both energy

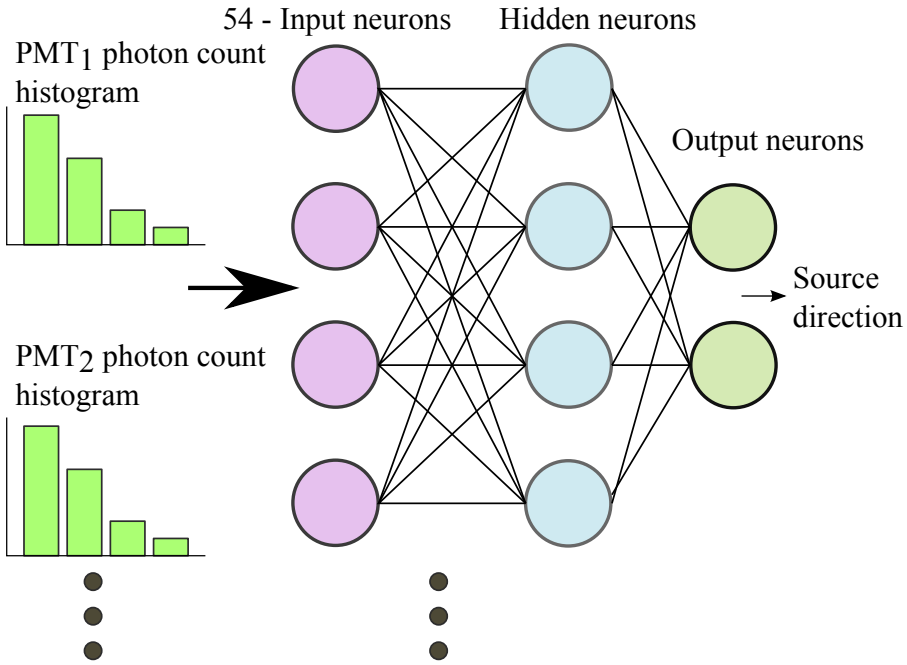


Figure 5.6: Schematic of the back propagation ANN used in this research to estimate the incidence of neutron field to the detector.

and direction with the same network were found to less successful than two separate ANNs for this purpose. The two networks estimated neutron source energy and neutron incidence respectively. The architecture of the network used in this work for estimating the direction of incidences is shown in Figure 5.6. Each network was trained with the same input data. This consisted of 9 discrete bins of the number of photons detected by each of the PMTs resulting in 54 input neurons for the six PMTs, feeding into 3 layers of neurons with a sigmoid activation function.

The networks trained with an upper energy cut off of 1 MeV, were trained with 196 facts (7 monoenergetic neutron sources, ranging from 15 keV to 1 MeV located at 28 locations around the spherical scintillator). The networks trained with an upper energy cut off of 5 MeV, were trained with 336 facts (12 monoenergetic neutron sources, ranging from 15 keV to 5 MeV located at 28 locations around the spherical scintillator). The resilient propagation (RPROP) training algorithm was used for each network [106].

All data used in the network were normalised between 0 and 1. The spherical angle $\phi$ was normalised over the range 0, $\pi$ and $\theta$ over the range 0, $2\pi$. The mean

squared error (MSE) used to evaluate network convergence is the error of these normalised values.

Previous research has shown that between 1 and 10 MeV in a 10.8 cm radius scintillator, visually, the anisotropic pattern of capture can no longer be seen [90]. By reducing the size of the scintillator further to 7.5 cm radius, the light collected from each capture will increase (from around 9% to 17%). However it is expected this reduction will further impede the detection abilities of the scintillator in the upper energy ranges. Two different scintillator radii were considered in this work, 7.5 cm and the original radius of 10.8 cm. Another consideration with the radius of the detector was the additional mass the larger detector will further impede portability of this instrument. A reduction in size from 10.8 cm to 7.5 cm reduces the mass from around 4.7 kg to 1.6 kg (not accounting for the instrumentation electronics). It was noted during the initial investigations of the 7.5 cm detector that no satisfactory results could be obtained when training the network with an upper energy limit of 5 MeV. By reducing this to 1 MeV, the network was observed to converge below the desired MSE.

Table 5.2: Configuration parameters of the six ANNs investigated in this work.

| Scintillator radius cm | ANN output | Hidden neurons | Normalised MSE cut off $10^{-4}$ | Training energy range |
|---|---|---|---|---|
| 7.5 | Energy | 50 | 6 | 10 kev - 1 MeV |
| 7.5 | Direction | 30 | 6 | 10 kev - 1 MeV |
| 10.8 | Energy | 54 | 2 | 10 keV - 5 MeV |
| 10.8 | Direction | 28 | 6 | 10 keV - 5 MeV |

Each network investigated was optimised in terms of numbers of hidden neurons. Starting with 10 hidden neurons it was observed the network convergence was above the MSE. Increments of 5 neurons were added to the network, and retraining was undertaken. More hidden neurons were added to the network until the point of convergence for the MSE error on the network was below that of the prescribed MSE training cut off. This MSE value was obtained experimentally by ensuring that the error on the training data was suitably low, but not low enough that the network over trained on the training facts and became less flexible to testing facts it had never seen before. The final configurations of the ANNs are shown in Table 5.2.

The instruments ability to work with data it has not received training for is a crucial requirement of this instrument. Once trained, each network was tested with a data set interpolating between neutron source energies and directions found in the training data. Training a network with a large number of neutron sources in a laboratory environment would be a time consuming task, so the network's abilities to interpolate between training facts should reduce the need for a large number of training facts.

## 5.5 Results

### 5.5.1 Monoenergetic neutron sources

To assess the suitability of the training of the ANNs, each network was tested with monoenergetic neutron source energies interpolating between the training energies. Four source locations were selected that were not found in the data set. In each of these cases the neutron field located at directions AP, PA, RLAT and LLAT to the detector.

For validating the training of the direction ANN, the spread of the estimated angles were plotted and this is shown in Figure 5.7a and 5.7b. Each data cluster represents a single source location and within that cluster, each data point is one of the monoenergetic neutron source energies. It can be seen from Figure 5.7a and 5.7b that for monoenergetic neutrons, both detectors can resolve the azimuthal angle $\theta$ reasonably well. However it can be seen that with the estimation of the polar angle component, $\phi$ there is a spread of around 45 degrees in this estimation for the 7.5 cm detector. For the 10.8 cm this worsens to a spread of around 63 degrees.

It is thought that at energies greater than 1 MeV the isotropic pattern of capture makes it hard to resolve the direction of neutron incidence. For each energy, the network is trained with 24 different source locations. So in the range of 1-5 MeV the network is potentially seeing around 100 facts that all appear similar to the network, in terms of input values. With noise propagated into this data it is thought that this matter will only become worse.

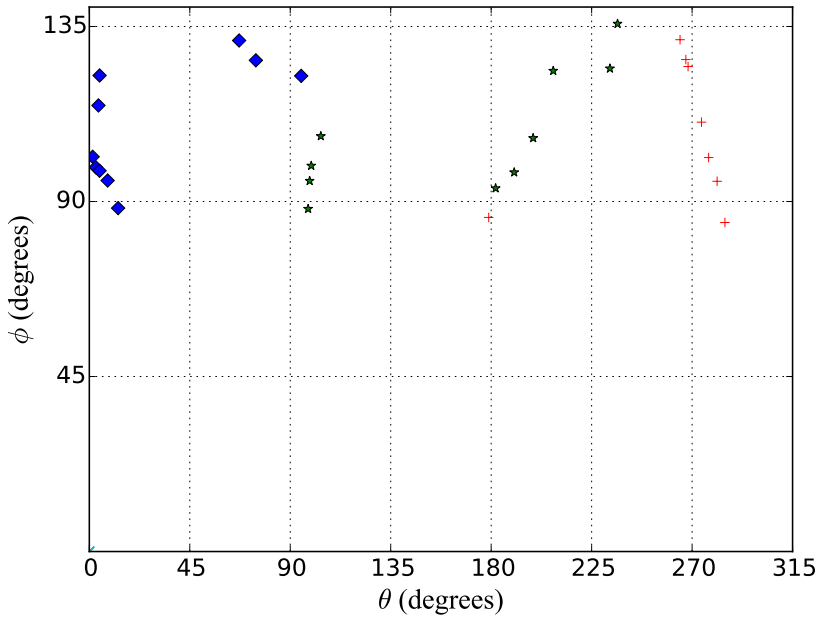


(a)

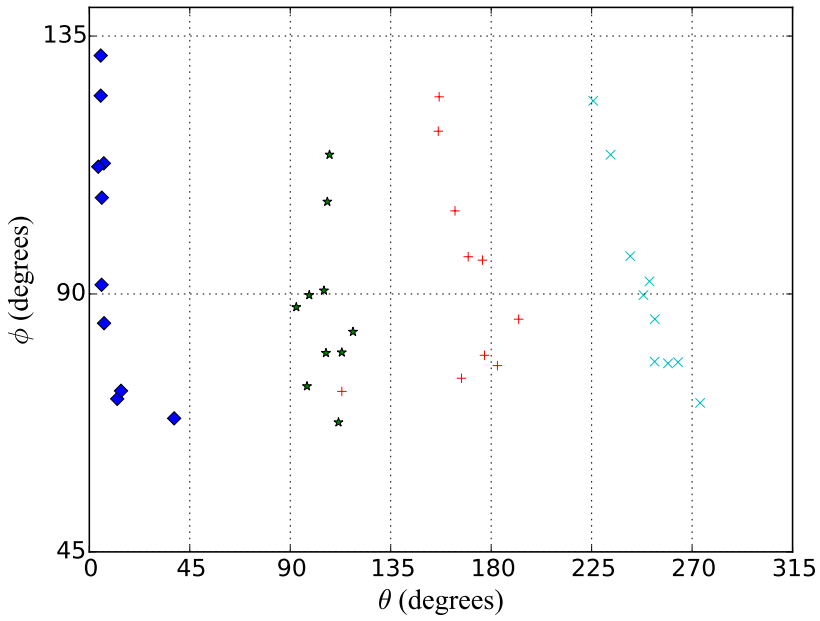


(b)

Figure 5.7: ANN estimation of the incidence of a monoenergetic neutron field for four different source locations (AP (0°), PA (180°), RLAT (90°) and LLAT (270°)) for (a) 7.5 cm detector and (b) 10.8 cm detector.

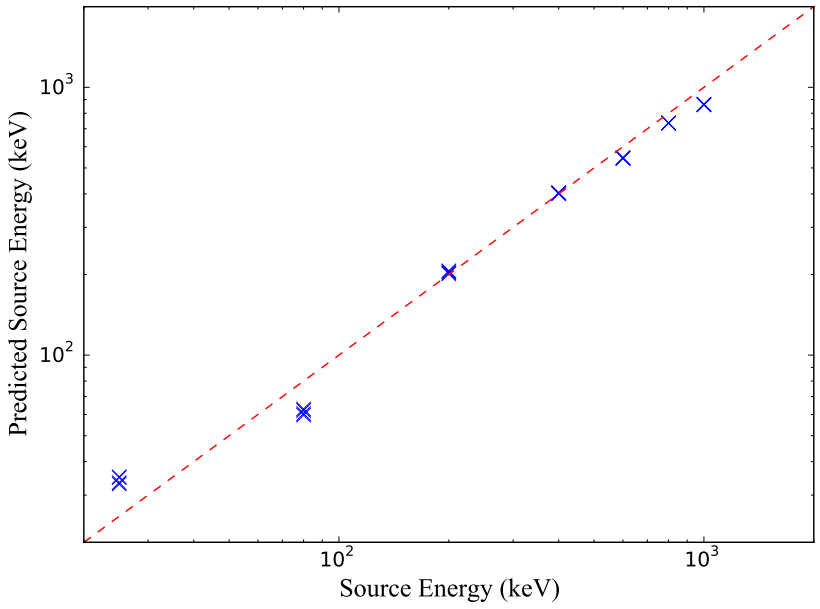


(a)

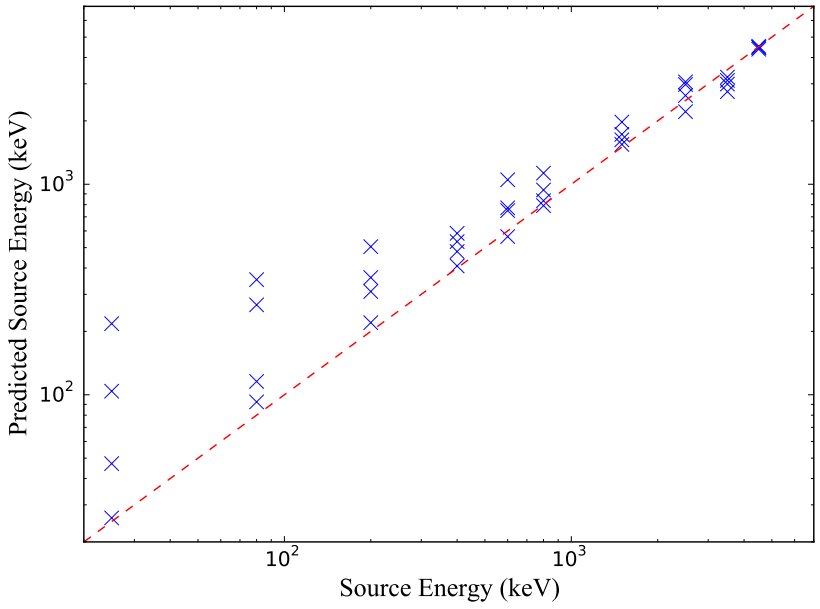


(b)

Figure 5.8: ANN estimation of the energy of a monoenergetic neutron field compared against the known energy of this field. Each energy was repeated for four different source locations (AP, PA, RLAT and LLAT) with the two detectors of radius (a) 7.5 cm and (b) 10.8 cm.

To investigate the validity of the ANN estimating energy, each the ANN estimation energy was plotted against the known value of each monoenergetic neutron source energy. This can be seen in Figure 5.8a and 5.8b, with four points in each data cluster representing each source location. It can be seen that the 7.5 cm detector is able to estimate the energy much better than the 10.8 cm detector at lower neutron energies.

### 5.5.2 Testing the ANN with a distributed neutron field

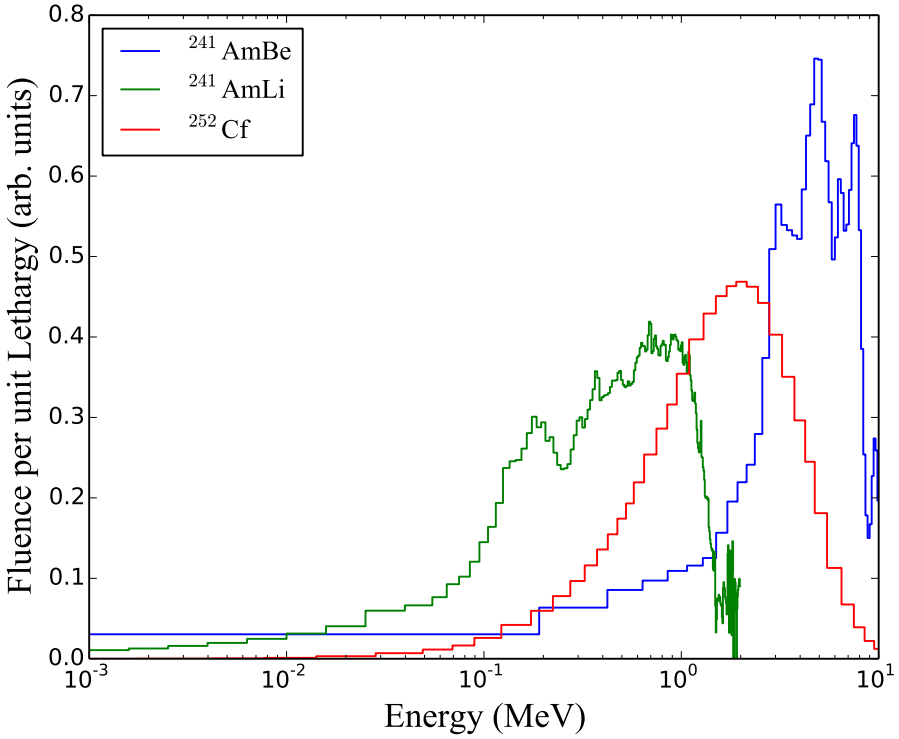


Figure 5.9: The neutron spectra of three distributed fields used for testing the ANN in this work; $^{252}$Cf, $^{241}$AmBe and $^{241}$AmLi.

With the promising results obtained modelling monoenergetic neutron sources it was decided to investigate if the ANN could estimate the effective dose of a more complex neutron fluence with energy dependency. For these investigations three radionuclide source were investigated; $^{252}$Cf, $^{241}$AmBe and $^{241}$AmLi. The neutron spectra from these three sources can be seen in Figure 5.9. Due to the higher energies

Table 5.3: ANN estimate of effective dose of 3 radionuclide neutron sources investigated in this work.

| Neutron Source | Neutron incidence | Calculated effective dose (pSv.cm$^2$) | ANN estimated effective dose (pSv.cm$^2$) | Percentage difference between calculated and estimated effective dose % |
|---|---|---|---|---|
| $^{252}$Cf | AP | 350 | 392 | 11 |
| | PA | 209 | 196 | 6 |
| | RLAT | 138 | 107 | 26 |
| | LLAT | 159 | 136 | 15 |
| $^{241}$AmBe | AP | 426 | 421 | 1 |
| | PA | 291 | 238 | 20 |
| | RLAT | 197 | 168 | 16 |
| | LLAT | 222 | 182 | 20 |
| $^{241}$AmLi | AP | 152 | 207 | 30 |
| | PA | 77 | 87 | 13 |
| | RLAT | 48 | 35 | 32 |
| | LLAT | 57 | 43 | 28 |

found within these fields, only the 10.8 cm detector trained up to 5 MeV was used. The neutron energies found within these spectra are both above and below those used in the training data. The source was located AP, PA, RLAT and LLAT to the detector. No further training was undertaken with the networks from those used for monoenergetic tests.

The results shown in Table 5.3 show promising results of the estimation of the effective dose from these distributed fields. The maximum difference between calculated and effective dose was found to be 30%. With the $^{241}$AmBe source it can be seen in Figure 5.9 there is a contributing fluence of neutrons above the upper ANN monoenergetic training energy of 5 MeV. With neutrons above those found in the training energies contributing to the spectra it the ANN is able to estimate this effective dose to within 20%. The broader distribution of the $^{241}$AmLi can be seen to estimate the dose with a slightly larger percentage difference compared to the $^{252}$Cf and $^{241}$AmBe results. It is thought that the lower energies found within this spectra could be causing this higher percentage difference as it can be seen in Figure 5.8b that ANN is not able to estimate these lower energies as accurately.

## 5.6 Conclusion

In this work it has been investigated using Monte Carlo simulations if the effective dose of a neutron field could be estimated based upon the pulse height spectra from a number of neutron captures in a scintillator. The results obtained showed promise. Each ANN was optimised with extensive training and these optimal networks were then validated with data that the ANN had not seen during training. This consisted of monoenergetic neutron source energies interpolating between the training energies and different source locations. The network was able to resolve the azimuthal angle of incidence reasonably well. However the polar angle of incidence was found to have a large spread. It is not known how much this would affect the effective dose as with the current ICRP fluence to effective dose conversion coefficients no values are published to account for these polar angles. Further investigation will be required to quantify this.

Following initially promising results with the monoenergetic neutron fields, the networks were then tested with three neutron sources. These sources were located AP, PA, RLAT, LLAT, locations not found in the training data. The ANN was able to estimate the effective dose with an accuracy of 30% or less.

Reducing the detector size to 7.5 cm radius, an upper limit of 1 MeV is imposed. However with the larger radius detector less light will be collected from each neutron capture event. This will likely impede the abilities of the detector to discriminate a scintillation as a neutron capture. This capture detection ability is crucial for the instrument. For use of the instrument in the upper energy ranges it is thought that a polyethylene moderator could be installed around the detector. Whilst adding mass to the instrument this would potentially enable a energy and direction of the field to be resolved at energies above 1 MeV. This would not reduce on the amount of light collected by each neutron capture, and thus not impede the ability to perform PSD on the detected light pulses.

To realise this instrument into one which can be used to estimate the effective dose of a broader distributed workplace fields further investigation is required. Specifically, to see if the ANN can cope with multiple angles of incidence and broad energy distributions with stronger thermal components. It is anticipated that the proton recoil distribution could be investigated to aid the ANN in these more broad

energy spectra. For complex fields with multiple incidence it needs to be investigated how much training the ANN would require to deal with multiple unknown angles of incidence.

# Chapter 6

# Comparative analysis of pulse shape discrimination methods in a $^{6}$Li-loaded plastic scintillator

*Balmer, M.J.I, Gamage, K.A.A and Taylor, G.C.*

*Nuclear Instruments and Methods in Physics Research Section A Accelerators, Spectrometers, Detectors and Associated Equipment. 788:146-153, July 2015*

## 6.1 Abstract

Three algorithms for discriminating between fast neutrons, thermal neutrons and gamma rays in a $^{6}$Li-loaded plastic scintillator have been compared. Following a literature review of existing pulse shape discrimination techniques, the performance of the charge comparison method, triangular filtering and frequency gradient analysis were investigated in this work. The scintillator was exposed to three different mixed gamma/neutron radiation fields. The figure of merit of neutron/gamma separation was investigated over a broad energy range, as well as for the neutron capture energy region. After optimisation, all three methods were found to perform similarly in terms of neutron/gamma separation.

## 6.2 Introduction

Scintillators loaded with a high neutron capture cross-section isotope enable detection of not only fast neutrons, but also thermal neutrons. Recently, plastic scintillators with a $^{6}$Li loading have been developed, with the ability to discriminate events between thermal neutron, fast neutron and gamma interactions [107]. When compared to low flash point loaded liquid scintillators, the advantages of easy to machine plastics are obvious.

When a neutron interacts in a scintillator, its primary method of energy loss is through elastic scattering with a proton. The recoil of this proton excites $\pi$-electrons within the molecular structure of the scintillator, raising the $\pi$-electrons from their ground state to either a singlet, $S_i$, or triplet state, $T_i$. The decay of $\pi$-electrons back to their ground state results in a prompt emission of photons, known as *fluorescence*. This *fast component* of the detected scintillation pulse typically occurs a few nanoseconds after the excitation. With the interaction of two $\pi$-electrons in the $T_i$ state it is possible to be left with one in the $S_0$ state and one in the $S_1$ state. When this $S_1$ electron decays the photon emission is known as *slow fluorescence*. This produces the *slow component* of a scintillation pulse [32].

Heavier particles exhibit a greater rate of energy loss in a scintillator, due to their higher ionising densities resulting in pulses that decay more slowly by delayed fluorescence. Hence, by examining the differences in these pulse shapes, it is possible to determine the type of interacting particle.

If a neutron loses enough energy in a scintillator through elastic collisions, it is likely it will be captured when a loading isotope is present in the scintillator. For a scintillator loaded with the high capture cross-section isotope $^{6}$Li, the capture of the neutron results in the emission of two low atomic mass particles, as shown in Equation 6.1:

$$^{1}n +^{6} Li \rightarrow t\ (2.73\ MeV) + \alpha\ (2.05\ MeV), \tag{6.1}$$

where $t$ is tritium ($^{3}$H). The interaction of a gamma in a scintillator usually results in the Compton scattering of an electron. Therefore in a mixed radiation field, with a $^{6}$Li-loaded scintillator, four main particles (proton, $\alpha$, tritium and an electron) are detected as a result of neutron scattering, neutron capture and gamma interactions

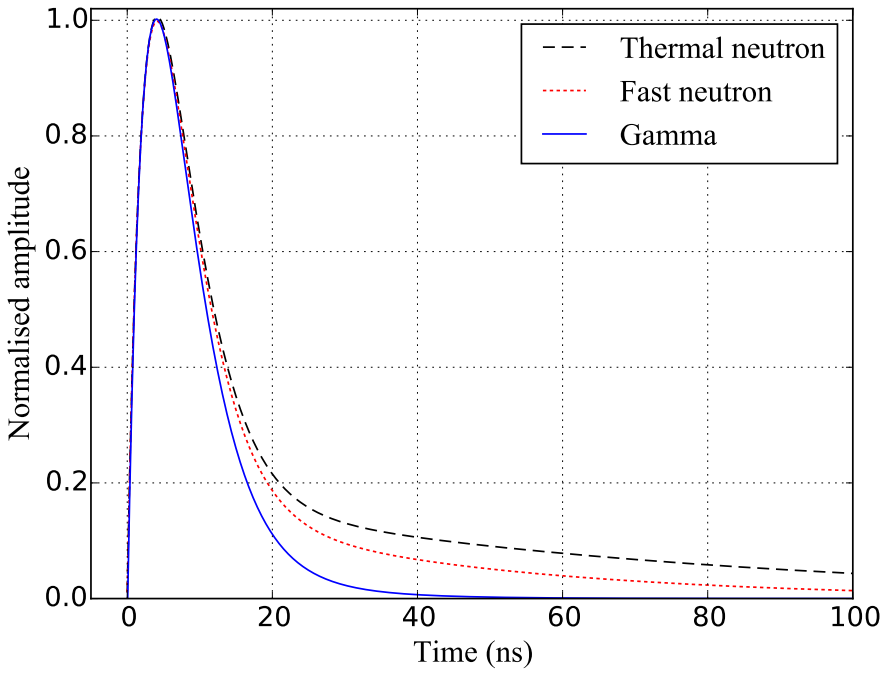


Figure 6.1: Theoretical pulse shape of a fast neutron, captured thermal neutron and gamma interaction in a scintillator. Based on information presented by Zaitseva et al. [107]

respectively. The slow component of the scintillation pulse is proportional to the ionisation density of the interaction, so inspection of the slow component allows the discrimination of three primary interactions of neutrons and gammas in a scintillator. Theoretical models of these three pulse shapes are shown in Figure 6.1.

This paper reviews prior research of pulse shape discrimination (PSD) techniques in a scintillator, including methods suitable for identification of neutron capture in a loaded scintillator. The three most promising techniques are compared using experimental methods.

## 6.3 A review of pulse shape discrimination for neutron detection in scintillators

Since the early application of PSD in liquid scintillators, the two primary methods of PSD were by zero crossing and charge comparison techniques [108, 109, 110]. However, in the last decade, with the advances in semiconductor technology, there has been an increased focus towards digital approaches to PSD methodologies [49, 50, 51, 52]. In particular advances in field-programmable gate array (FPGA) and analogue-to-digital converter (ADC) technologies now allow portable, real-time systems for neutron detection with scintillators.

### 6.3.1 Analogue techniques

The zero-crossing technique relies on external analogue circuitry to integrate, over time, the pulse detected by a photomultiplier tube (PMT). This integration is typically carried out by an RC circuit and the discrimination is based upon the time to reach a prescribed nominal voltage.

Arguably, the most commonly used PSD technique is charge integration. By integrating the pulse over two different time intervals (whole pulse (long), segment after peak (tail)) separation between particles can be observed. This simple algorithm lends itself well to implementation in the digital domain, for example removing complexity associated with analogue electronic hardware. Using recursive algorithms, both of these analogue techniques have been demonstrated as digital implementations [111].

### 6.3.2 Time domain

Pulse gradient analysis (PGA), first described by D'Mellow et al. [112], exploits the difference between the peak and a sample amplitude (after a given time) of a scintillation pulse. This method requires experimentation to find the optimum time interval between the peak and the sample amplitude. For optimum results, a finite impulse response (FIR) filter is recommended for use with this algorithm. Using a sample amplitude closer to the peak will improve pile-up capabilities as all information required to discriminate is recorded by this time.

Unknown particle interaction pulse shapes can be compared against a known set of pulse shapes in the time domain. Marrone at al. [72] presented an empirical method for comparison, this method has been compared with other PSD methods in the time domain [113]. By using a statistical technique to compare the difference between the theoretical pulse and the normalised unknown pulse, events can be classified as neutron or gamma events. Expanding further on these techniques, known for their pattern matching capabilities, artificial neural networks have been successfully deployed [52, 114, 115]. Typically time of flight (TOF) will be used to obtain a known pulse shape for a neutron/gamma interaction. However, this methodology is time consuming and would need to be repeated for any change to a system which could affect the pulse shape (cable, digitiser, amplifiers etc.). Recent investigations into pulse classification techniques highlight the possibility of foregoing TOF classification [116].

With the bulk of the signal processing performed in software, switching between PSD techniques can be used depending on the energy of the detected event [117]. A low-processing-intensive algorithm can be used for higher energies, whilst at lower energies, more computationally intensive algorithms can be used; thereby not impacting too much the overall throughput of the signal processing system.

Using triangular filtering techniques, Nakhostin demonstrated effective PSD down to 65 keVee [74]. It is worth noting that the results presented in this research were obtained using an ADC with a resolution of only 8 bits. Trapezoidal shaped filters have also been investigated [118].

### 6.3.3 Frequency domain

As previously noted FPGA technology has helped to accelerate the growth of investigation into PSD in the digital domain, due to FPGA's inherent ability to perform fast parallel processing [119]. Indeed with modern FPGA technology boasting fast digital signal processing capabilities in a low cost package, some of the recursive techniques applied in the time domain demand very little of a modern FPGA based analyser. The recent investigations of PSD in the frequency domain lend themselves well to FPGA implementation [49, 120, 121, 122]. Furthermore, frequency gradient analysis (FGA) has been shown to exhibit better noise rejection capabilities when

compared to some techniques operating in the time domain [49, 121, 122, 123].

To transform the detected pulse into the frequency domain, a frequency transform such as a Discrete Fourier Transform (DFT) or Discrete Wavelet Transform (DWT) can be used. The DFT has been favoured for PSD due to its lower computational overhead [121]. The difference between the zero frequency and the first frequency component of the Fourier transform is the mechanism which allows PSD to be realised using FGA.

## 6.4 Experimental method

The $^{6}$Li-loaded scintillator investigated in this work was provided by the Lawrence Livermore National Laboratory (LLNL), USA. The scintillator (denoted by the LLNL number 9023) had dimensions; 40 mm diameter and 25 mm thick [107].

The scintillator was coupled to an ET Enterprises 9214B PMT with Eljen EJ-550 optical grease. The scintillator was then enclosed in a light proof housing. The PMT was housed in a ET Enterprises B2F/RFI housing with a C638B tapered distribution voltage divider. The high voltage was set to -1200 V and connected to the PMT cathode. The PMT anode was connected to a Hybrid Instruments Ltd TOM digitiser system. The digitiser was configured to sample the raw pulses at a rate of 500 MS/s (2 ns per ADC sample) with an effective resolution of 11 bits. The information for each triggered pulse consisted of 128 ADC samples. The data were sent to a UDP/IP server on a personal computer for recording. These samples were processed with a custom program written in Python. A schematic diagram of the hardware is shown in Figure 6.2.

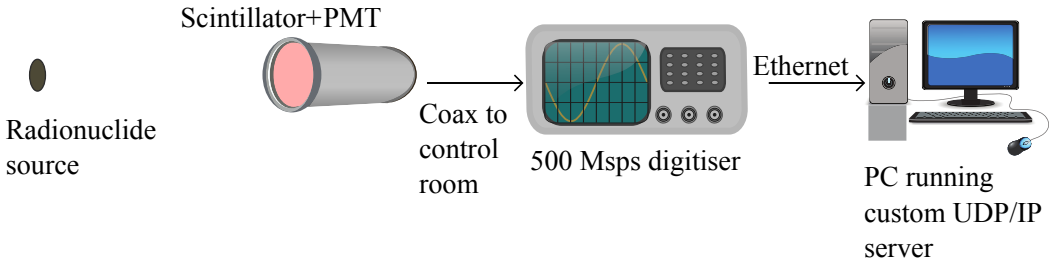


Figure 6.2: Schematic diagram of the experimental setup.

Previous research with the $^{6}$Li-loaded plastic scintillator has shown that the

thermal capture cluster lies within the elastic neutron group [107]. The first investigation in this work was the capability to discriminate fast neutrons from gamma interactions in the scintillator. Three different mixed radiation fields were considered in this work, a $^{252}$Cf (NPL reference number 4774) with a 12.7 cm diameter Bonner sphere surrounding the source, $^{241}$AmBe (NPL reference number 1095) with a Pb cap to suppress low energy (60 keV) gamma detections in the scintillator, both unmoderated and surrounded by a 20.32 cm diameter Bonner sphere. The Bonner spheres were used for two of the sources to provide a higher thermal neutron fluence within the field. The unmoderated $^{241}$AmBe field was chosen to contrast these fields with a low thermal content and higher fast neutron content. Each of the sources was located 1 m from the front face of the scintillator. The numbers of pulses recorded with each source are shown in Table 6.1.

Table 6.1: Table detailing the sources used with the two different sized scintillators in this work.

| Source | Moderation - Bonner sphere size (cm) | Number of accepted pulses |
|---|---|---|
| $^{252}$Cf | 12.7 | 117829 |
| $^{241}$AmBe | None | 54306 |
| $^{241}$AmBe | 20.32 | 70141 |

### 6.4.1 Figure of merit

The quality of separation between neutron and gamma induced pulses in the scintillator can be quantified with a figure of merit (FOM) calculation as shown in Equation 6.2:

$$FOM = \frac{m2 - m1}{FWHM_n + FWHM_\gamma}, \tag{6.2}$$

where *m2* and *m1* are the corresponding discrimination index for neutron and gamma peaks from a normal distribution fitting of the data and, FWHM is the full-width at half-maximum of each of these distributions. An example is shown in Figure 6.3.

In this work two principal energy ranges were investigated in terms of neutron/gamma separation FOM. The first was 400 keVee to 1300 keVee, the second

was 300 keVee to 400 keVee, this second region specifically focusing on the thermal neutron capture energy range. Using the mixtures function within the Python library, *scikit-learn*, normal distributions were fit to each of the peaks [124]. To check the quality of these fits a linear regression test was performed between the fit and experimental data. The lowest r-squared value observed was 0.986.

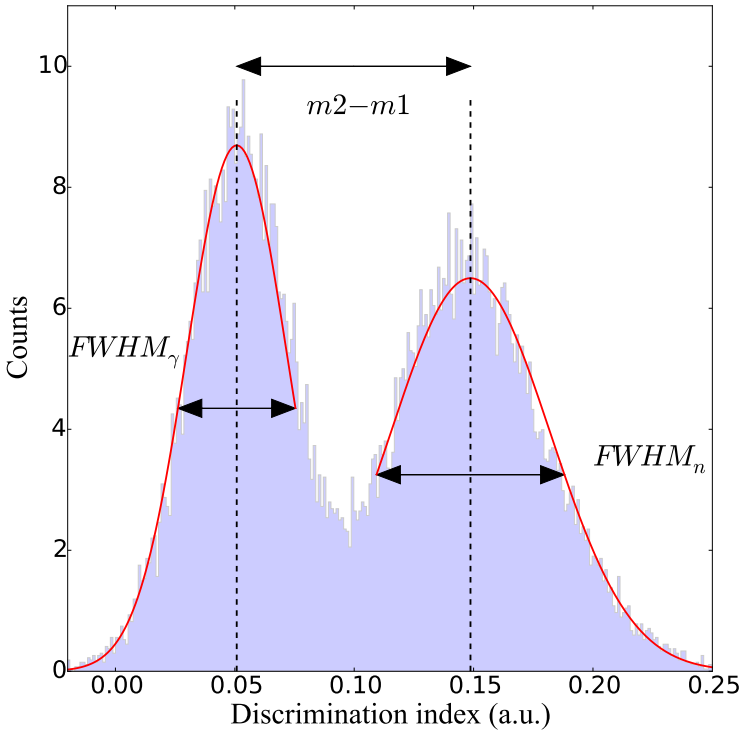


Figure 6.3: Derivation of the figure of merit (FOM) calculations carried out in this work. The full width at half maximum (FWHM) is found for both the gamma events (the left hand distribution) and neutron events (the right hand distribution). The peak separation of the two normal distributions is divided by the sum of these two FWHM values.

## 6.5 Results

### 6.5.1 Energy calibration

An energy calibration was performed on the system using two gamma sources, $^{22}$Na and $^{137}$Cs. An $^{22}$Na source produces two gamma rays of energy 511 and 1275 keV, with corresponding Compton edges of 341 and 1062 keV respectively, for gamma interactions in the scintillator. The $^{137}$Cs produces 662 keV gamma rays with a corresponding Compton edge of 477 keV for gamma interactions. The $^{22}$Na gamma source consisted of a 1 mm diameter ion exchange bead at the centre of a solid plastic disc 3 mm thick and 25 mm in diameter. The source was positioned 12 cm from the front face of the scintillator, 51061 pulses were recorded. The $^{137}$Cs source was located 1 m away from the front of the scintillator and 66436 pulses were recorded. The raw pulse height data were compiled into a histogram counting the number of occurrences of each ADC bit in the data as shown in Figure 6.4.

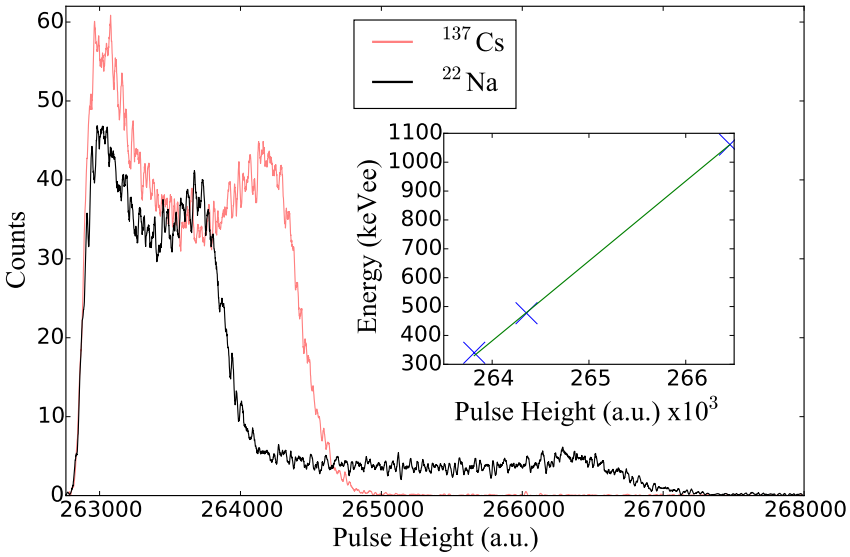


Figure 6.4: Light output from two gamma emitting sources, $^{22}$Na and $^{137}$Cs, showing three Compton edges. These Compton edges of 341, 477 and 1062 keV are then translated to a pulse height. The inset shows the linearity of the calibration line intersecting these three points.

The Compton edges were found by taking the 75% value after each of the Comp-

ton peaks [125]. These three Compton edges are plotted in the inset of Figure 6.4 and are shown to exhibit good linearity.

### 6.5.2 Raw data and filtering

To investigate the noise of the system, 100 raw pulses randomly selected from the $^{22}$Na source irradiation were normalised to unit pulse height and are shown in Figure 6.5. The blue shaded areas in Figures 6.5a and 6.5b represent the maximum and minimum values of each sample bit, respectively. From inspection of the baseline in Figure 6.5a it can be seen that below 200 keVee, relative to the peak of the pulse, the noise levels are reasonably high. As the energy increases towards the anticipated thermal capture region, between 300 and 400 keVee, Figure 6.5b shows that this noise becomes less of a problem. However it can still be seen that due to sampling every 2 ns, by taking the maximum value recorded in each pulse there is potentially up to 2 ns jitter relative to the true peak. For the 300-400 keVee energy region, the blue shaded area after the peak from 20 to 25 ns is due to this jitter rather than noise.

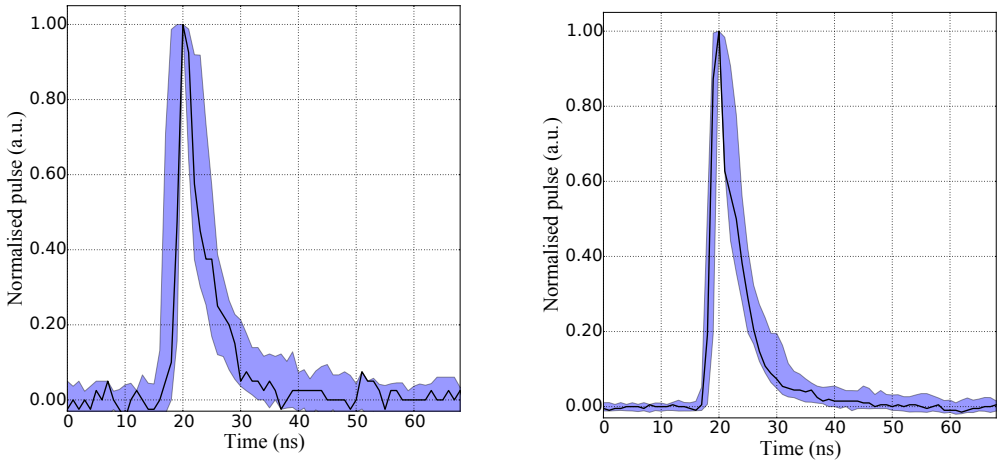


(a) (b)

Figure 6.5: Normalised raw pulse data recorded with $^{22}$Na source. The black line shows a single raw pulse. For each sample bit, a maximum and minimum value in the data was recorded. These maximum and minimum values are the upper and lower bounds of the blue shaded area respectively for (a) pulses in the 100-200 keVee range, (b) pulses in the 300-400 keVee range.

### 6.5.3 Charge comparison method (CCM)

In this work the long (entire pulse) and short (tail of the pulse) integrals of each pulse have been found by summing the ADC samples within the temporal windows of their definitions. More computationally intensive methods of numerical integration have been shown to have no benefit when applied to CCM [111]. With each of the PSD techniques investigated in this work, parameters can be changed to optimise performance. In the case of CCM the short integral length can be optimised.

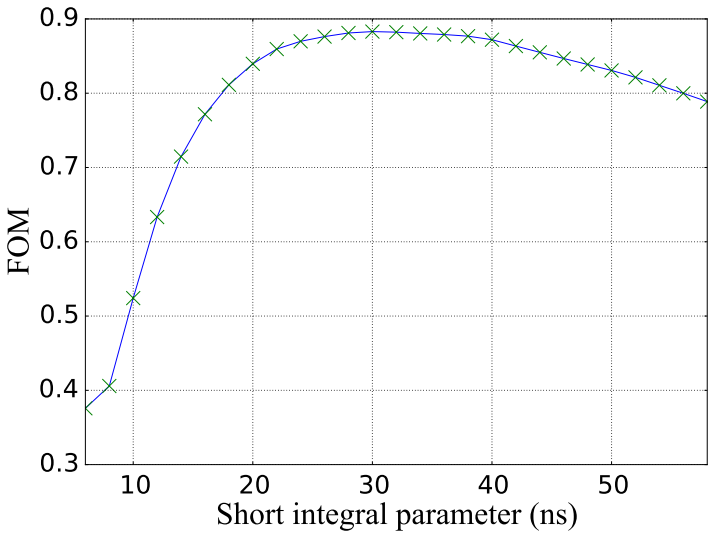


Figure 6.6: Pulse shape discrimination results from charge comparison method (CCM). By varying the short integral length and evaluating the FOM, it was found there was an optimised short integral parameter.

For a number of short integral lengths, the FOM was evaluated (using data obtained from an $^{241}$AmBe source in the 800-1300 keVee range). The optimum value after the peak of the pulse to start the short integral was found to be 30 ns. This optimisation is shown in Figure 6.6. The long integral was defined as 10 ns before the peak of the pulse to 140 ns after the peak of the pulse. Whilst these values are optimal for achieving the best figure of merit in this work, a trade off could be realised by reducing the length of the long integral to reduce pulse pile up problems. However in this work pulses have simply been rejected by a pile up algorithm. This algorithm rejected the data if two peaks occurred in a data packet (256 ns).

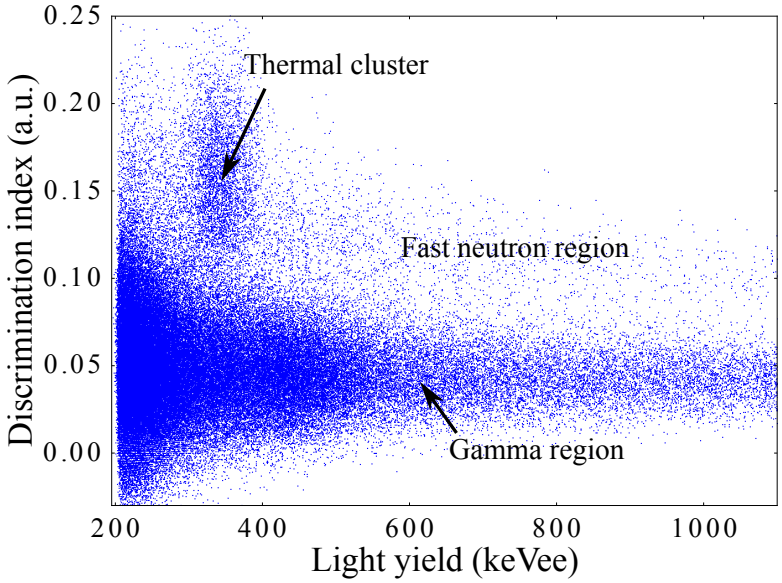


Figure 6.7: Pulse shape discrimination results from charge comparison method (CCM). Long integral divided by short integrals versus the total light output for CCM pulse shape discrimination with moderated $^{252}$Cf.

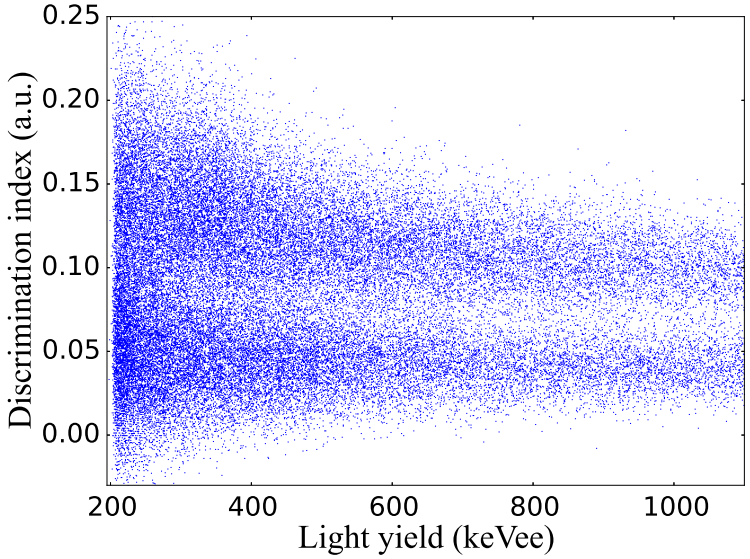


Figure 6.8: Pulse shape discrimination results from charge comparison method (CCM). Long integral divided by short integrals versus the total light output for CCM pulse shape discrimination, with sources $^{241}$AmBe.

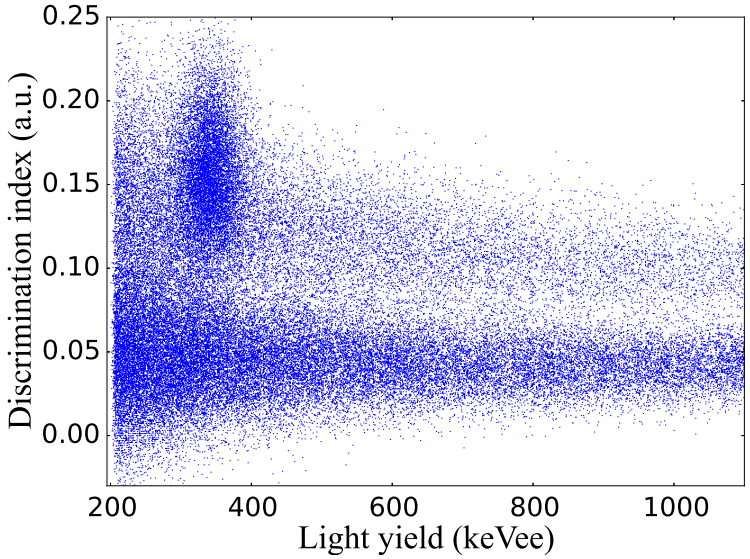


Figure 6.9: Pulse shape discrimination results from charge comparison method (CCM). Long integral divided by short integrals versus the total light output for CCM pulse shape discrimination, with moderated $^{241}$AmBe.

The performance of CCM with the $^{6}$Li-loaded scintillator can be seen in Figures 6.7 to 6.9. In each of the figures, above 300 keVee, the gammas are found between a discrimination index of around -0.05 to 0.07. Above this, in the second plume, are the fast neutrons. Within this plume at around 340 keVee the thermal neutrons are found.

A high thermal, low fast neutron field was established using a 12.7 cm Bonner sphere around a $^{252}$Cf source. The results are shown in Figure 6.7. A low number of fast neutrons were observed, compared to numbers of thermal neutron captures. A high gamma contribution to this field can be seen and at the lower end of the thermal neutron region, at around 250 keVee. It can be seen that the discrimination between thermal neutrons and gammas becomes very difficult.

With a low thermal neutron content in an $^{241}$AmBe field reasonable neutron/gamma discrimination can be observed down to around 500 keVee, as shown in Figure 6.8. Below this energy, the uncertainty of an event being a neutron or gamma will be high.

### 6.5.4 Triangular filtering algorithm (TFA)

In this method a triangular filter is employed on the pulse and the difference in amplitude in output of the filter is used to discriminate between neutron and gamma events [74]. This discrimination takes place on a modified pulse consisting of only samples after the pulse peak, where each sample in this region is subtracted from the peak amplitude of the pulse. The recursive triangular filter formula shown in Equation 6.3:

$$z[n] = z[n-1] + y[n] - 2y[n-k] + y[n-2k], \tag{6.3}$$

where $z$ is the filtered pulse, $y$ is the modified pulse (pulse from peak onwards), $n$ is the current sample bit and $k$ is an integer for the time constant of the filter. It should be noted that these pulses were also processed by additional filtering before being passed to the triangular filter. Savitzky-Golay, moving average and FIR filtering were investigated [126]. The highest FOM was observed with a 31 sample point moving average filter. With this optimised moving average filter, $k$ was then varied to investigate the dependence of $k$ on the FOM, and this optimisation is shown in Figure 6.10. The peak value of the moving average filter was divided by the peak value of the triangular filter to find the discrimination index.

The parameter $k$ selected for the results presented in this work was found by inspecting the FOM of the data obtained from an $^{241}$AmBe source, specifically with data in the 800-1300 keVee range. A value of 67 was chosen for $k$. The results of the PSD performance can be seen in Figures 6.11 to 6.13. It can be seen that very similar results to CCM were obtained.

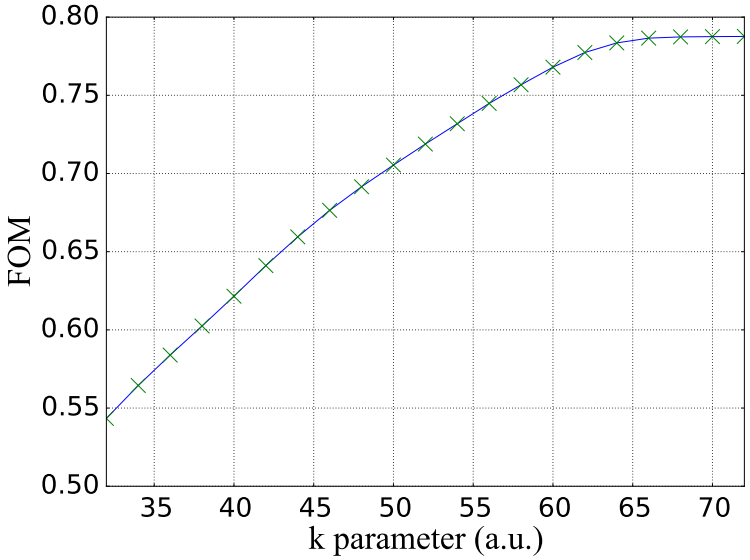


Figure 6.10: Pulse shape discrimination results from triangular filtering algorithm (TFA). The optimisation of filter parameter k was performed by inspecting the resulting FOM for each value investigated.

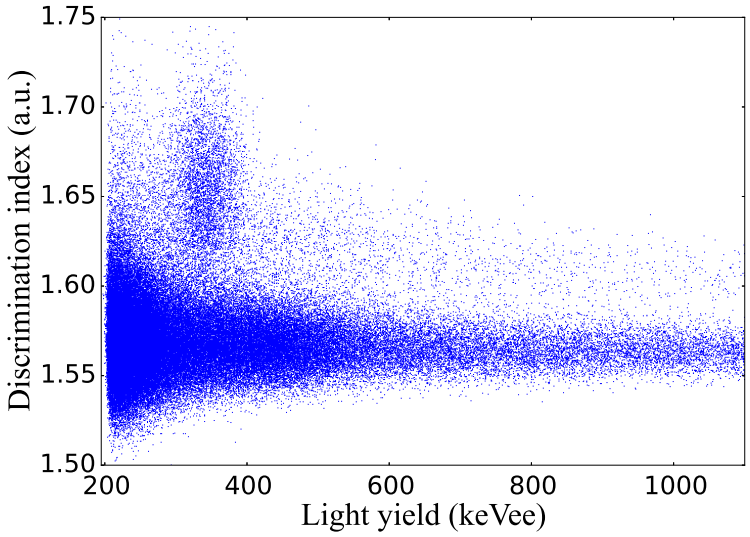


Figure 6.11: Pulse shape discrimination results from triangular filtering algorithm (TFA). Normalised triangular filter output versus the total light output, with moderated $^{252}$Cf.

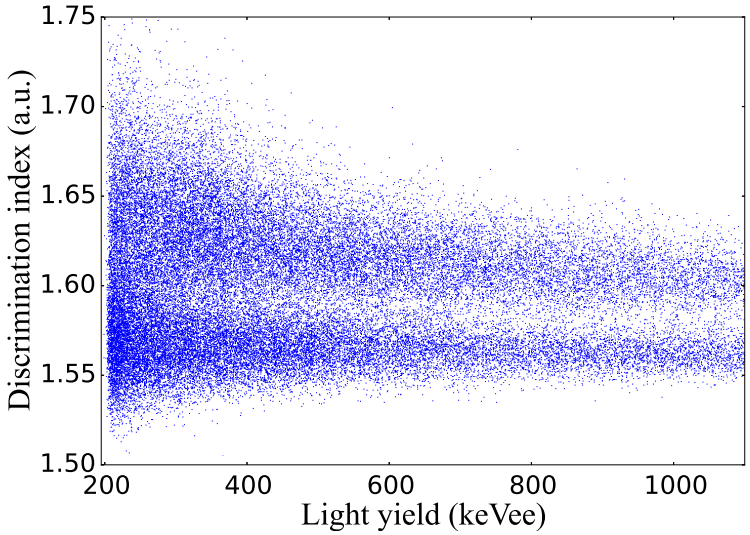


Figure 6.12: Pulse shape discrimination results from triangular filtering algorithm (TFA). Normalised triangular filter output versus the total light output, with $^{241}$AmBe.

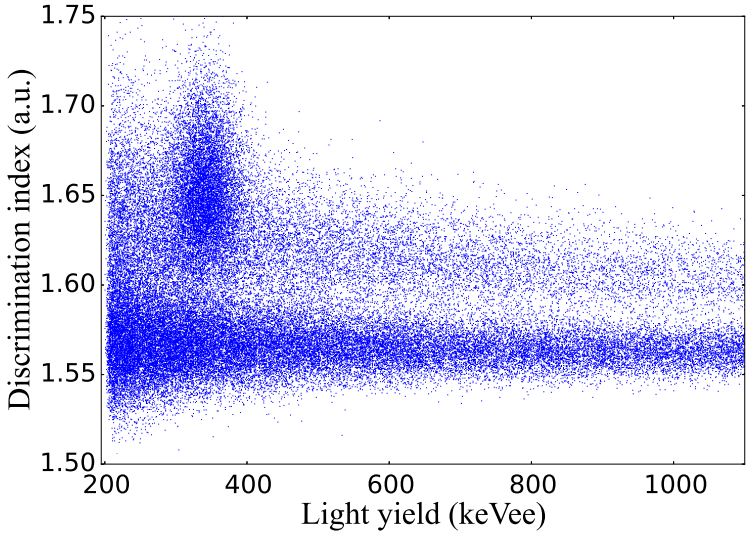


Figure 6.13: Pulse shape discrimination results from triangular filtering algorithm (TFA). Normalised triangular filter output versus the total light output, with moderated $^{241}$AmBe.

### 6.5.5 Frequency gradient analysis (FGA)

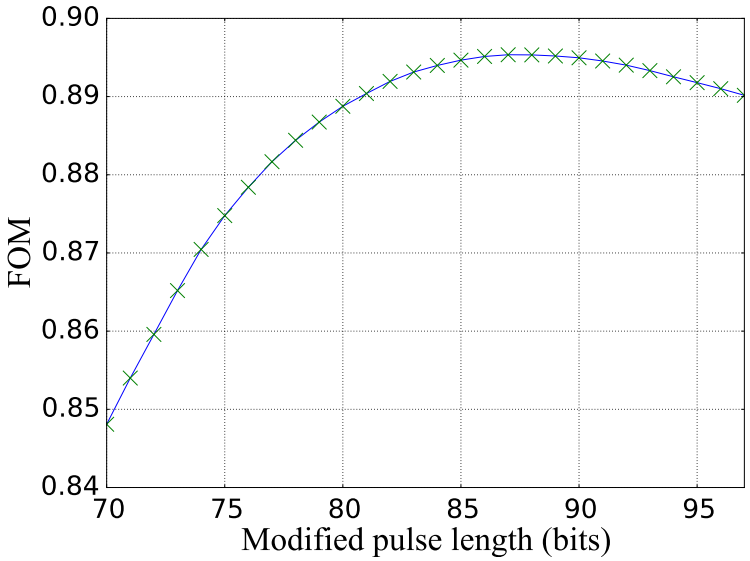


Figure 6.14: Pulse shape discrimination results from frequency gradient analysis (FGA). The optimised length to sample after the peak was found in investigating a number of different lengths and inspecting the resulting FOM.

Frequency gradient analysis is achieved by performing a Fast Fourier Transform (FFT) on the pulse [127]. Lui et al. have performed further optimisation of this technique involving the use of a moving average filter and an optimised discrimination parameter [128]. This optimised parameter is shown in Equation 6.4:

$$D_{fft} = 1 - \frac{|X[0]|}{|X[1]|} \tag{6.4}$$

where X[0] and X[1] are the first and second components of the FFT respectively.

In the empirical optimisation of the FGA method the baseline was removed from the pulse. This baseline was found by taking the average amplitude of the pulse in the range, *n-40* to *n-10*, where $n$ is the ADC sample containing the pulse peak. Previous literature has discussed the use of a moving average filter with the FGA algorithm [128]. In this instance, it was found that optimal results were achieved without the use of a moving average filter. Furthermore, modifying the pulse to only consist of 10 ns before the peak and number of samples after the peak was found to

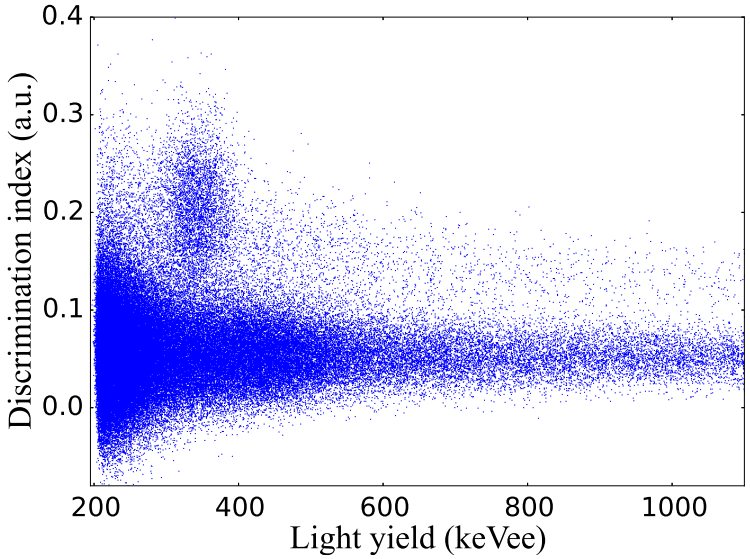


Figure 6.15: Pulse shape discrimination results from frequency gradient analysis (FGA). Gradient between first and second components of FFT of the pulse versus the total light output for FGA pulse shape discrimination, with moderated $^{252}$Cf.

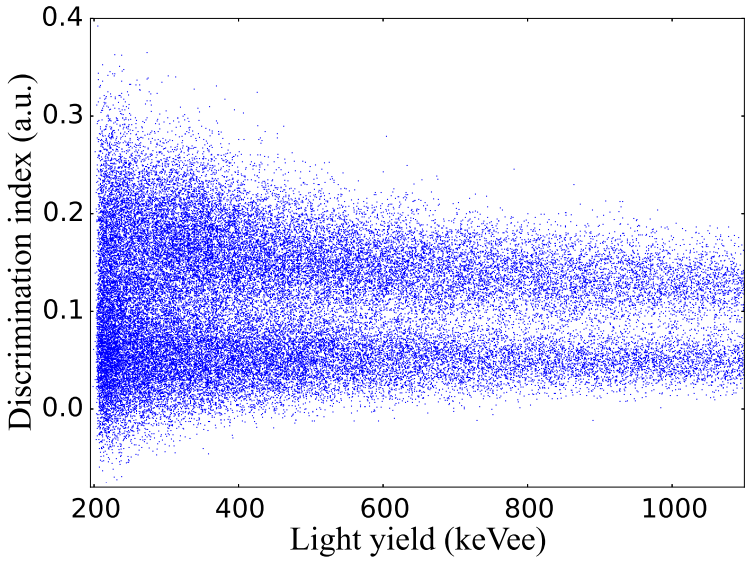


Figure 6.16: Pulse shape discrimination results from frequency gradient analysis (FGA). Gradient between first and second components of FFT of the pulse versus the total light output for FGA pulse shape discrimination, with $^{241}$AmBe.

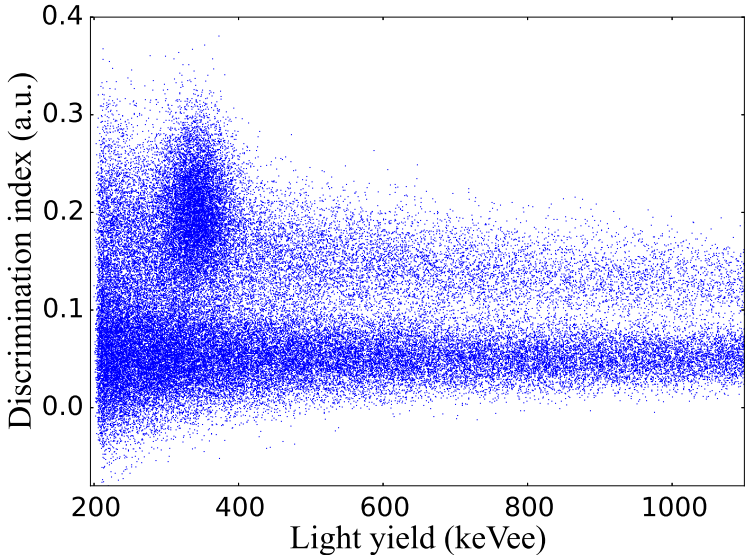


Figure 6.17: Pulse shape discrimination results from frequency gradient analysis (FGA). Gradient between first and second components of FFT of the pulse versus the total light output for FGA pulse shape discrimination, with moderated $^{241}$AmBe.

bring further optimisation. The number of samples after the peak was incremented by 1 sample bit (2 ns), starting at 70 and increasing to 97. For each increment the resulting FOM was observed. A value of 87 sample bits (174 ns) in the long segment of data after the pulse peak was chosen based on an observed maximal FOM at this value (1 sample bit either side of this would likely give the same performance). These results are shown in Figure 6.14.

The results of the PSD performance can be seen in Figures 6.15 to 6.17

The FOM for the data can be seen in Table 6.2. For both fast only and thermal regions, it can be seen that with an unmoderated $^{241}$AmBe field, for detection of fast neutrons in the 400-1300 keVee region (as well as the thermal neutron region of 300-400 keVee), FGA and CCM perform slightly better than TFA in terms of discriminating between neutron and gamma events. This trend was observed for $^{241}$AmBe, $^{241}$AmBe with a 20.32 cm Bonner sphere and $^{252}$Cf with a 12.7 cm Bonner sphere.

Table 6.2: Figure of merit (FOM) for data presented in this work for CCM, FGA and TFA methods.

| Energy Region | Source | Moderation | PSD Method | FOM |
|---|---|---|---|---|
| 400-1300 | $^{241}$AmBe | None | CCM | 0.761 |
| | | | FGA | 0.766 |
| | | | TFA | 0.746 |
| 300-400 | $^{241}$AmBe | None | CCM | 0.660 |
| | | | FGA | 0.653 |
| | | | TFA | 0.625 |
| 300-400 | $^{241}$AmBe | 20.32 cm Bonner sphere | CCM | 0.790 |
| | | | FGA | 0.773 |
| | | | TFA | 0.765 |
| 300-400 | $^{252}$Cf | 12.7 cm Bonner sphere | CCM | 0.723 |
| | | | FGA | 0.694 |
| | | | TFA | 0.634 |

## 6.6 Conclusion

Using a $^{6}$Li-loaded plastic scintillator, three pulse shape discrimination methods were investigated: FGA, TFA and CCM, with the primary aim of separating fast neutron and gamma events. Mixed radiation fields with thermal neutron content were also considered, and the ability of the three algorithms to discriminate these thermal events from gammas in the $^{6}$Li-loaded plastic scintillator was also investigated.

To describe the separation between neutron (fast and thermal) and gamma events, the quality of separation was quantified using a FOM. Two different energy regions were investigated in terms of FOM, 400-1300 keVee (fast neutron region) and 300 - 400 keVee (thermal neutron region). Although all three methods qualitatively perform very similarly, numerical analysis of the FOM showed that CCM was marginally better than FGA, where FGA was better than TFA in neutron/gamma separation in a $^{6}$Li-loaded plastic scintillator.

The optimisations for FGA and TFA found in this work are relevant for a 500 MS/s, 11 bit digitiser, where previous experimental work with these algorithms was performed with lower resolution, faster sampling rate digitisers. Recent research has investigated differing sampling rates and resolutions [54, 53]. Expanding on this work, repeating the methodology outlined in this paper for sample rates between 500

MS/s and 4 Gsps and differing resolutions would further improve the understanding of the relative performance of the algorithms discussed in this work. Recent research has also compared different pulse shaping algorithms [75]. Optimum filters for each PSD technique could also be further investigated with differing ADC sample rates and resolutions.

When comparing CCM and FGA it could be argued that although similar performance was observed between the two in terms of both fast and thermal neutron discrimination from gammas, the simplicity of CCM could be advantageous. However, with FPGA technology the number logic cells available is ever increasing. Thus the need for comparison of simplicity/processing time between PSD techniques becomes less of a salient point.

## 6.7 Acknowledgments

The authors would like to express thanks to Natalia Zaitseva and the team at LLNL for providing the scintillator sample. The authors would like to acknowledge the funding support from EPSRC and the National Physical Laboratory, Teddington, UK. We also acknowledge the help and advice of Dr. Nigel Hawkes at National Physical Laboratory. The authors acknowledge the use of the package Matplotlib for all plots in this research [129].

# Chapter 7

# Neutron assay in mixed radiation fields with a $^{6}$Li-loaded plastic scintillator

*Balmer, M.J.I, Gamage, K.A.A and Taylor, G.C.*

*Journal of Instrumentation. 10(08):P08012-1-14, August 2015*

## 7.1 Abstract

A novel technique for assay of thermal and fast neutrons in a $^{6}$Li-loaded plastic scintillator is presented. Existing capture-gated thermal neutron detection techniques were evaluated with the $^{6}$Li-loaded plastic scintillator studied in this work. Using simulations and experimental work, shortcomings in its performance were highlighted. As a result, it was proposed that by separating the combined fast and thermal neutron events from gamma events, using established pulse shape discrimination techniques, the thermal neutron events could then be assayed. Experiments were conducted at the National Physical Laboratory, Teddington, performing neutron assays with seven different neutron fields using the proposed technique. For each field, thermal and fast neutron content was estimated and were shown to corroborate with the seven synthesised fields.

## 7.2 Introduction

It is highly desirable to detect both fast and thermal neutrons, in order to perform accurate neutron dosimetry in an energy distributed field. Using a liquid scintillator with current state-of-the-art pulse shape discrimination techniques (PSD), neutron interactions in the detector can be discriminated from gamma interactions down to around 40 keVee [130]. This equates to a neutron energy of approximately 450 keV, although this is dependent on a number of factors including detector dimensions and type of scintillant [131].

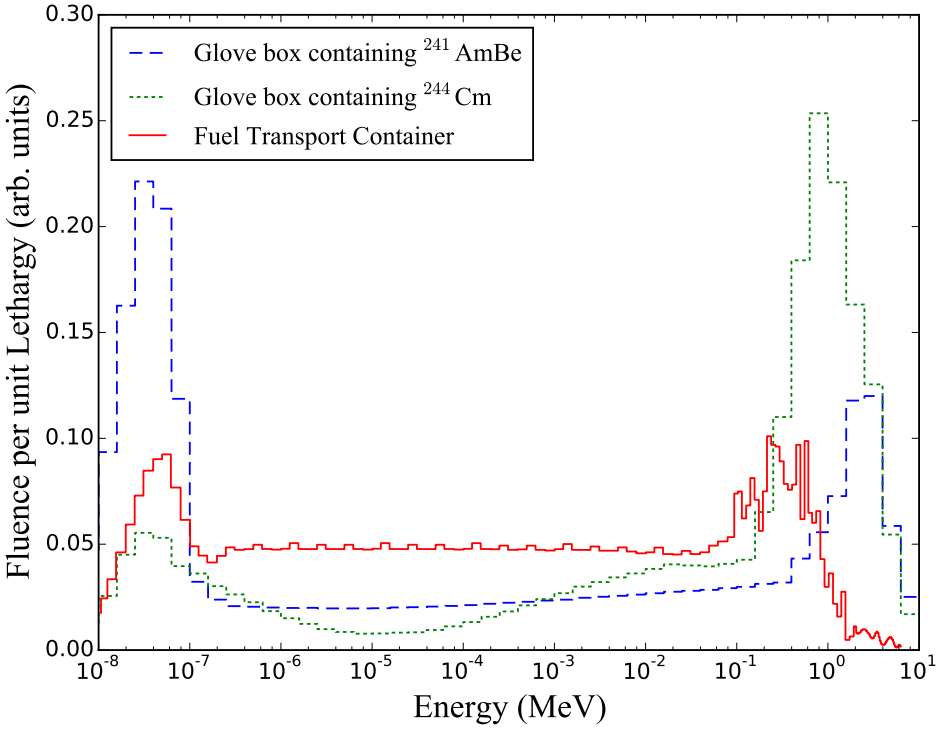


Figure 7.1: Three typical energy-distributed neutron workplace fields [132, 133]. The importance of detecting both thermal and fast neutrons to allow accurate neutron dosimetry of this field can seen.

Figure 7.1 shows three neutron spectra of different workplace fields. It can be seen that at energies below 450 keV there there is a neutron fluence which must be accounted for. Not being able to detect neutron fluences at these lower energies

would likely lead to an inaccurate estimate of the dose of these fields (despite the conversion coefficients being substantially lower below 450 keV than above 450 keV). Therefore, it is of great importance for accurate neutron dosimetry, to be able to quantify the contents of this region by determining the thermal content within the field.

Traditionally, $^{3}$He based detectors have been used for thermal neutron detection. However, dwindling $^{3}$He stocks mean that there is an ever present need to identify alternatives for these detectors [17]. A scintillator loaded with a high neutron capture cross-section isotope such as $^{10}$B, $^{6}$Li or gadolinium allows the extension of neutron detection below the 450 keV limit imposed by a typical non-loaded liquid organic scintillator, whilst still being able to detect fast neutron interactions. With a high neutron capture cross-section, $^{10}$B-loaded scintillators have been extensively used for thermal neutron detection [51, 134, 50, 135, 136, 86]. These scintillators are typically loaded with up to 5% fractional mass of $^{10}$B. The $^{10}$B capture reaction for 6% branching ratio and 94% branching ratio are shown in Equation 7.1 and Equation 7.2 respectively.

$$^{1}n + \ ^{10}B \rightarrow \ ^{7}Li + ^{4}He \ (Q - value = 2.79MeV) \tag{7.1}$$

$$^{1}n + \ ^{10}B \rightarrow \ ^{7}Li + ^{4}He + \gamma \ (0.477 \ MeV)(Q - value = 2.31MeV) \tag{7.2}$$

Although Equation 7.1 shows a high energy $^{4}$He, emitted as a result of capture, in practice it has been observed that a strong quenching of the scintillation event leads to a detected pulse of around 60 keVee with the commercially available BC-523A [86]. Further developments of $^{10}$B-loaded liquid scintillators have increased this to 100 keVee with the scintillator EJ-309B5 [94]. The 60 keVee neutron capture signal lies beneath the region of efficient pulse shape discrimination for most liquid scinitillators. As such, a capture gating technique is used to discriminate the neutron capture pulses from gamma or fast neutron interactions [51, 136]. Capture gating relies on detecting both the recoil and capture of a single neutron within the scintillator. When the detector is triggered, a time window is applied, during which time detection of two events leads to the assumption of a possible neutron capture.

To achieve a high efficiency with capture gated detection, a number of considerations must be given. The volume of the detector must be sufficiently large to allow multiple neutron interactions in the scintillator before capture, so that the resulting pulse is of a detectable amplitude. The trigger threshold for the neutron recoil pulse must also be considered. A low trigger threshold not only increases the processing demands on the electronics system (due to more frequent triggering), but also increases the probability of detecting an unwanted *accidental*, i.e. a gamma interaction. A significant potential advantage of capture gated detection is that neutron capture detection could be possible without any pulse shape discrimination or pulse height information. By simply detecting two pulses within a given coincidence window, no analysis of the shape or amplitude of the pulses would be required. This could lead to a significant simplification of the pulse processing system for a portable application.

Recent advances in plastic scintillators with a $^{6}$Li loading hold promise for thermal and fast neutron spectroscopy applications. These plastics have the potential ability to discriminate between thermal neutron, fast neutron and gamma interactions [107]. Clearly separated away from gamma interactions in a typical PSD scatter plot, the thermal cluster can be as high as 470 keVee depending on the size and synthesis of materials used. The potential hazards of low-flashpoint liquid scintillators are not a problem with plastic scintillators and they become an attractive prospect for neutron dosimetry in mixed radiation fields. The $^{6}$Li capture reaction is shown in Equation 7.3.

$$^{1}n +^{6} Li \rightarrow {}^{3}H\ (2.73\ MeV) +^{4} He\ (2.05\ MeV) \tag{7.3}$$

Comparing the isotopes of $^{6}$Li (natural abundance approximately 8%) and $^{10}$B (natural abundance approximately 20%), the later has a higher thermal capture cross-section of 3837 barns compared to 940 barns with the former. Furthermore, when considering existing scintillators, $^{10}$B-loaded liquid scintillators typically have 5% fractional mass loading of $^{10}$B, compared to 0.1-0.3% of $^{6}$Li-loaded plastic scintillators (developments to achieve higher loadings of $^{6}$Li are ongoing [107]). Therefore, it is not known currently if capture gated neutron detection with a $^{6}$Li-loaded plastic scintillator boasts any degree of thermal neutron detection efficiency.

This research investigates the suitability of capture gated detection of thermal neutrons in a $^{6}$Li-loaded plastic scintillator. The thermal cluster as a result of neutron capture in a $^{6}$Li scintillator lies within the fast neutron region. A novel technique is presented to perform thermal neutron assay based on removing the fast neutron background from this thermal neutron region.

## 7.3 Modelling neutron recoil distributions

A scintillator loaded with 0.14% fractional mass of $^{6}$Li, measuring 40 mm diameter and 25 mm thickness, was considered in this work. This scintillator, plus a second with the same dimensions with 5% $^{10}$B were modelled in a neutron field from a $^{241}$AmBe radionuclide source to understand the mechanisms of capture gated detection within each of these scintillators.

The Monte Carlo radiation transport package, MCNP v5.0, was used to simulate the detectors [88]. In MCNP materials were simulated using the ENDF/B-VII.0 neutron cross-section tables at temperature 293.13 K. To handle low energy thermal scattering of neutrons below 5 eV, MCNP has thermal treatment for a variety of material types. For s($\alpha$, $\beta$) thermal treatment, *poly.01t* was included in the MCNP input file. Using the particle tracking file (PTRAC), neutron recoil and neutron capture events within the scintillator were recorded. If an event resulted in a neutron capture, the energy deposited in the scintillator was recorded. The time between the recoil and capture was also recorded.

The simulations were terminated after 4.4x10$^{6}$ events that resulted in one or more proton recoils in the scintillator in each event. 119956 neutrons were captured in the $^{10}$B scintillator and 13789 in the $^{6}$Li-loaded scintillator. The differences in capture efficiency are reflected Figure 7.2a, showing a histogram of the energy deposited in the scintillator by each event before capture. Figure 7.2b shows a histogram of time between last recoil and capture. It can be seen that with the $^{10}$B-loaded scintillator all neutrons were captured within 1 $\mu$s. This is in contrast to the $^{6}$Li-loaded scintillator where the time to capture extends up to 6 $\mu$s. These results highlight that, as would be expected, with a significantly lower neutron capture cross-section and fractional mass content, the $^{6}$Li-loaded scintillator has a much lower capture detection efficiency.

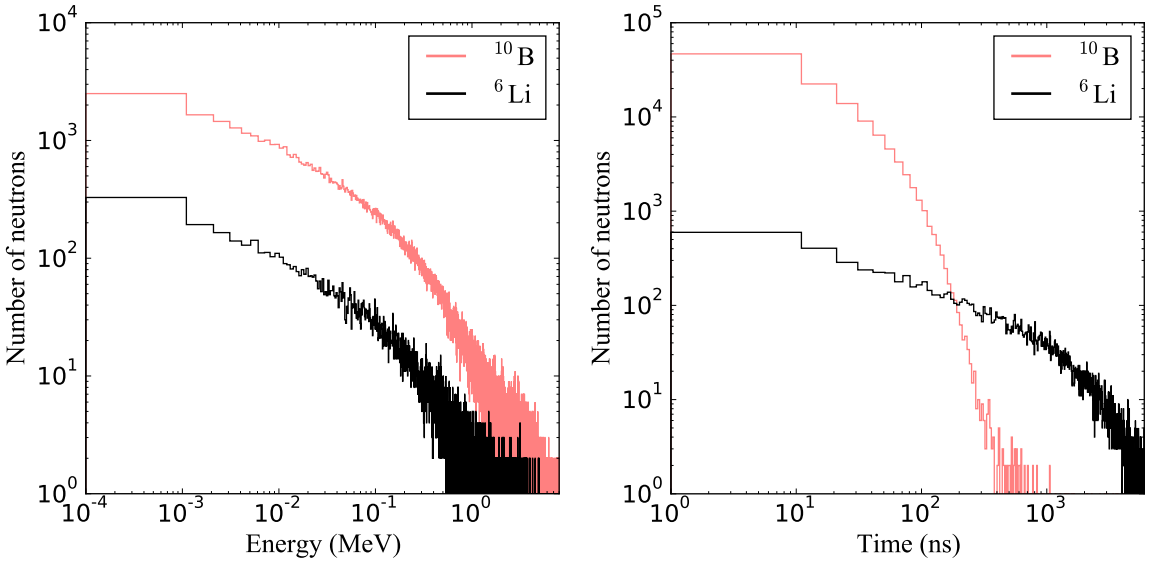


(a) (b)

Figure 7.2: Simulated results of two different loading isotopes ($^{6}$Li and $^{10}$B) in a scintillator. The Figures show (a) a histogram of neutron energy deposited in the scintillator from an event resulting in neutron capture (b) a histogram of time between fast neutron interaction and capture of this neutron for a number of events.

These simulations highlight a number of practical issues which must be considered with capture gating [137]. Due to their inherent properties, with any processing electronics and photomultiplier tube (PMT), a dead time will usually be imposed. Therefore, the pulse processing hardware and algorithms must capable of processing two pulses in quick succession. Figure 7.2b shows that for both $^{10}$B and $^{6}$Li, a high number of neutron captures occur less than 100 ns after a neutron recoil event. Also of consideration, it can be seen in Figure 7.2a a high number of recoils deposit less than 200 keV in the scintillator. Performing pulse shape discrimination on a detected signal with such low energy would be highly improbable. Therefore all gated events would need to be considered by the detection system. Furthermore, in a radiation field with a high gamma to neutron ratio, false triggering of the detection system from a gamma interaction would need to be considered. The higher the trigger is set, the lower the neutron capture detection efficiency. However, the lower this trigger is set, the system must be able to cope with this high throughput demand.

## 7.4 Methodology

### 7.4.1 Experimental details

Two $^{6}$Li-loaded scintillators were investigated in this experimental work. Both samples were provided by Lawrence Livermore National Laboratory (LLNL), USA [107]. Sample one, (denoted by the LLNL number 9023) measured 40 mm diameter and 25 mm thick. The second sample measured 25 mm in diameter by 18 mm thick, (denoted by the LLNL number 9038).

The scintillator was coupled to an ET Enterprises 9214B PMT with Eljen EJ-550 optical grease. It was then enclosed in a light proof housing. The PMT was housed in an ET Enterprises B2F/RFI housing with a C638B tapered distribution voltage divider. The high voltage was set to -1200 V and connected to the PMT cathode. The PMT anode was connected to an Analog Devices AD9254 150 MS/s, 14 bit analogue-to-digital converter (ADC). Each digitised ADC sample was clocked to an Altera Cyclone IV EP4CE115 field-programmable gate array (FPGA).

Within the FPGA, when the sampled ADC value passed over a set threshold, a 'first in first out' (FIFO) buffer was enabled. This sample and the subsequent 27 samples after this trigger, as well as one sample before the trigger, were clocked through the FIFO. When the FIFO was full, a universal asynchronous receiver/-transmitter (UART) read the FIFO and sent these 29 samples from the FPGA to a PC through a USB link. This UART was configured to run at 8 Mbits per second. For each detected pulse, a message of 29 ADC samples and time stamp took approximately 200 $\mu$S to send. This allowed a throughput of around 4000 pulses per second. If a second pulse was detected before the first was cleared from the FIFO, data were clocked to a second parallel FIFO. A simplified block diagram of the electronic detector system is shown in Figure 7.3. Although a 150 MS/s, 14 bit ADC is reasonably slow compared to current state-of-the-art, it is worth noting all work carried out and presented by LLNL in their research was undertaken with a 200 MS/s 14 bit ADC system [107]. The raw ADC samples were recorded on a PC for offline analysis. The processing of the raw ADC samples was performed by a custom program written in Python using the charge comparison method [109].

With the use of Bonner spheres as a variable source moderation, a number of

differing neutron fields were synthesised using three radionuclide sources; $^{241}$AmBe ((NPL reference 1095), $^{241}$AmLi (NPL reference 3250) and $^{252}$Cf (NPL reference 4774). The $^{241}$AmBe and $^{252}$Cf sources were each covered with two different sizes of HDPE sphere of diameters 12.7 cm and 20.32 cm. With the $^{241}$AmBe source, the detector was placed 75 cm from the source; a distance of 147.2 cm was used for $^{241}$AmLi and 72.4 cm for $^{252}$Cf. These distances were selected to ensure that the throughput of the detector remained below 4000 pulses per second. A Pb cap surrounded all sources, excluding the $^{241}$AmLi source (owing to its size), to suppress low energy gamma detections in the scintillator.

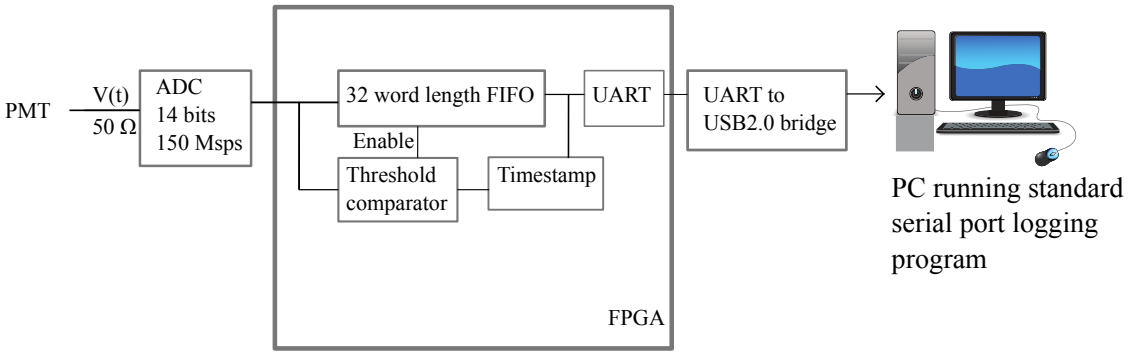


Figure 7.3: Block diagram of the detector system.

### 7.4.2 Charge comparison method (CCM)

The charge comparison method was used in this work to discriminate neutron and gamma interactions. The long integral was found by summing all 32 ADC samples. A number of short integrals were investigated and a value was chosen as 9 samples after the peak to the end of the data packet for each pulse. An example of the results observed for $^{241}$AmBe with a 20.32 cm HDPE sphere around the source can be seen in Figure 7.4.

### 7.4.3 Separating neutrons from gamma

Traditionally, following pulse shape discrimination (PSD), a line of separation is placed on a PSD scatter plot to classify events as either a neutron or a gamma [20].

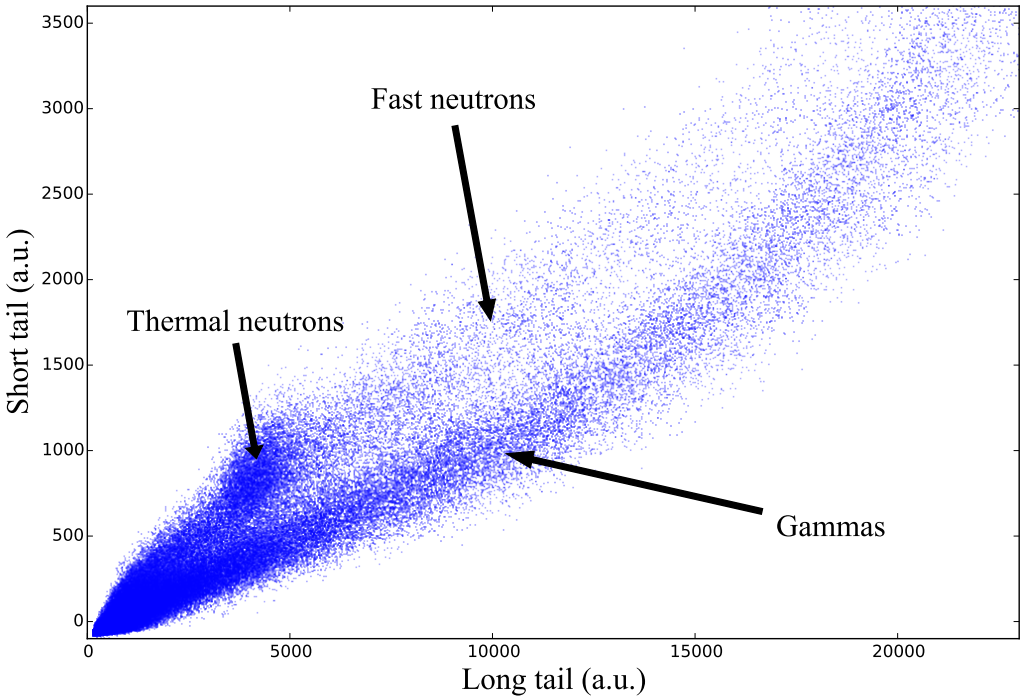


Figure 7.4: Pulse shape discrimination results from charge comparison method using $^{241}$AmBe with a 20.32 cm sphere surrounding the source.

With liquid scintillators, such as BC-501A, excellent neutron/gamma separation is observed and a line of separation is sufficient to classify these events. However, Figure 7.4 shows that placing a line of separation becomes a more onerous task.

Figure 7.5 shows a histogram of long/short integral ratios for pulse heights in the range of 3000 to 15000, resulting from $^{241}$AmBe with a 20.32 cm sphere surrounding the source. Typically, neutron and gamma pulse shape variations for a given pulse height, follow a Gaussian distribution. However, it can be seen in Figure 7.5 that the neutron and gamma regions overlap. A line of separation could be placed at the intersection of the neutron and gamma distributions (discrimination index of 0) in Figure 7.5. However, it can clearly be seen that this would lead to events being incorrectly classified, as the Gaussian distributions overlap. In this case, resulting in an underestimate of the neutron fluence.

A Gaussian mixtures model (GMM) can be used to estimate the contributing Gaussian distributions which result in an observed distribution [63] [138]. Using an iterative algorithm, expectation-maximisation, the maximum likelihood parameters

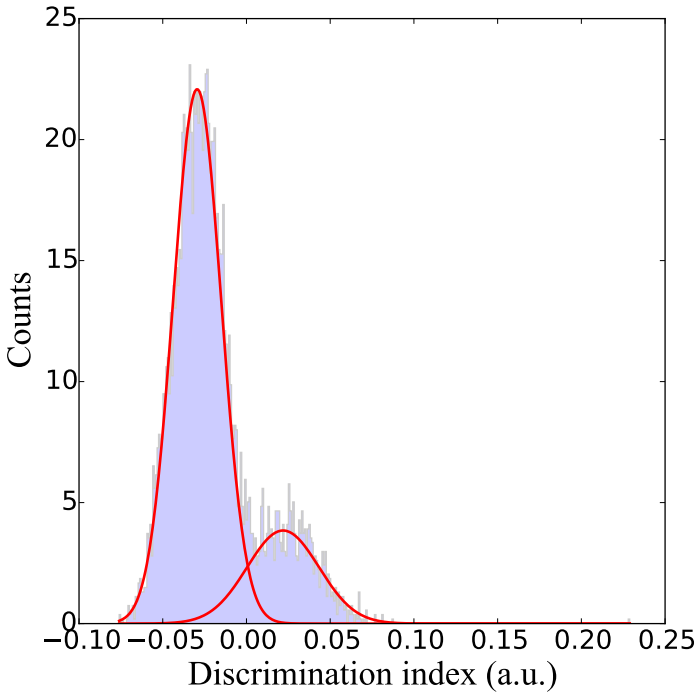


Figure 7.5: Filled histogram of pulse heights in the range 3000 to 15000 for 200 different discrimination indices using a $^{241}$AmBe with a 20.32 cm sphere surrounding the source. The estimated fits for these distributions are shown in red. The left-hand distribution is the gamma pulses and right-hand neutron pulses.

of the two Gaussian distributions are found. The GMM within the Python library *scikit-learn* was used to fit two Gaussian distributions shown in red in Figure 7.5. In this work it is assumed that the number of neutrons is equal to the integral of the fit performed by the GMM algorithm for the neutron Gaussian (the rightmost distribution). The GMM algorithm was applied to pulse heights in the region of 2000-3000 and secondly 3000-15000. The individual counts were summed to find the total neutron count (above the pulse height threshold of 2000).

### 7.4.4 Thermal neutron assay

With the $^{6}$Li scintillator studied in this research, the thermal neutron cluster lies within the fast neutron plume. Using the LLNL smaller scintillator (number 9038),

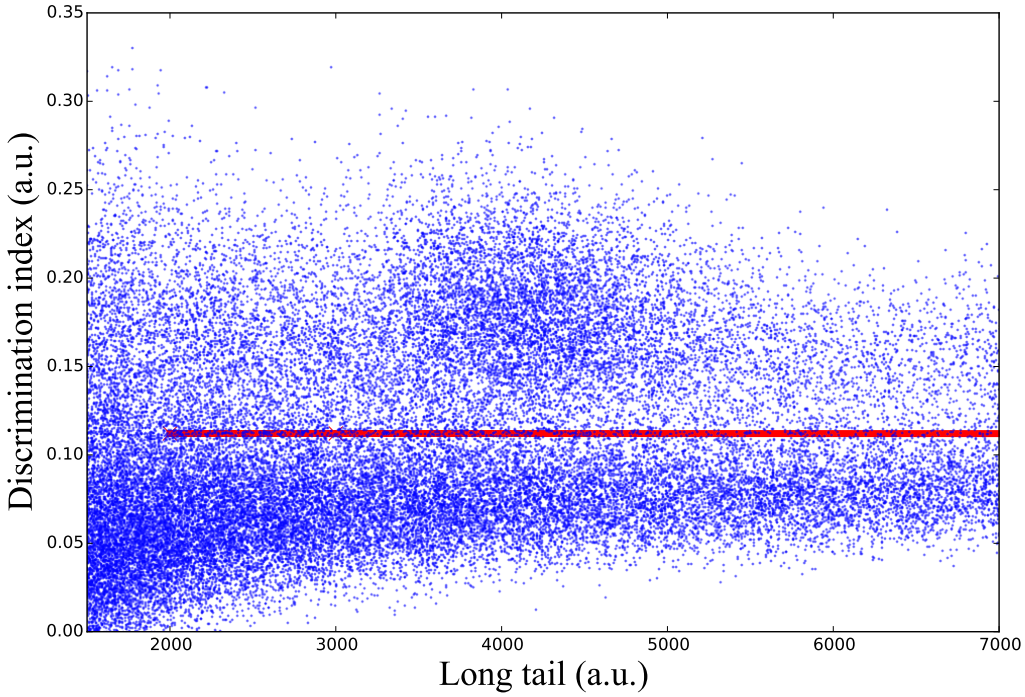


Figure 7.6: PSD scatter plot using $^{241}$AmBe with a 20.32 cm sphere surrounding the source. This plot is limited to show just the thermal cluster region. The red line is the line of best separation found using the GMM algorithm. This separation is then used to find an approximate neutron pulse height spectrum. See text for further explanation.

the cluster of thermal neutrons can clearly be seen in Figure 7.4 at around 4500,1000.

The statistical method outlined in the previous section detailing fast neutron assay cannot classify individual events as being neutron or gamma interactions. Therefore, to plot an approximate neutron pulse height spectrum, a line of separation was used. As previously discussed, this line of separation will mean misclassification of some events due to the overlapping Gaussian fits observed in Figure 7.5. However, for the purposes of performing the thermal neutron assay this does not matter. The mid-point of the two pulse height distributions found by the GMM algorithm (for example at discrimination index 0.0 in Figure 7.5) was used to find a marker for the separation between neutron and gamma events. The resulting PSD scatter plot with this line of separation (shown in red) is shown in Figure 7.6.

A plot of the resulting neutron pulse height spectrum can be seen in Figure 7.7,

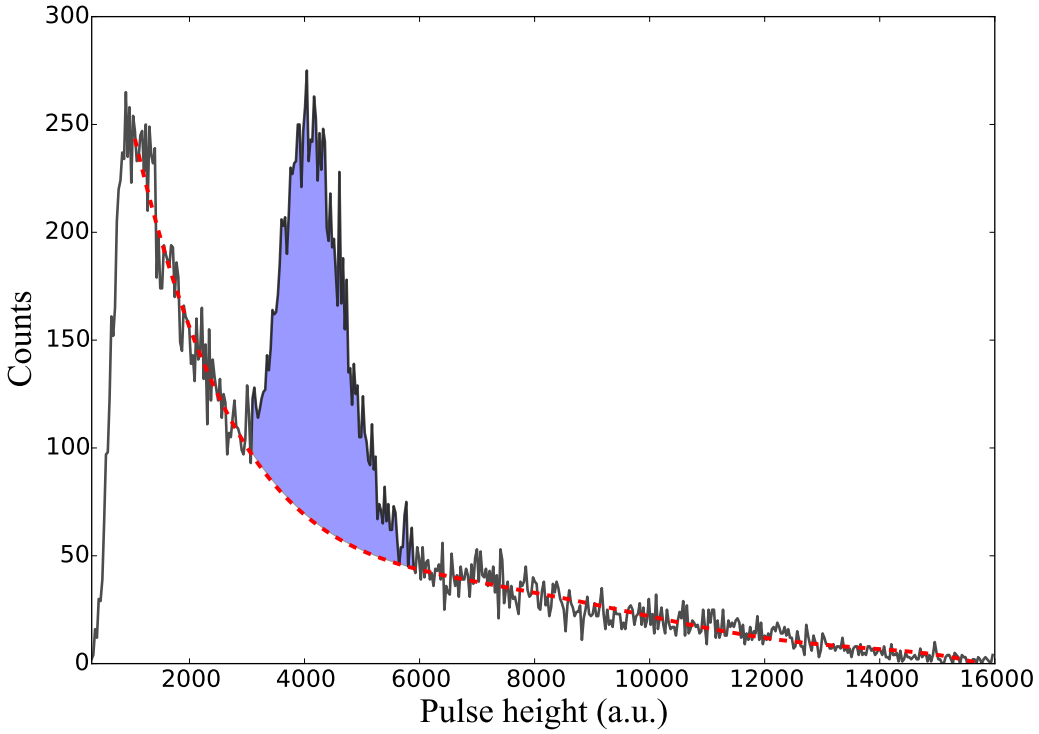


Figure 7.7: Neutron recoil pulse height with a $^{241}$AmBe source with a 20.32 cm Bonner sphere around the source. The shaded blue area denotes the thermal neutrons. The dashed red line is the line of best fit for the recoil pulse height with the thermal neutrons removed.

with the spectrum shown as a solid black line. The thermal cluster can be clearly seen between pulse heights of 3000 and 6000. In this work it was proposed that by applying a line of best fit to the data outside of the bound of the thermal cluster, a fit for the data without this thermal peak could be obtained. This was performed by applying a polynomial fit to the data outside of the bounds of 3000 to 6000, the resulting fit is shown in Figure 7.7 as a dashed red line. Within the bounds of the pulse heights found in the thermal cluster, the total integral was subtracted from the integral of the polynomial fit. This number was then taken to be the number of thermal neutrons and is shown in the blue shaded region in Figure 7.7. Having the highest thermal content in the fields studied in this work, the limits for the upper and lower bound of the thermal cluster were found using the $^{241}$AmBe with a 20.32 cm diameter HDPE (Bonner) sphere around the source field. These upper

and lower limits were then fixed at pulse heights 3096 and 5927 for the remainder of the experiments.

## 7.5 Results

### 7.5.1 Capture gating

The larger of the two $^{6}$Li-loaded plastic scintillators (serial number 9023) was exposed to a bare $^{241}$AmBe source and 5634859 events triggered the FPGA during 16 hours exposure time. 4854168 were below the saturation level of the ADC and were accepted as valid events for further processing. The scatter plot for CCM on the data can be seen in Figure 7.8.

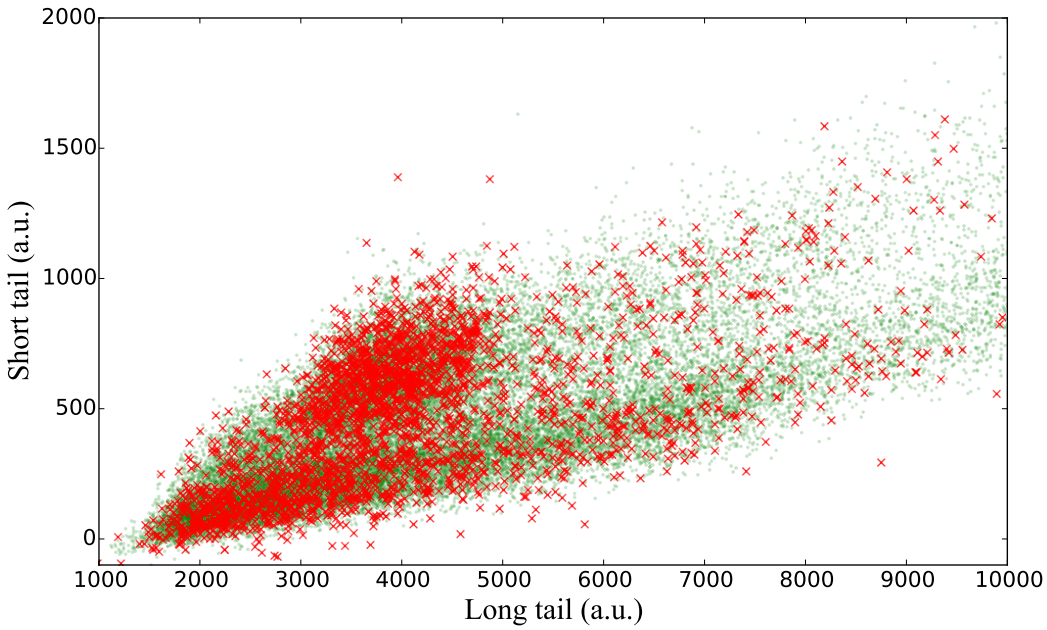


Figure 7.8: Pulse shape discrimination results from charge comparison method using a $^{241}$AmBe source (using the larger of the two scintillators (serial number 9023)). Green events correspond to non-gated events, and red corresponds to the second pulse within a gated time window.

The green events in the background represent an event for which a single trigger occurred and no further events were recorded within a 13 $\mu$s gated time window.

Where two events occurred within the gated time window, the second of these two events is shown in red. The total number of gated events was 5220. It would be expected, if all these events were neutron captures, that the red dotes would cluster around the neutron capture region of pulse heights between 3000 and 6000. However, it can be seen that a number of these events appear to have been gamma interactions. Regardless of the misclassification of these events, these experimental results are in the same order of magnitude as the simulations in the work.

### 7.5.2 Thermal neutron assay

Seven neutron fields synthesised from three different sources were investigated in this work. Neutron recoil pulse height plots for a sample of the synthesised fields studied in this research are shown in Figure 7.9.

An $^{241}$AmBe source with a 20.32 cm Bonner sphere around the source was used to synthesise a field with both fast neutrons and high thermal neutron content. Inspection of Table 7.1 shows that for this configuration, from 153033 triggered events, 21104 fast neutron interactions occurred and 7761 thermal neutrons were captured in the detector. This experiment was repeated and the repeatability of the algorithm was investigated for 105946 triggered events. The two ratio of fast to thermal neutrons for each experiment was 3.0 and 2.7, which is reasonably consistent.

A cadmium container was installed surrounding the front and sides of the detector to remove this thermal content from the field. The results are shown in Figure 7.9b. It can clearly be seen that the cadmium captures a significant number of the thermal neutrons, confirming that the presence of this peak is due to the thermal neutrons when no container is present. This is further compounded by the results shown in Figure 7.9d for an $^{241}$AmBe field with no moderation, and hence, low thermal neutron content in the field. Figure 7.9c shows a neutron field of $^{252}$Cf surrounded by a 20.32 cm Bonner sphere.

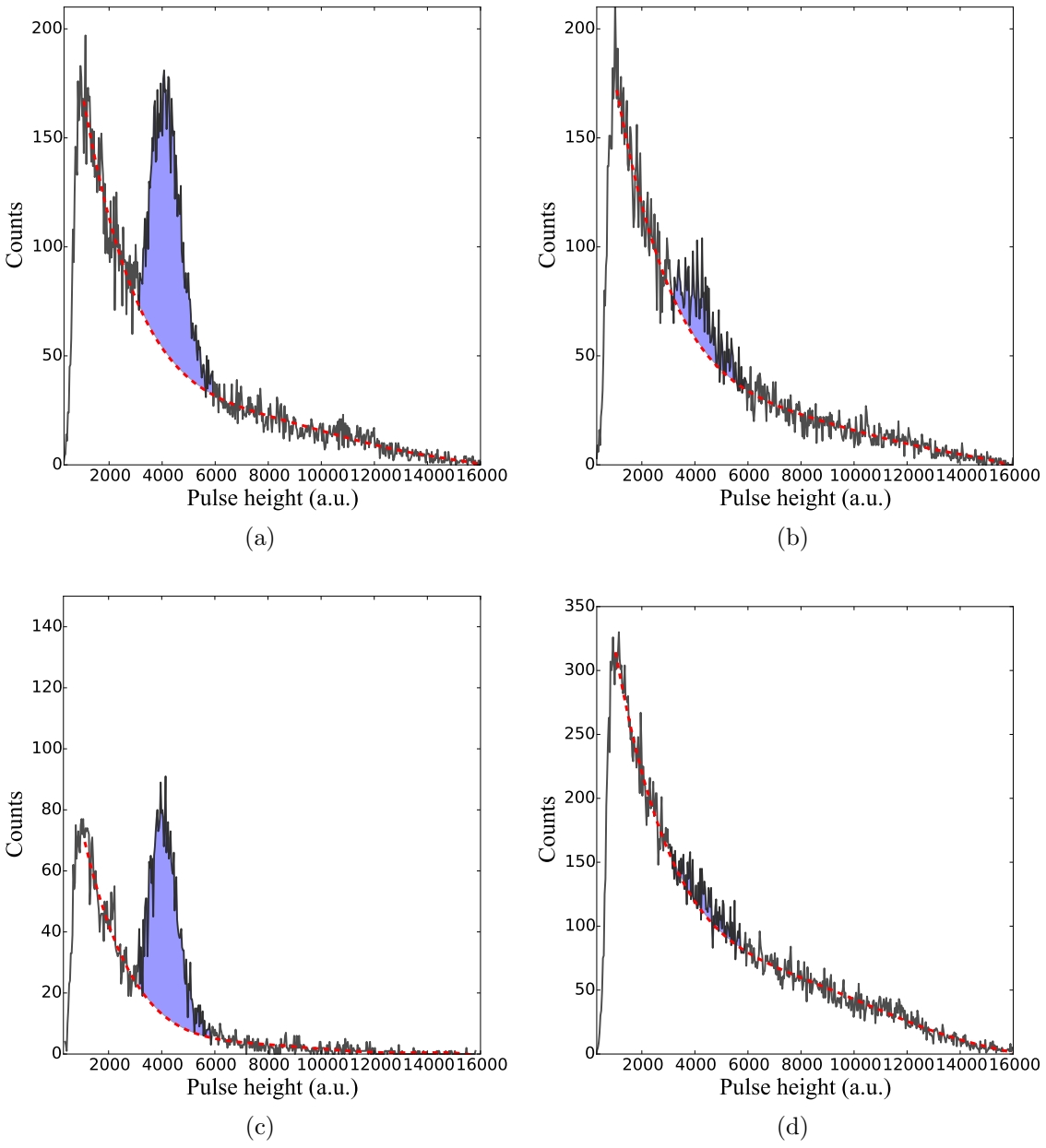


Figure 7.9: A selection of four contrasting experimental measurements from the total dataset of 9 measurements. Neutron recoil pulse height, with shaded blue area denoting the thermal neutrons. The dashed red line is the line of best fit for the recoil pulse height with the thermal neutrons removed. Neutron fields for (a) $^{241}$AmBe surrounded by a 20.32 cm Bonner sphere, (b) $^{241}$AmBe surrounded by a 20.32 cm Bonner sphere and detector enclosed in a Cd vessel, (c) $^{252}$Cf surrounded by a 20.32 cm Bonner sphere (d) $^{241}$AmBe with no moderation.

Table 7.1: Table detailing the sources used with the two different sized scintillators in this work. Unless otherwise stated, Pb cap installed over each of the sources.

| Source | Moderation (Bonner sphere size) | Additional Notes | Number of triggered events | Fast neutrons | Thermal neutrons | Fast to thermal neutron ratio |
|---|---|---|---|---|---|---|
| $^{241}$AmBe | 20.32 cm | Cd vessel | 105813 | 16013±127 | 1073±33 | 14.9±0.6 |
| | 20.32 cm | | 105946 | 14934±122 | 4942±70 | 3.0±0.1 |
| | 20.32 cm | | 153033 | 21104±145 | 7786±88 | 2.71±0.05 |
| | 12.7 cm | | 108535 | 22886±151 | 3467±59 | 6.6±0.2 |
| | None | | 114720 | 30786±175 | 651±26 | 47.3±2.2 |
| $^{241}$AmLi | 12.7 cm | No Pb cap | 199910 | 0 | 1835±43 | n/a |
| $^{252}$Cf | 20.32 cm | | 123410 | 4723±69 | 2619±51 | 1.8±0.1 |
| | 12.7 cm | | 122826 | 6471±80 | 1667±41 | 3.9±0.1 |
| | None | | 121018 | 10083±100 | 93±10 | 108.4±13.7 |

Table 7.1 shows all the results recorded in this research. Events with a pulse integral of 3000 (the lower limit of the thermal cluster) or greater are classified as a fast neutron. It can be seen that by surrounding the radionuclide source with Bonner spheres of increasing diameter up to 20.32 cm, a higher thermal neutron content in these fields is recorded.

The $^{241}$AmLi surrounded by a 12.7 cm Bonner sphere field highlighted shortcomings in the GMM algorithm when applied to this technique. This field was specifically chosen to investigate performance of the technique in the presence of a high gamma, low neutron field. Figure 7.10 shows the PSD scatter plot recorded with 2x10$^{6}$ triggered events. It can be seen that the gamma/neutron ratio of this source was extremely high. With very few fast or thermal neutrons compared to the high gamma flux, the GMM algorithm predicts that the observed thermal events are gamma interactions. The thermal assay algorithm was adapted such that if the GMM algorithm estimated 1500 or fewer total neutron interactions, it resorted to a user-configured threshold between gamma and thermal neutrons. In this case, the fast neutron background was too low, and the number of events in the thermal neutron region was considered to be the thermal neutron count.

The uncertainties shown in Table 7.1 assume Poisson count statistics. This matter is partially investigated in Chapter 8, section 8.4.3 with a number of repeated

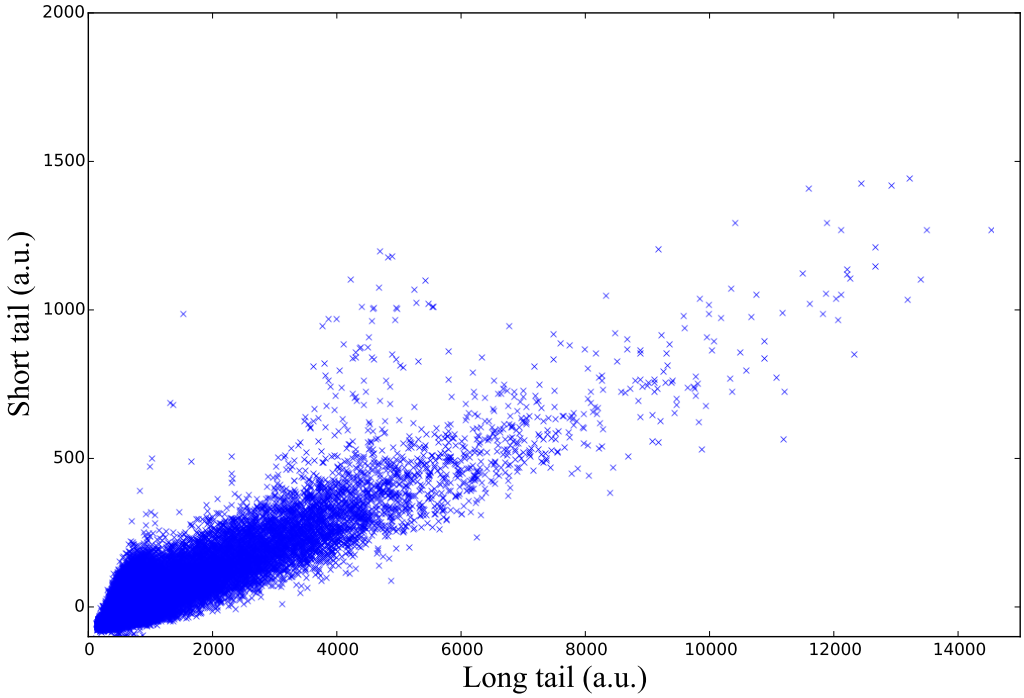


Figure 7.10: Pulse shape discrimination results from charge comparison method using a $^{241}$AmLi source. A Pb cap did not surround the source in this experiment (owing to the size of the source) and as such a high gamma to neutron ration was observed in this field.

measurements. However, significant further investigation would still be required to fully ensure this validity. Firstly, investigation would be required to investigate how different gamma fluences influence the uncertainty of the neutron assays. Secondly, a number of repeated time of flight measurements for a given field would be very insightful.

## 7.6 Conclusion

A new technique has been investigated for thermal neutron assay with a $^{6}$Li-loaded plastic scintillator. Thermal neutron assay has been performed on 7 different neutron fields synthesised from $^{241}$AmBe, $^{241}$AmLi and $^{252}$Cf radionuclide sources. This thermal assay was performed by removing the fast neutron background count within the pulse-height range of detected thermal neutrons. A statistical technique, Gaus-

sian mixtures model, has been used to perform fast neutron assay with non-ideal neutron/gamma separation.

Capture gated $^{10}$B-loaded liquid scintillator detectors are an established thermal neutron detection technique. Simulations of one of these detectors with a $^{6}$Li-loaded plastic scintillator were performed. When compared to $^{10}$B, the lower neutron capture cross-section and fractional mass content of $^{6}$Li results in a low efficiency thermal neutron detector. Furthermore, it was observed through experimental work that not all of the capture gated events were that of a signal found in the thermal neutron region of a PSD scatter plot. It was assumed these events outside this region were gamma interactions. Working in a high gamma, low neutron field would further hinder thermal neutron detection using this technique.

The algorithms are such that after calibration, no user input is required. The techniques described in this work have been successfully implemented as algorithms and tested on a number of different fields in this manner. The algorithms described lend themselves well to implementation into a portable real-time neutron detection system to perform neutron dosimetry.

The applicability of the techniques described in this research provide a method for performing both fast and thermal neutron assay beyond that solely of a $^{6}$Li-loaded plastic scintillator. Scintillators for thermal neutron detection such as CLYC and $^{10}$B-loaded plastic scintillators appear to be suitable to use this technique for fast and thermal neutron assay [21, 22].

## 7.7 Acknowledgements

The authors would like to express thanks to Natalia Zaitseva and the team at LLNL for providing the scintillator. The authors would like to acknowledge the funding support from EPSRC and National Physical Laboratory, Teddington, UK. The authors acknowledge the use of the package Matplotlib for all plots in this research [129]. The data generated in this work are available from the Lancaster University data archive [139].

# Chapter 8

# A novel approach to neutron dosimetry

## 8.1 Abstract

Having been overlooked for many years, research is now starting to take into account the directional distribution of neutron workplace fields. This paper reports on the development of an instrument which can estimate the effective dose of a neutron field, accounting for both the direction and the energy distribution. A $^{6}$Li-loaded scintillator was used to perform neutron assays at a number of locations in a water phantom. The variation in thermal and fast neutron response to different energies and field directions was exploited, and the modelled response of the instrument to various neutron fields was used to train an artificial neural network (ANN). Experimental results were obtained for a number of radionuclide source based neutron fields to test the performance of the system. The results of experimental neutron assays at 25 locations in a 20x20x17.5 cm$^3$ water phantom were fed into the trained ANN. A correlation between neutron counting rates in the phantom and neutron fluence rates was experimentally found. The resulting estimates of effective dose rate had an error of 45% or less, regardless of energy distribution or direction. The ANN was also trained to learn ambient dose equivalent and the resulting ambient dose equivalent rate for the experimental results was found to be 60% or less for the 14 experimental fields investigated.

## 8.2 Introduction

Human exposure to ionising radiation is a health risk which radiation protection practices attempt to reduce. Depending on the type of ionising radiation, a differing risk is experienced. As such, the dose from each type of radiation (such as gamma, neutron, beta) should be considered when assessing this risk.

In neutron dosimetry, the overall risk to the human body is classified as the sum of the risks to individual tissue/organs. However, when considering males and females, they have a different overall risk weighting due to anatomical differences. Furthermore, weighting factors are based on a specific size of human. Depending on the neutron field energy and direction of incidence, the committed dose to each of these organs differs. Therefore, it can be seen that the neutron radiation exposure risk to a human is a complex problem to quantify. Considering these factors, from an instrumentation standpoint, estimating the risk for a specific individual is a difficult, if not currently impossible, task.

The radiation protection quantity *effective dose* can be used to provide an estimation of the health risk due to exposure to a neutron field [30]. Using this quantity, the risk estimate accounts for both the energy distribution and direction of incidence of a neutron field. Using conversion coefficients, a neutron fluence can be transformed into an effective dose for a given incidence of neutron field, by applying fluence to effective dose conversion coefficients that vary with energy and angle [30]. Figure 8.1 shows how the effective dose coefficients change for antero-posterior (AP), postero-anterior (PA), left-lateral (LLAT) and right-lateral (RLAT) incident radiation. It can be seen that the greatest health risk is experienced with the AP direction of incidence, while the lowest risk is with RLAT incidence.

A number of important points should be noted with regard to effective dose. The ICRP guidelines describe it as something that cannot be measured, and as such, one can only estimate effective dose. Secondly, when considering a workplace field, it is assumed that a single directional component will not dominate. More likely, a complex directional field will result, which will likely vary with neutron energy. As such, using only the published fluence to effective dose conversion coefficients for a limited number of directions, it is a near impossible task to estimate the effective dose of a workplace neutron field with any degree of accuracy.

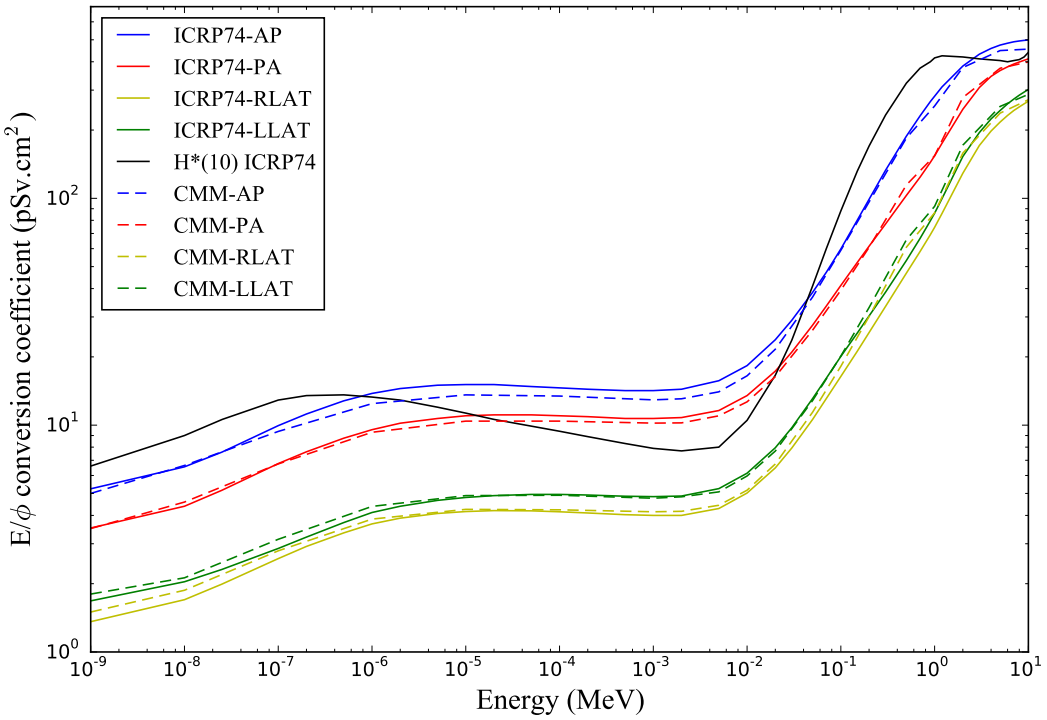


Figure 8.1: Effective dose coefficients for AP, PA, RLAT, LLAT are shown for both ICRP74 and the CMM phantom calculated values described in this work (see section 2.2). It can be seen that in some energy regions, *H*(10)* does not always provide a conservative estimate of the neutron dose.

In light of the practical shortcomings of effective dose, the quantity *ambient dose equivalent H*(10)* is currently used for operational neutron dosimetry. This quantity is supposed to be a conservative measure of the risk, carrying a higher conversion coefficient than the AP fluence to effective dose conversion coefficient. However, it can be seen in Figure 8.1 that this is not the case for the values currently used in UK industry from ICRP74 [30]. In the conservative energy regions, for radiation workers, this extra margin of safety has the potential to limit working practices. Furthermore, the accuracy of radiation health studies is limited by the mostly conservative estimates of the neutron dose. It should be noted that ICRP116 provides an updated set of coefficients to reduce this conservatism, however it still falls short in some areas of the spectrum [19, 31]. In this research, the data from

ICRP74 have been used as UK legislation is currently based upon this.

In this work, the authors have developed a novel instrument to estimate the effective dose of a neutron field. No instrument currently exists which, from a single location, can estimate effective dose [90]. Recent advances in lithiated plastic scintillators and signal processing techniques now allow both fast and thermal neutron assay to be performed in a single scintillator [107] [140]. It was proposed that by moving this $^{6}$Li-loaded scintillator detector within a water phantom and observing the distribution of fast and thermal neutrons within a moderating phantom, an artificial neural network (ANN) could be trained to learn the corresponding effective dose of these fields. The concept of using ANNs to estimate effective dose has previously been investigated with computer simulations [84, 141]. These methods consisted of a single doped scintillator and relied on localising neutron capture within a large scintillator. However, no efficient signal processing methodology was identified to localise neutron capture within a scintillator.

It is believed that in the research presented in this paper, for the first time, a single instrument has been able to estimate effective dose. The instrument has been experimentally tested in multidirectional fields and an error (i.e., the difference between estimated and calculated effective dose rate) of 45% or less was observed when estimating effective dose rate for all fields investigated with a data capture time of 90 minutes or greater.

## 8.3 Methodology

### 8.3.1 Modelling neutron distributions in a water phantom

The initial investigations of this instrument were based around Monte Carlo computer modelling. These set out to understand the distributions of thermal and fast neutrons in a water phantom. A scintillator loaded with 0.14% fractional mass of $^{6}$Li, measuring 25 mm diameter and 18 mm thickness was modelled within a water phantom of volume 20x20x17.5 cm$^{3}$. Individual simulations were performed for a number of different detector locations in the water phantom using Monte Carlo radiation transport package, MCNP v5.0 [88]. In MCNP, materials were simulated using the ENDF/B-VII.0 neutron cross-section tables at temperature 293.13 K. To

handle low energy thermal scattering of neutrons below 5 eV, MCNP has thermal treatment for a variety of material types. For s($\alpha$, $\beta$) thermal treatment, *poly.01t* and *lwtr.01* were included in the MCNP input file, for the scintillator and water respectively. Using the particle tracking file (PTRAC), neutron recoil and neutron capture events within the scintillator were recorded. If an event resulted in a neutron energy deposition of greater than a fixed energy threshold, a fast event was tallied. This threshold was chosen to be the energy region beyond the fixed light production arising from $^{6}$Li neutron capture in the scintillator. Further details regarding this can be found in the results section of this work. It was decided to perform the assay at 25 locations on the horizontal plane at the mid-height within the water phantom.

Simulations were performed for 30 minutes of computer time at 25 locations in a 5 x 5 grid pattern in the water phantom. The geometric centre of the scintillator was located at x locations [-7, -3.5, 0, 3.5, 7] and y locations [-7, -3.5, 0, 3.5, 7] (all locations in cm), where 0,0 cm was the centre of the water phantom. For this proof-of-concept instrument, data acquisition for z axis displacements of the detector was not implemented. As such, the training and testing of the instrument does not account for any top or bottom based neutron field directions.

### 8.3.2 Estimating effective dose for a workplace field

To measure the performance of the proposed instrument, a method needed to be identified to calculate the effective dose of an experimental field. Using ICRP published conversion coefficients, doses can be calculated for AP, PA, RLAT, LLAT, ROT and ISO fields. However, this field is assumed to be a parallel beam. Calculating effective dose close to radionuclide neutron sources becomes a difficult task due to the divergent beam nature of the field. Furthermore, in a workplace field, it is anticipated that a complex directional neutron distribution would be present.

Although it may be possible to create rough estimates of the effective dose of a real-world field by attempting to break it down into the above six components, it was decided that values derived from calculations based on an anthropomorphic phantom would better reflect the reality of the workplace. Tom Jordan's Computerised Man Model (CMM) was selected for this purpose as it was listed in the input geometry format of the radiation transport code MCNP [142].

Having completed an initial check on the model, the male phantom was transformed into an hermaphroditic phantom by treating (a) the pectoral muscles as representing breast tissue, and (b) a volume of tissue in front of the spine as representing ovary tissue. F6 (dose) tallies were created for both neutron and photon interactions for each tissue of interest. A complete list of cells used to approximate the organs and tissues of interest is given in the supplementary material for this work [143]. A number of adjustments to the model were required to observe the agreement shown in Figure 8.1.

All experimental data published in this work were measured at the National Physical Laboratory (UK) in the low scatter facility [144, 145]. The dimensions of the room were 25x18x18 $m^3$, with the designated low scatter area being approximately 18x18x15 $m^3$, and the source was installed close to the centre of this space. For each experimental test performed, a corresponding effective dose at that given location was calculated by modelling the CMM phantom within the low scatter facility.

In order to experimentally synthesise some near-isotropic fields, it was anticipated that a shadow cone in front of a source could be used. However, the shadow cones available formed a shadow in the region of tens of cm, rather than the height of a person. Therefore, to calculate the effective dose behind the shadow cone, the phantom was reduced in scale by a factor of ten, and the density of each tissue increased by a factor of ten. This was in a method analogous to the principles of microdosimetry using tissue equivalent proportional counters [146]. Further details are available in the supplementary material published with this research [143].

### 8.3.3 Artificial neural network approach

Artificial neural networks (ANNs) are well proven for their abilities in pattern recognition systems and have previously been researched for neutron spectrum unfolding purposes [64, 65, 66, 67, 48]. Once a neural network has been trained, the network can be deployed into a fast real-time system. It was proposed that by observing the distribution of fast and thermal neutrons within a water phantom, an ANN could be trained to learn the corresponding effective dose of these fields.

The C based software library FANN, version 2.2.0, was used for the investigations

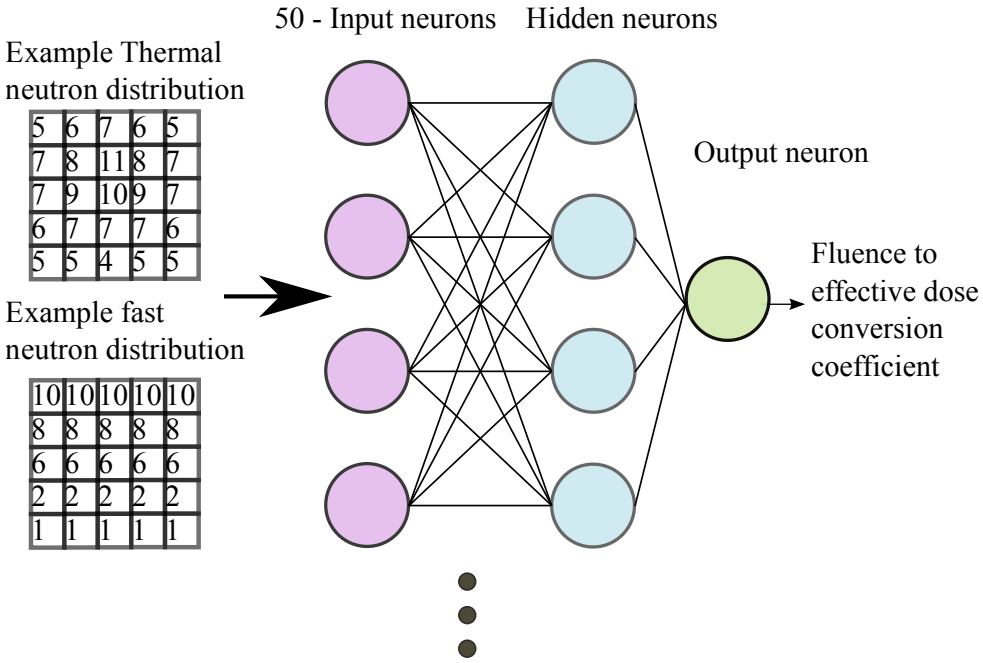


Figure 8.2: Simplified schematic of the ANN used in this research to estimate the fluence to effective dose conversion coefficient based upon the assayed thermal and fast neutron distributions within a water phantom.

in this work [105]. For ANN training, the resilient propagation (RPROP) learning algorithm has been applied [106]. Specifically, the iPROP- method described by Igel et al [147]. By using individual step sizes for weight updates of each neuron, the RPROP algorithm removes the need for optimisation of a learning rate.

Number of layers, number of neurons and activation functions could all be changed for a given set of input data to optimise the learning of the pattern. The architecture of the network used in this work is shown in Figure 8.2. The input data consisted of 50 input neurons (fast and thermal neutron assay at 25 locations), feeding into 3 layers of neurons with a sigmoid activation function. The resulting output of the ANN was an estimate of the fluence to effective dose conversion coefficient for the given neutron field.

### 8.3.4 Experimental details

A $^{6}$Li-loaded scintillator provided by the Lawrence Livermore National Laboratory (LLNL) was used in this work [107]. The scintillator measured 25 mm in diameter by 18 mm thick (denoted by the LLNL number 9038) and was coupled to an ET Enterprises 9111 PMT with Eljen EJ-550 optical grease. It was then enclosed in a light proof housing. The PMT was housed in an ET Enterprises PDM9111 housing with a C673BFP tapered distribution voltage divider. The high voltage was set to +848 V.

The PMT signal was connected to an Analog Devices AD9254 150 mega-samples-per-second (MS/s), 14 bit analogue-to-digital converter (ADC), located in the control room of the low scatter facility. Low loss, high bandwidth coaxial cable was used to preserve signal quality (Huber + Suhner SX07262BD). Each digitised ADC sample was clocked to an Altera Cyclone IV EP4CE115 field-programmable gate array (FPGA). Further specifications on this digitiser can be found in the authors' previous work [140].

An open top water phantom was used, measuring 20x20x20 cm$^3$. The water was only filled to a height of 17.5 cm to avoid any spillage during the movement of the detector between assay locations. The PMT was suspended from the top of the water phantom, such that the centre of the scintillator was at a height of 8.75 cm above the bottom of the phantom. The PMT was moved in the X-Y plane by a lead screw on each axis, with each axis supported by a carriage and rail system. Each lead screw was coupled to a 12 V 0.33 A stepper motor with a step angle of 1.8 degrees and a peak holding torque of 2.3 kg/cm. The stepper motors were controlled by an Arduino Uno R3 microntroller board coupled to a motor control PCB. Commands to control the detector location in the water phantom were sent to the microcontroller board from the control room over an Ethernet cable using USB to Ethernet converters at each end of the cable. The instrument as described can be seen in Figure 8.3, and a system diagram identifying equipment located in the low scatter facility and outside, in the control room, can be seen in Figure 8.4.

In post processing, the charge comparison method was used to discriminate neutron and gamma interactions in the scintillator [109]. This method compares the total pulse integral (long integral) with the short pulse integral (an area on falling

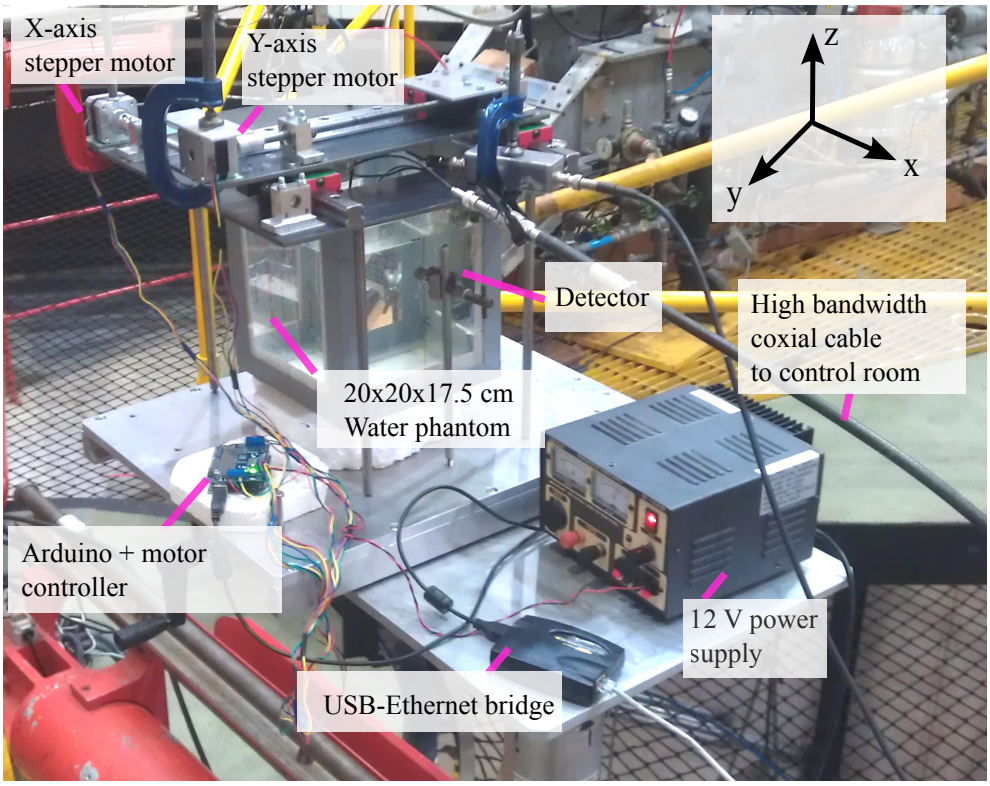


Figure 8.3: Photograph of the instrument installed in the NPL low scatter facility.

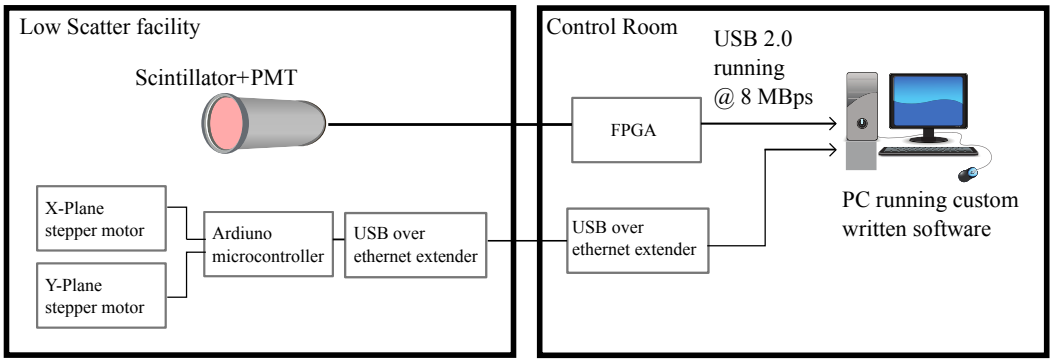


Figure 8.4: Diagram of the system, detailing equipment located in the control room and within the low scatter facility.

edge of the pulse). The charge comparison method was implemented by summing 32 ADC samples for each pulse to find the long integral. The neutron/gamma discrimination performance of a number of short integrals were investigated, with the best

performance given by a value of 10 samples after the peak to the end of the data packet for each pulse. A Gaussian mixtures model was used to perform fast neutron assay, and thermal assay was performed using a peak removal algorithm [140].

## 8.4 Results

### 8.4.1 Measuring thermal and fast neutron distributions in a water phantom

For radiation with an AP direction of incidence, the corresponding calculated effective dose conversion coefficients for $^{241}$AmBe and $^{252}$Cf were 394.7±0.4 and 337.3±0.4 pSv cm$^2$ respectively. Being comparatively close together in terms of fluence-dose conversion coefficients, it was decided to see if a difference between these two fields could be observed in terms of fast and thermal neutron distribution in the water phantom. The sources were modelled as an isotropic emission source located 80.5 cm from the centre of the water phantom with a direction of incidence AP. Simulations were run at incremental 1 cm depths along the x axis, with the y and z locations fixed to their respective geometric centres of the water phantom. The modelled distribution of thermal neutrons at varying depths through the water phantom are shown in Figure 8.5. In the modelled results it can be seen that there was a difference between $^{241}$AmBe and $^{252}$Cf in the thermal neutron count with an increase in depth into the phantom.

The modelled results showed promise and were verified experimentally. $^{241}$AmBe (NPL serial number 1095) and $^{252}$Cf (NPL serial number 4774) sources were exposed to the water phantom at a distance of 80.5 cm, with an AP direction of neutron incidence. The geometric centre of the scintillator was aligned to the mid-height of the water. The scintillator was also aligned to remain fixed in the midpoint of the y axis in the water phantom. Fast and thermal neutron assay was performed at a number of locations along the x axis. The orientation of the axes can be seen in Figure 8.3. Measurements were performed at each location for 30 minutes.

The modelled and experimental thermal neutron distributions can be seen in Figure 8.5. It can be seen that the experimentally measured thermal distributions closely follow the modelled results for $^{241}$AmBe and $^{252}$Cf. An $^{241}$AmLi source (dose

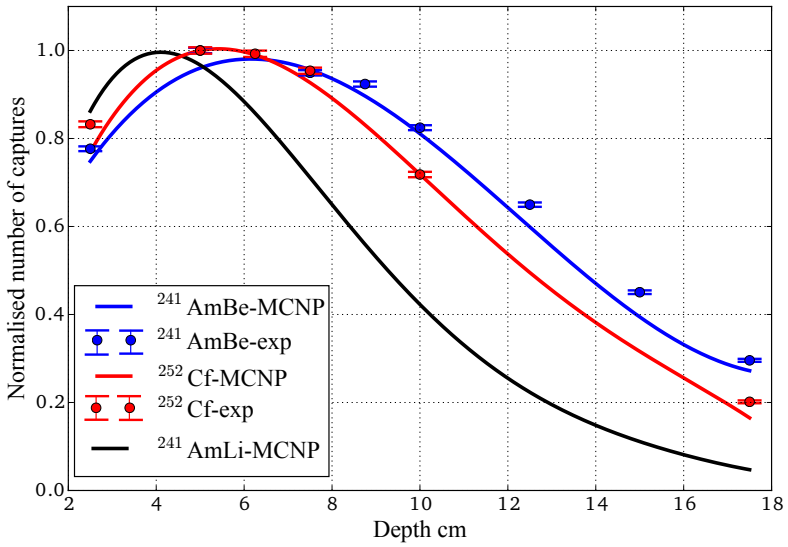


Figure 8.5: Modelled (denoted by MCNP) and experimental (denoted by "exp") thermal neutron count with a varying assay depth $^{241}$AmBe and $^{252}$Cf . The dashed lines shown are the experimental results and solid lines the modelled results. The data in each set were normalised to the maximum count across all of the measurement locations in that set. A neutron field with a greater contribution of thermal neutrons ($^{241}$AmLi) is also shown for comparison.

conversion coefficient of 151.3±0.3 pSv cm$^2$) was modelled to provide an indication of the difference in distribution that would be observed with a field with a greater contribution of thermal neutrons.

In the experimental results, an event was classified as a fast neutron if it had a greater amplitude than a pulse found in the thermal neutron cluster. An example of a pulse shape discrimination plot, illustrating the fast neutron region and the thermal cluster is shown in Figure 8.6.

By observing the thermal to fast ratio of the experimental results, the modelled fast neutron threshold was changed until a close agreement was observed between the modelled and experimental results. This fast neutron threshold was found to be 2.1 MeV in the modelled results. The resulting experimental and modelled thermal to fast neutron ratios distributions, with varying depth, can be seen in Figure 8.7.

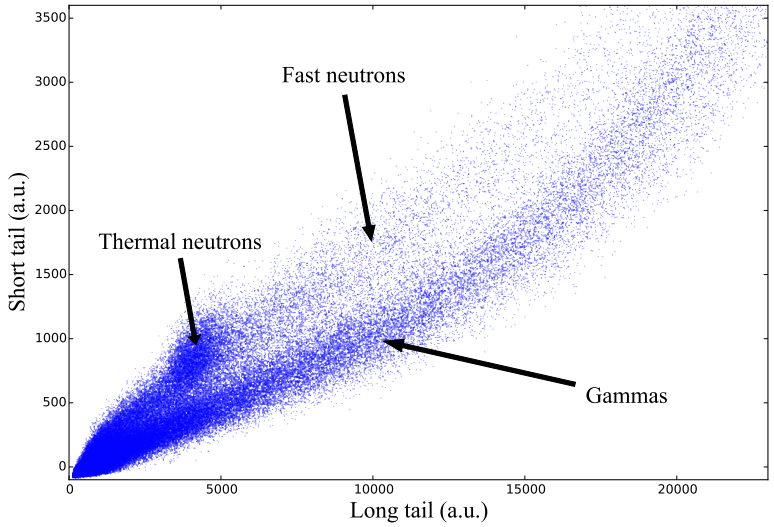


Figure 8.6: An example of a pulse shape discrimination scatter plot obtained in this work. The thermal and fast neutron regions are shown, as well as the gamma events, which are rejected.

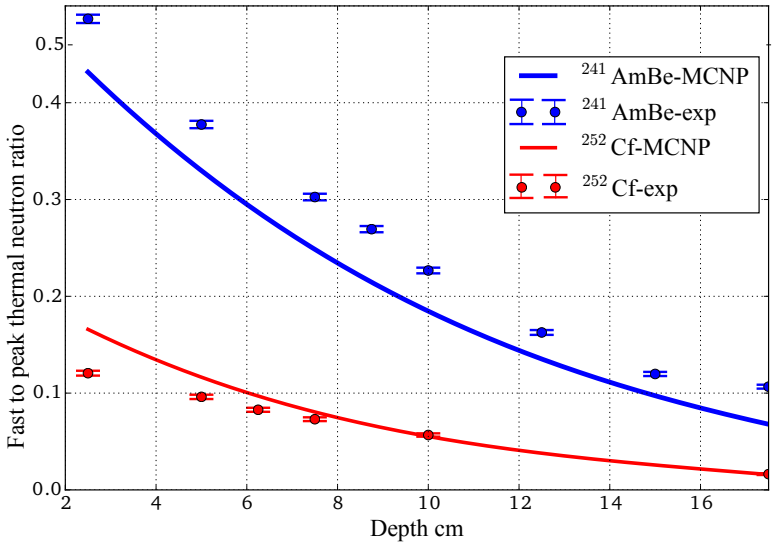


Figure 8.7: Modelled (denoted by MCNP) and experimental (denoted by "exp") thermal to fast neutron ratio with a varying assay depth for $^{241}$AmBe and $^{252}$Cf . The dashed lines shown are the experimental results and solid lines the modelled results.

### 8.4.2 Training the ANN

Following the promising agreement between the modelled and experimental neutron distributions in the water phantom, it was decided to train an ANN with a number of simulated neutron field responses of the instrument. Ten different neutron spectra were selected. These were chosen for their range of resulting effective dose conversion coefficients with AP direction of incidence. The highest of these coefficients was 394.7±0.4 pSv cm$^2$ and the lowest was 9.33±0.02 pSv cm$^2$. A sample of the neutron spectra used in the ANN training set can be seen in Figure 8.8. Full details of these fields can be found in the additional supplementary information published for this work [143]. For each field, simulations were performed at 25 locations in the water phantom. For each location, thermal and fast neutron counts were extracted from the simulation.

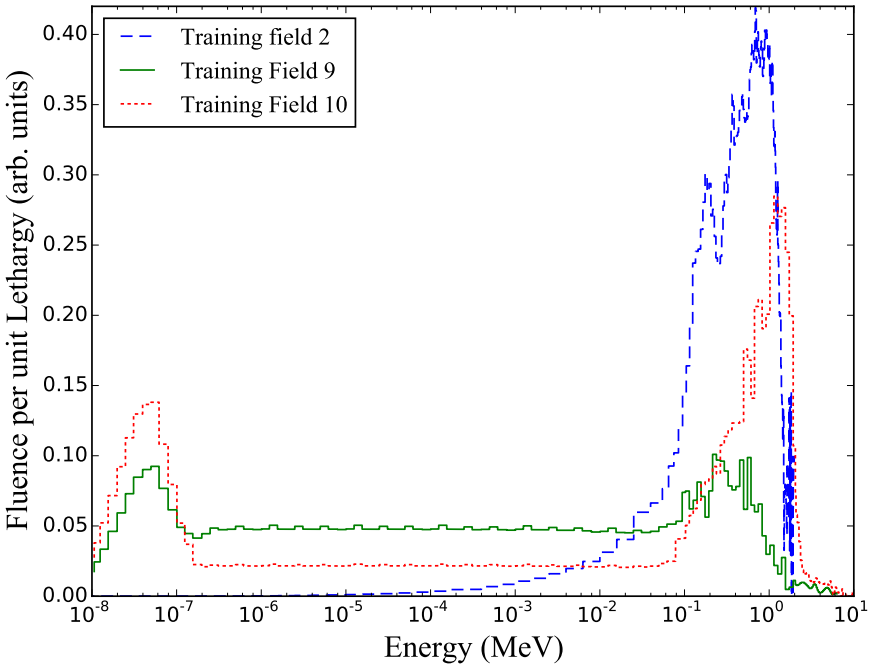


Figure 8.8: A sample of the workplace-like neutron fields used for performing MCNP simulations to find the instrument response to these fields in terms of thermal and fast neutrons.

For each field, training data were obtained for AP, RLAT, PA, LLAT angles of

incidence, and the 45 degree angles between each of the these angles. To save computer simulation time, the AP data for each field were rotated to provide a resulting PA, RLAT and LLAT response training set. This same rotation was applied for the 45 degree angle between AP-RLAT to find the remaining responses. Simulations were also performed to find the instrument response to an isotropic field.

The resulting ANN training data contained 90 examples, consisting of 10 fields, with 9 different angles of incidence for each of these neutron spectra. The data for each training example were normalised to the peak value within each set (this peak value being either a fast or thermal neutron count at any one of the assay locations). The output training data were normalised to a conversion coefficient of 600 pSv cm$^2$. An overview of the data flow within the ANN based system can be seen in Figure 8.9.

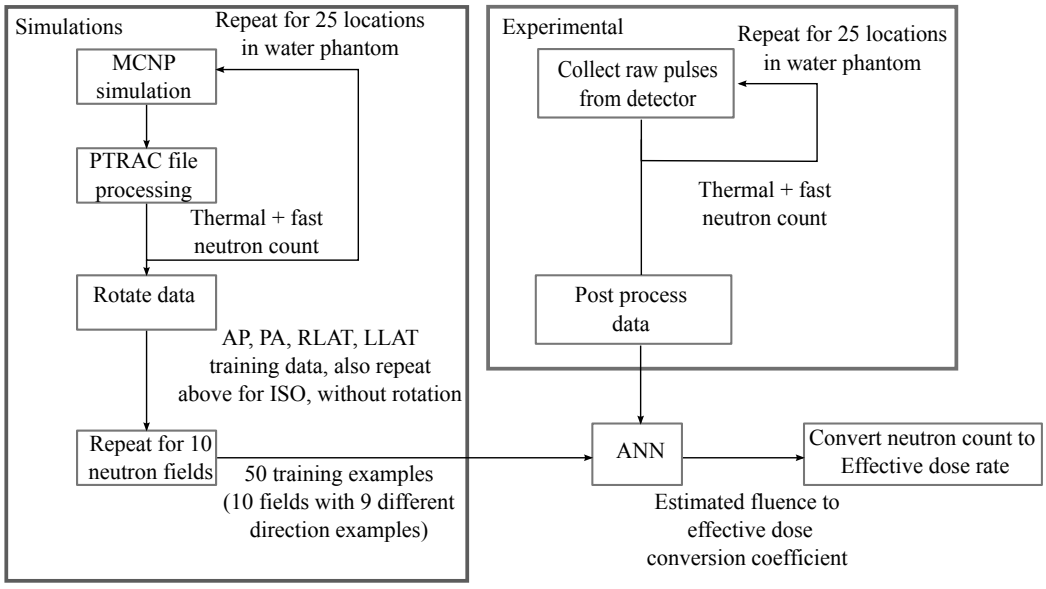


Figure 8.9: Data flow diagram. The simulated response of the instrument for 10 different neutron fields was used to train an ANN. The experimental results were passed to the trained ANN, resulting in a fluence to effective dose conversion coefficient. This coefficient was converted to an effective dose rate, by applying a conversion factor based on the total number of detected neutron events in the scintillator.

The ANN training was stopped when a total normalised mean squared error of 8x10$^{-5}$ was observed for the complete training set. It was observed that beyond this the ANN started to learn the specific training set too well and performed poorly

with data beyond the training set. An optimal setting of 1 hidden layer (with a sigmoid activation function) with 50 hidden neurons was used with the RPROP learning algorithm. Due the random initial weights used in ANN training, each trained network results in a unique output. As such, 10 networks were trained in parallel and the resulting outputs averaged to estimate the fluence to effective dose conversion coefficient. The resulting average ANN results for the training data can be seen in Figure 8.10.

It can be seen in this figure that the network struggled to accurately learn low dose fields with a conversion coefficient of 25 pSv cm$^2$ or less. It should be noted that two outliers are not shown on this graph. These ANN input values were 4.4 and 7.1 pSv cm$^2$ respectively which resulted in output errors of 220% and 187% respectively.

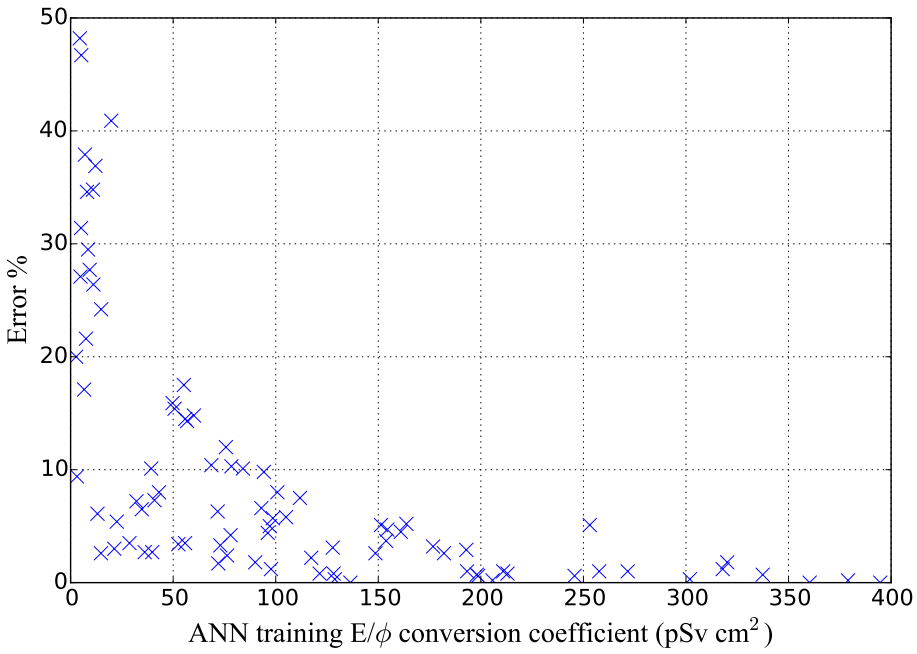


Figure 8.10: ANN error for the 90 examples, from 10 differen neutron spectra used in training. The error is classified as the percentage difference between the desired and actual output, divided by the desired value, from the average results of 10 ANNs.

### 8.4.3 Single radionuclide source field

It was decided that the first tests for the instrument would be with single radionuclide sources. Although not true to a workplace-like field (in terms of energy or directional components), $^{241}$AmBe (for RLAT directions, NPL reference 7245, and for AP, NPL reference 1095), $^{241}$AmLi (NPL reference 3250) and $^{252}$Cf source (NPL reference 4774) were first selected to test the ANN. These initial experimental results would provide an indication of the performance of the ANN when presented with experimental data for fields and directions it had seen in training. However, distances between source and detector other than 80.5 cm were investigated and the training set did not include the low scatter facility in the model. It was anticipated that room thermalisation of neutrons would produce a slightly different field at the detector, in terms of direction and energy distribution.

A single source was located at the centre of the NPL low scatter facility and the distance to the centre of the detector was recorded. Depending on source activity, differing scan times were chosen. The experimental results for these single source experiments are shown in Table 8.1. The scan time at each individual location within the phantom was kept constant. The time given in Table 8.1 is the total time that the FPGA was recording data for at the 25 locations. The resulting ANN fluence to effective dose conversion coefficients were estimated with an error of 38% or better for the 10 experimental measurements performed.

To calculate the dose rate, a preliminary method was identified for this proof-of-concept instrument. First, the neutron fluence rate at the measured distance for the given neutron emission rate of a source was calculated (these can be found in the supplementary information [143]). Due to the difference in the thermal and fast neutron detection efficiency, a multiplier of 2 was applied to the fast neutron count. The sum of the modified fast neutron count and the thermal neutrons detected per second against calculated source emission rate is shown in Figure 8.11. A fit of y=1.8x was applied to these data. The resulting method for estimating neutron fluence rate is shown in Equation 8.1.

$$N_{flu} = \frac{2A_{fast} + A_{thermal}}{t} 1.8 \tag{8.1}$$

where $N_{flu}$ is the estimated neutron fluence rate at the centre of the water

Table 8.1: Experimental results for single radionuclide sources located at a varying distances. The ANN estimated fluence to effective dose (E) conversion coefficient is shown, and the resulting E rate based on the number of detected neutron events within the water phantom.

| Neutron Source | Neutron field direction | Scan time [a] | Distance to phantom [b] | Fluence to E conversion coefficient (pSv cm$^2$) | | | E rate ($\mu$Sv/hr) | | |
|---|---|---|---|---|---|---|---|---|---|
| | | | | CMM | ANN | Error | CMM | ANN | Error |
| $^{241}$AmBe | AP | 400 | 80.5 | 384±4 | 382 | 1% | 41.1±0.4 | 41.5 | 0.9% |
| | AP | 750 | 150.0 | 349±6 | 381 | 9% | 10.8±0.4 | 9.2 | 15% |
| | RLAT | 750 | 248.5 | 182±10 | 180 | 1% | 17.9±1.4 | 18.5 | 3% |
| $^{252}$Cf | AP | 750 | 80.5 | 311±3 | 295 | 5% | 17.1±0.5 | 14.1 | 17% |
| | AP | 9 | 80.5 | 311±4 | 381 | 23% | 17.1±0.5 | 33.2 | 94% |
| | AP | 90 | 80.5 | 311±3 | 227 | 27% | 16.4±0.4 | 13.3 | 19% |
| | 45° | 750 | 80.5 | 273±3 | 170 | 38% | 12.2±0.3 | 6.7 | 45% |
| | AP | 285 | 80.5 | 311±3 | 275 | 12% | 16.4±0.4 | 14.5 | 11% |
| $^{241}$AmLi | AP | 1250 | 150.0 | 129±3 | 147 | 14% | 0.36±0.02 | 0.46 | 25% |
| | RLAT | 1250 | 175.7 | 51±2 | 48 | 5% | 0.11±0.01 | 0.11 | 1% |

[a] time in minutes.
[b] distance to the geometric centre of the water phantom from the source (cm).

phantom, $A_{fast}$ is the total fast neutron assay in the phantom, $A_{thermal}$ is the total thermal neutron assay in the phantom, $t$ is the total detection scan time, in seconds.

The outlier to the fit shown in Figure 8.11 is the $^{252}$Cf scan for 9 minutes. This is due to shortcomings in the accuracy of the GMM algorithm when small total numbers of pulse have been detected. This is discussed further in the authors' previous work [140].

This estimate of neutron fluence rate($N_{flu}$) was multiplied by the ANN estimated conversion ($E_{coeff}$) coefficient, multiplied by the number of seconds in an hour, to give the resulting dose rate in $\mu$Sv/hr as shown in Equation 8.2.

$$E_{rate} = 3600\ N_{flu} E_{coeff} \tag{8.2}$$

In Table 8.1 it can be seen that the ANN estimated the conversion coefficient for the short $^{252}$Cf scan time with a 23% error, however, the fluence rate estimate resulted in dose rate error of 94%. For longer scan times, the resulting conversion coefficient and dose rate estimates differed by less than 45% between the experimental

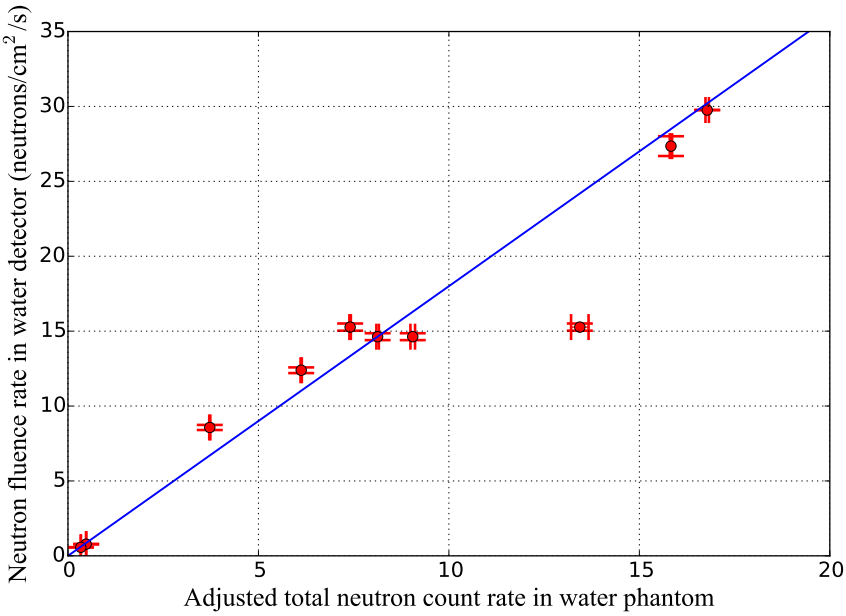


Figure 8.11: Relationship between the adjusted total neutron count rate in the water phantom and the neutron fluence rate at the given experimental distance for a given source.

Table 8.2: Experimental results investigating repeatability of results with a short scan time of 25 minutes. An $^{241}$AmBe source was located 248.5 cm from the centre of the phantom at an RLAT angle of incidence.

| Observed thermal to fast neutron ratio | Fluence to E conversion coefficient (pSv cm$^2$) | | | E rate ($\mu$Sv/hr) | | |
|---|---|---|---|---|---|---|
| | CMM | ANN | Error | CMM | ANN | Error |
| 3.89±0.03 | 182±10 | 143 | 21% | 17.9±1.4 | 17.7 | 1% |
| 4.09±0.03 | | 182 | 0.1% | | 22.1 | 23% |
| 4.26±0.03 | | 157 | 14% | | 18.8 | 5% |
| 4.63±0.04 | | 166 | 9% | | 19.4 | 8% |
| 4.83±0.04 | | 149 | 18% | | 16.9 | 6% |
| 4.40±0.03 | | 133 | 27% | | 15.8 | 12% |
| 4.34±0.03 | | 143 | 21% | | 16.8 | 6% |
| 4.52±0.04 | | 168 | 8% | | 19.5 | 9% |
| 4.18±0.03 | | 169 | 7% | | 20.3 | 13% |
| 4.45±0.04 | | 159 | 12% | | 18.7 | 5% |

and calculated values. The largest of these differences being for $^{252}$Cf at 45°.

It was decided the poor results from the 9 minute $^{252}$Cf scan warranted further

investigation of short scan times. With a shorter scan time, the thermal and fast neutron assay has a greater uncertainty. It was decided to perform 10 consecutive data captures with a short scan time (25 minutes) to observe the resulting spread of ANN estimates for $^{241}$AmBe (NPL reference 7245) at RLAT angle of incidence. The results can be seen in Table 8.2. Table 8.3 shows the averages of the thermal and fast neutron assays at each location within the water phantom for these repeated measurements at the short scan times. The uncertainties are calculated as standard uncertainties.

It can be seen that for a short scan time, the error ranges from 0.1% up to 27%, with a mean error of 14% for the fluence-dose conversion coefficient. This results in an mean error of 9% for the effective dose rate. The measured thermal to fast neutron ratios for these experimental data are shown for comparison in Table 8.2. A ratio of 3.03 was observed at the end of a 750 minute scan with the same experimental setup (as shown in Table 8.1). All ratios in Table 8.2 are greater than this ratio. This is thought to be due to an under estimate of the fast neutron content within the field. This suggests that the fast and thermal neutron assay algorithm error for short scan times, will have a tendency to result in an underestimate the effective dose. This hypothesis holds true for the data shown in Table 8.2.

Table 8.3: Averaged (a) thermal and (b) fast neutron assays at each location in the water phantom. These are from 10 consecutive experiments of a short total scan time of 25 minutes for the 25 locations. An $^{241}$AmBe source was located 248.5 cm from the centre of the phantom at an RLAT angle of incidence (row 5 in the table being closest to the source).

(a)

| | 1 | 2 | 3 | 4 | 5 |
|---|---|---|---|---|---|
| 1 | 349±25 | 515±32 | 650±33 | 801±33 | 778±37 |
| 2 | 443±25 | 652±21 | 882±30 | 1041±66 | 979±41 |
| 3 | 454±26 | 704±17 | 935±39 | 1140±27 | 1043±21 |
| 4 | 454±24 | 668±25 | 904±25 | 1082±24 | 1032±51 |
| 5 | 359±29 | 524±31 | 699±21 | 832±44 | 838±30 |

(b)

| | 1 | 2 | 3 | 4 | 5 |
|---|---|---|---|---|---|
| 1 | 17±12 | 114±24 | 153±3 | 236±10 | 323±11 |
| 2 | 19±13 | 121±9 | 181±9 | 243±8 | 341±12 |
| 3 | 37±19 | 110±20 | 156±6 | 244±6 | 323±8 |
| 4 | 40±14 | 99±23 | 171±11 | 232±10 | 354±7 |
| 5 | 7±7 | 84±23 | 162±20 | 241±9 | 314±8 |

### 8.4.4 Bidirectional field

With the network having been trained on single directions and isotropic fields, it was decided to see how the instrument performed with two sources located perpendicular to each other. A $^{241}$AmLi (NPL reference number 3250) was located AP to the detector at a distance of 144.7 cm. An $^{241}$AmBe source (NPL reference number 1152) was located RLAT to the detector at a distance of 195.8 cm. A scan was performed for 1000 minutes. The resulting distribution of thermal and fast neutrons in the water phantom can be seen in the heat plot shown in Figure 8.12. It is interesting to see the dominance of thermal neutrons suggests an AP source, whilst the fast neutron distribution suggests an RLAT source. The resulting ANN estimated fluence-to-dose conversion coefficient was 180 pSv cm$^2$ with an error of 6%, shown in Table 8.4. The dose rate was estimated by the ANN to be 0.93 $\mu$Sv/hr resulting in an error of 15% with the expected value.

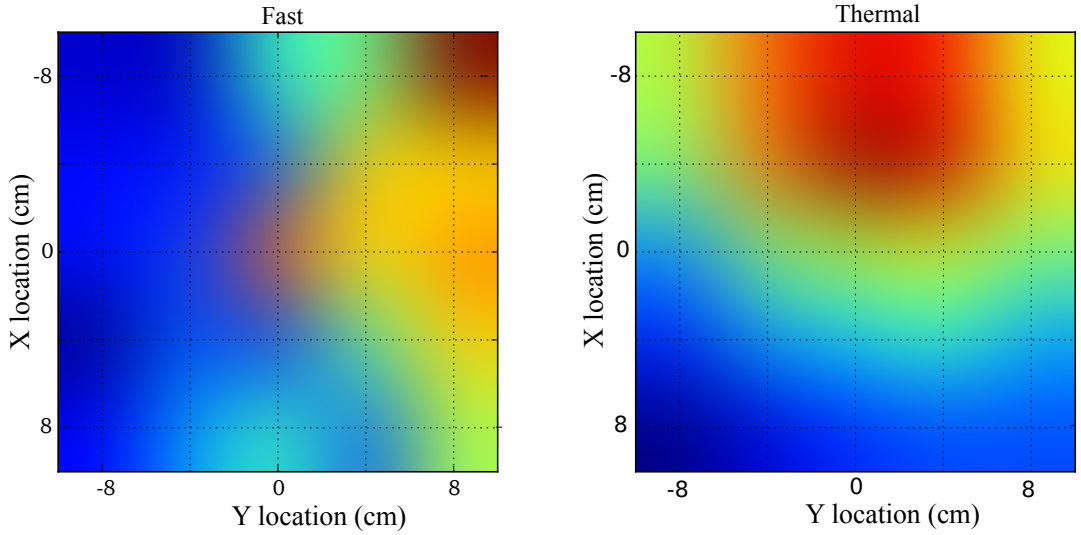


(a) (b)

Figure 8.12: Heat plot of the measured neutron distributions in the water phantom. For (a) fast neutrons (b) thermal neutrons. The dominance of $^{241}$AmBe (located RLAT) fast neutrons can be seen in the fast neutron plot. Likewise, the dominance of thermal neutrons from $^{241}$AmLi can be seen in the thermal neutron plot.

Table 8.4: Experimental results with bidirectional field.

| Neutron Source | Neutron field direction | Scan time [a] | Distance to phantom [b] | Fluence to E conversion coefficient (pSv cm$^2$) | | | E rate ($\mu$Sv/hr) | | |
|---|---|---|---|---|---|---|---|---|---|
| | | | | CMM | ANN | Error | CMM | ANN | Error |
| $^{241}$AmLi $^{241}$AmBe | AP RLAT | 1000 | 144.7 195.8 | 169±5 | 180 | 6% | 0.81±0.05 | 0.93 | 15% |

[a] time in minutes.
[b] distance to the geometric centre of the water phantom from the source (cm).

### 8.4.5 Shadow cone field

From the early investigation of this instrument it was known that testing it in a more complex field in terms of energy and direction would be required. However, the field in which the instrument was to be tested must also be understood to know the effective dose of that field. It was decided to synthesise a more complex field with a shadow cone. It was anticipated that this field would create a largely isotropic thermal field with a weak AP component of low angle scattered fast neutrons. A shadow cone (NPL serial number 7) was installed with the front face of the shadow cone 23 cm from the source. The shadow cone was 50 cm long, comprising iron (20 cm) and borated wax (30 cm). The narrow (iron) end had a diameter of 9 cm and the wide (wax) end a diameter of 17 cm, creating an apex angle of 4.57 degrees. The water phantom centre was 150 cm from the source, behind the shadow cone. The effective dose conversion coefficient was calculated to be 91±10 pSv cm$^2$. Results for two scans, one lasting 1250 minutes and one lasting 25 minutes, can be seen in Table 8.5. The ANN estimated coefficient based on the experimental measurements was 88 pSv cm$^2$ for a scan time of 1250 minutes. The neutron fluence rate in the detector was calculated based on the fraction of simulated neutrons reaching the detector multiplied by the source neutron emission rate. The resulting ANN effective dose rate was estimated to be 2.9 $\mu$Sv/hr with a calculated error of 36%. It can be seen that the shorter scan time of 25 minutes resulted in an error of 49% for the effective dose rate. However, further repeated measurements would be required to more fully understand the uncertainty of such a measurement for a short scan time.

Table 8.5: Experimental results with $^{252}$Cf behind a shadow cone.

| Neutron Source | Neutron field direction | Scan time [a] | Distance to phantom [b] | Fluence to E conversion coefficient (pSv cm$^2$) | | | E rate ($\mu$Sv/hr) | | |
|---|---|---|---|---|---|---|---|---|---|
| | | | | CMM | ANN | Error | CMM | ANN | Error |
| $^{252}$Cf | S/C[c] | 25 | 150.0 | 91±10 | 73 | 20% | 4.5±0.6 | 2.3 | 49% |
| | S/C | 1250 | 150.0 | | 88 | 3% | | 2.9 | 36% |

[a]time in minutes.
[b]distance to the geometric centre of the water phantom from the source (cm).
[c]source located AP to detector, behind shadow cone.

### 8.4.6 Ambient dose equivalent

The network architecture used for learning effective dose was retrained to learn ICRP74 ambient dose equivalent (*H*(10)*) fluence to dose conversion. This included the 10 parallel network architecture previously used, with the resulting output being the average of these 10 networks. The pattern and resulting output for this presents a different challenge for the ANN. Due to the anisotropic response of the instrument, an infinite number of inputs of the same single-direction field result in the same dose. The ANN must learn multiple patterns resulting in a single solution. ANN training was stopped when a total normalised mean squared error of 8x10$^{-5}$ was observed for the complete training set. The estimated conversion coefficient and dose rates are shown in Table 8.6. It can be seen that the ANN estimated the *H*(10)* with an error of 60% or less. The shadow cone and bidirectional fields, not found in the training data set, were estimated with an error of 31% or less. These preliminary results show promise, but further characterisation investigating the angular response of the instrument are required.

## 8.5 Conclusion

In this research a novel approach to neutron dosimetry has been proposed. Performing neutron assays at a number of locations with a $^6$Li-loaded scintillator detector in a water phantom, a pattern of thermal and fast neutron distributions was observed. An ANN was trained to learn simulated responses of the instrument in 10 different

Table 8.6: Experimental results for a network trained to learn ambient dose equivalent *H*(10)*. The ANN estimated Fluence to *H*(10)* conversion coefficient is shown, and the resulting *H*(10)* dose rate based on the number of detected neutron events within the water phantom. The headings labelled CAL are the expected values based upon calculations.

| Neutron Source | Neutron field direction | Scan time [a] | Distance to phantom [b] | Fluence to *H*(10)* conversion coefficient (pSv cm$^2$) | | | *H*(10)* rate ($\mu$Sv/hr) | | |
|---|---|---|---|---|---|---|---|---|---|
| | | | | CAL | ANN | Error | CAL | ANN | Error |
| $^{241}$AmBe | AP | 540 | 80.5 | 391 | 374 | 4% | 42±0.0 | 41 | 3% |
| | AP | 750 | 150.0 | 391 | 201 | 49% | 12±0.2 | 5 | 60% |
| | RLAT | 750 | 248.5 | 391 | 363 | 7% | 38±0.9 | 37 | 3% |
| $^{252}$Cf | AP | 750 | 80.5 | 383 | 363 | 5% | 21±0.3 | 17 | 17% |
| | AP | 9 | 80.5 | 383 | 310 | 19% | 21±0.3 | 27 | 28% |
| | AP | 90 | 80.5 | 383 | 351 | 8% | 20±0.3 | 21 | 2% |
| | 45° | 750 | 80.5 | 383 | 326 | 15% | 17±0.3 | 13 | 24% |
| | AP | 285 | 80.5 | 383 | 356 | 7% | 20±0.3 | 19 | 7% |
| $^{241}$AmLi | AP | 1250 | 150.0 | 245 | 223 | 9% | 0.7±0.0 | 0.7 | 0% |
| | RLAT | 1250 | 175.7 | 245 | 211 | 14% | 0.5±0.0 | 0.5 | 8% |
| $^{252}$Cf | S/C [c] | 25 | 150.0 | 223 | 241 | 8% | 11±0.2 | 8 | 31% |
| | S/C | 1250 | 150.0 | 223 | 263 | 18% | 11±0.2 | 9 | 22% |
| $^{241}$AmLi $^{241}$AmBe | AP RLAT | 1000 | 144.7 195.8 | 297 | 246 | 17% | 1.4 | 1.3 | 10% |

[a] time in minutes.
[b] distance to the geometric centre of the water phantom from the source (cm).
[c] source located AP to detector, behind shadow cone.

computer simulated fields, each from 9 different directions. The instrument was then experimentally tested in a number of different radiation fields and the effective dose and *H*(10)* doses were estimated. When a scan time of greater than 90 minutes was performed, the largest resulting effective dose rate error was found to be 45% and 60% for *H*(10)*. It should be emphasised, however, that the training data were based purely on computer simulated results. It is thought that the instrument could be improved with more complex directional fields in training.

This proof-of-concept instrument has shown promise in the experimental testing thus far. However, a significant step forward with this instrument would be the addition of z axis measurements to resolve top and bottom angles of the neutron field. However, this requires considerably more simulations and the ANN would

require re-training. Further experimental testing of the instrument in more thermal fields would also beneficial. However, to estimate the effective dose of a neutron field, complex room geometries must be modelled and experimentally verified to gain confidence in the effective dose calculations. Therefore this further testing would need to take place in a facility where this confidence could be gained.

A new set of conversion coefficients were published in ICRP116. Consequently, given that the instrument presented in this research performs the processing within software, changing to ICRP116 recommendations would in theory be a simple software change with no further experimental response characterisations required. However, the same problem with only a limited number of published field directions exists. A complete re-validation of the CMM phantom would be required to obtain ICRP116 based fluence to effective dose conversion coefficients.

It should be noted that the water phantom was investigated for the ease of use in an experimental prototype. However, it is envisaged that a more practical instrument could be realised with polyethylene and multiple compact detectors embedded within a polyethylene cylinder or sphere. A silicon photomultiplier tube coupled to this detector could provide such a compact detector. Using more than one detector would have the benefit of a reduced scan time. A final point, worthy of further future investigation, given that the detector is sensitive to gamma radiation as well as neutron radiation, it is possible that this instrument could be used for gamma dosimetry as well.

## 8.6 Acknowledgements

The authors would like to express thanks to Natalia Zaitseva and the team at LLNL for providing the scintillator. The authors would like to acknowledge the funding support from EPSRC and the National Physical Laboratory, Teddington, UK. The authors would also like to acknowledge the help and advice of Dr. Nigel Hawkes at the National Physical Laboratory. The authors acknowledge the use of the package Matplotlib for all plots in this research [129]. The data generated in this work are available from the Lancaster University data archive [143].

# Chapter 9

# Discussion and conclusion

## 9.1 Summary

In this thesis a novel neutron survey meter has been designed, built and tested which takes account of both neutron energy and direction, to estimate effective dose. It is believed that in this research, for the first time, a single instrument at a single location has been used to estimate the effective dose of a neutron field.

At the beginning of this project, a number of existing neutron dosimetry techniques and their suitability for use in a directional neutron dose meter has been reviewed. The portability and real-time measurement capability of these instruments was also reviewed. Two promising instruments for directional neutron dosimetry were identified; a spectrometer developed by Physikalisch-Technische Bundesanstalt (PTB) and a theoretical design for an instrument proposed by the National Physical Laboratory (NPL) [13, 84]. Some preliminary computer modelling was performed to characterise these instruments. These models were also used to assess their suitability for portable applications. For optimal results with the PTB instrument, prior information on the energy spectrum under investigation was required to aid the unfolding process [11]. The NPL instrument design exploited the distribution of thermal neutron capture locations in a single loaded scintillator to estimate effective dose using an ANN. However, with the NPL design, no method was identified to localise neutron capture in the scintillator [84]. The NPL instrument was deemed worthy of further investigation for directional dosimetry.

In this research, the first investigation in the design of the instrument was to

identify a suitable loaded scintillator. The scintillator needed to be efficient at detecting thermal neutrons and the detected signal arising from capture needed to be correlated to the location of capture. Gd, $^{6}$Li and $^{10}$B loaded liquid scintillators were all considered as worthy candidates. Two computer modelling codes (Geant4 and MCNP) were used to investigate these scintillators. A comparison of these two computer codes for thermal neutron detector modelling was undertaken, a good agreement was observed. With no associated gamma emission from neutron capture, $^{6}$Li was found to be the most attractive of the scintillator loadings investigated in the simulations.

Simulation-based research was completed to see if the effective dose of a neutron field could be estimated based upon the pulse height spectra from a number of neutron captures in a scintillator. The theoretical results in chapter 5 showed promise, however, a key development area still required further study. The methodology required a scintillator that was only sensitive to thermal neutrons, or a signal processing method that could enable detection of thermal neutron capture based on a fraction of the collected light. It was proposed that capture gated neutron detection could be a suitable technique to meet this detection requirement. However, further experimental work described in chapter 6 showed that this technique did not boast any degree of efficiency with a $^{6}$Li-loaded plastic scintillator.

However, an outcome from this research in chapter 6 was the development of a novel technique to perform simultaneous thermal and fast neutron assays using the $^{6}$Li-loaded plastic scintillator system. Using this signal processing technique, a $^{6}$Li-loaded plastic scintillator based detector system performed neutron assays at a number of locations in a water phantom. The instrument response was modelled using MCNP and an ANN was trained to learn these responses. Experimental results of neutron assays at 25 locations in a 20x20x17.5 cm$^3$ water phantom were fed into the trained ANN. The resulting output was a fluence to effective dose conversion coefficient for the assayed field. A correlation between neutron fluence rate in the phantom and source fluence rate was experimentally found. The resulting estimates of effective dose rate had an error of 45% or less, regardless of energy distribution or direction. The ANN was also trained to learn ambient dose equivalent and the resulting ambient dose equivalent rate for the experimental results was found to be 60% or less for the 14 experimental fields investigated.

## 9.2 Outlook

Existing neutron area survey meters measure ambient dose equivalent *H*(10)*. However, this conservative estimate of the health risk to a human does not account for the direction of the neutron field. The instrument in this research has estimated the effective dose of a number of neutron fields. The directional dosimetry quantity of Hp(10,$\theta$) is perhaps more suitable than effective dose for directional neutron dosimetry, as it is an operational quantity [30]. However, no values beyond 75° are published. So in the absence of a more suitable directional area dosimetry quantity, effective dose has been used to investigate the potential of this instrument. A limitation of a number of existing neutron area survey meters is that their response is constrained by the hardware. This is not the case with this instrument, as its dose response is mostly in software. Indeed, if in the future new directional dosimetry standards are published, these could be evaluated for use with this instrument.

From a radiation protection viewpoint, the conservative nature of non-directional dosimetry standards is entirely valid. However, it can be useful to know the effective dose of a neutron field when evaluating the impact of operational instruments (such as an area survey meter measuring *H*(10)*). Their non-ideal anisotropic response means that there is a potential for under or over reading of some directional fields [76]. Furthermore, when evaluating personal dosemeters, their response is directional due to the proximity to the human body acting as a neutron moderator. The instrument developed in this research is a useful tool for understanding some of these existing instrument responses. That is, for directional fields, how well the operational quantities estimate the protection quantities.

A number cancer treatments require neutron dosimetry within the medical facilities. In these facilities in the UK, to comply with the Ionising Radiations Regulations 1999, the ionising radiations must be monitored. This instrument could be used to meet these operational dosimetry requirements. This instrument could also be used to aid the commissioning of facilities. The instrument provides a heat map which can be used to infer if there is a strong directional component in these neutron fields. With this information the suitability of neutron shielding in a facility could be appraised. This same feature could also be exploited to examine neutron dose for workers in a facility. For example, if a worker always sits in a fixed orientation

operating a machine, the directional dose experienced in this orientation could be estimated. Such studies are presently only possible with computer modelling. Further studies such as those discussed above using this instrument can only improve understanding of the health risk associated with exposure to neutrons.

## 9.3 Future work

The instrument reported on in this thesis has shown promise in the experimental testing already performed. However, there are a number of recommendations for future work which would be of benefit to this instrument.

### 9.3.1 Changes to the instrument design

The proof-of-concept instrument built in this research performed neutron assay at 25 different locations in a fixed horizontal plane, at the mid-height of the water phantom. Preliminary modelling of a neutron source located above and below the water phantom suggests that the ANN would benefit significantly from being able to perform measurements throughout the whole volume of the water phantom. Maintaining the same grid pattern over the whole phantom would result in 125 (5x5x5) assay locations. This high number of assay locations would significantly impede the usage of the instrument, requiring potentially a week to perform a whole scan.

With more than one detector located within the water phantom, the scan time could be reduced. In this instrument, if 25 detectors were placed in the water phantom at the horizontal scan locations, the 25 detector array could be moved up and down the 5 vertical scan segments of the phantom. However, the wiring and electronics associated with such a scheme would prove challenging for a portable design.

With these additional detectors all located in the water, the resulting change in response of the thermal and fast neutron distributions with the larger content of $^{6}$Li within the volume of water would need to be investigated.

A more practical design consideration is one which moves away from a liquid based neutron moderator (such as water in this case). In doing so, the portabil-

ity and ease of set-up of the instrument becomes more interesting. However, the movement of the detector within the volume of the moderator becomes a new challenge. A possible solution is in the form of a number of rotating, offset cylinders, with detectors embedded in these cylinders. Figure 9.1 shows a detector (red disc) offset within a rotating cylinder (rotating about the axes b). Installing this offset, in another rotating cylinder (rotating about the axes a), a number of detector scan locations can be achieved. This is analogous to a moon (the detector) rotating about a planet which rotates about the sun. This would enable a number of locations to be assayed within the moderating phantom. Furthermore, by placing a detector in the centre of this (on axis a), the central detector could be configured to provide an ambient dose equivalent estimate.

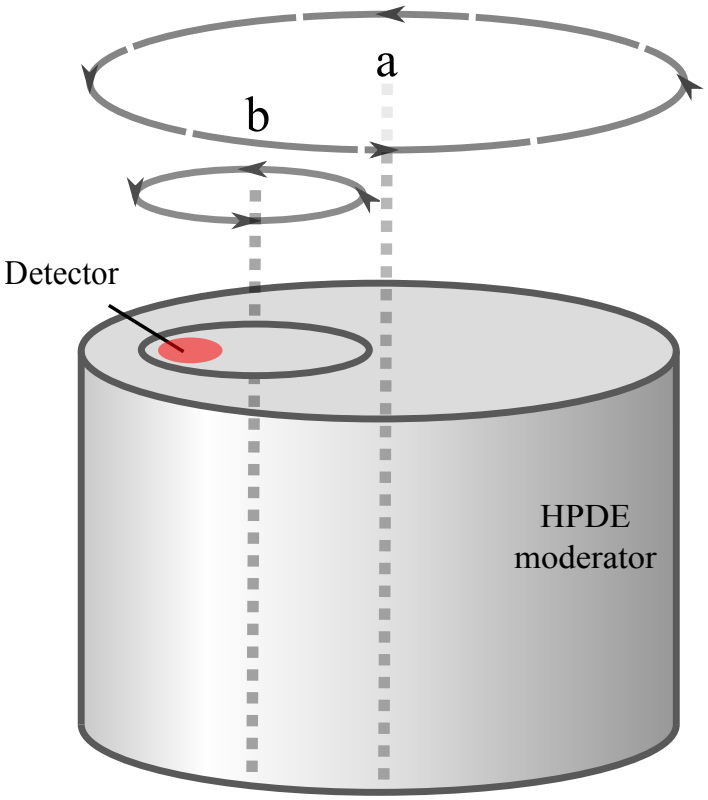


Figure 9.1: An example of an offset rotating cylinder with a detector embedded within this. This would enable a HPDE based moderator to be used and improved the portability and ease of setup of the instrument.

### 9.3.2 Neutron fluence rate estimation

The method for estimating the neutron fluence rate in the detector is a major area which could benefit from improvement in this instrument. The current method of finding a biased sum of thermal and fast neutrons is anticipated to be a function of neutron energy. In this work only $^{241}$AmBe, $^{241}$AmLi and $^{252}$Cf radionuclide source were used for the neutron fluence rate estimation. Further characterisation with more thermal fields would be advantageous to investigate this relationship. The most thermal of the three sources used, $^{241}$AmLi, had a comparatively low neutron emission rate. Performing longer scans or using a more active source would be advantageous. Indeed, if the thermal fluence rate estimation is found to be a function of neutron energy, the ANN estimation of the fluence to effective dose conversion coefficient could likely be used to aid this estimation.

### 9.3.3 Neutron detector

The $^{6}$Li-loaded plastic scintillator used in this work performed well. However, a number of improvements could be made to the detector. The current state of research of lithium containing plastic scintillators is such that 0.4% weight loadings of $^{6}$Li can now be achieved, compared to the 0.14% of $^{6}$Li in this work [148]. This would likely result in shorter scan times for the same number of detected thermal neutrons.

Other scintillators for combined thermal and fast neutron detection such as $Cs_2LiYCl_6$:Ce (CLYC) and $^{10}$B-loaded plastic scintillators should also be evaluated against the $^{6}$Li used in this work [21, 87]. The technique for thermal neutron assay in this work appears to be suitable for use with these scintillators. In the case of $^{10}$B-loaded plastic scintillators (thermal capture cross-section of 3837 barns) it is anticipated a much greater thermal neutron detection efficiency would be observed compared to $^{6}$Li (thermal capture cross-section of 940 barns). However, further experimental work would be required to characterise this.

For multiple detectors within a single neutron moderator, there is a motivation to reduce the size of the detector system. Silicon photomultipliers (SiPm) are an emerging technology with suitability for this. Further work could look to investigate

the performance of a SiPm based detector system. Currently, it is not clear if the SiPm detectors presently on the market would provide adequate PSD performance when coupled to the plastic scintillator used in this work [149, 150, 151].

### 9.3.4 Pulse processing electronics

The FPGA based pulse processing system used in this work has a number of limitations. One of the primary constraints is the data throughput of the USB to PC communications link. Due to the prototype nature of the instrument and algorithms, the FPGA was programmed to send raw pulse information, so that the PSD method could be decided in post processing. Following the experimental work described in chapter 6, the charge comparison method was selected for use with this instrument. It is envisaged that this algorithm could be programmed to be performed within the FPGA.

In the UART configuration implemented in the FPGA, for every detected pulse, the total number of bits sent was 1620 (30 ADC samples, where each sample was 6 ASCII characters, and each ASCII character was 9 bits). This limited reliable operation of the FPGA to around 5000 triggered events per second. Encoding the numbers in hexadecimal and sending just the long and short integral (from the charge comparison method of PSD) for each pulse could reduce this to 90 bits per pulse. In real terms, with the 8 Mbit UART used in this instrument, this would increase the data throughput to nearly 89,000 triggered events per second. Furthermore, moving to an FPGA based system with an ARM processor embedded within the system would increase options for data transfer between the FPGA and processor. Speeds of up to 1 GB/s could likely be achieved even over long length transmission lines.

A second limitation of the FPGA based system is the relatively low ADC sample rate of 150 MS/s. Current ADC technology allows potentially 3 GS/s ADC operation, however, at these higher count rates a reduced resolution is the usual trade off. Repeating the comparative analysis of PSD methods in this work for a number of different samples rates and ADC resolutions would likely give further insight into this.

### 9.3.5 Directional dosimetry

The instrument built in this research could be trained to learn other directional dose coefficients, such as personal dose equivalent. Furthermore, as these response functions lie in software, the instrument can easily simultaneously estimate personal dose equivalent, ambient dose equivalent and effective dose at the same time.

Effective dose is a risk estimation which is not tailored for individual humans. However, with this instrument, with further human phantom modelling there is potential to provide unique dose estimates for individuals. Although, the instrument would only be beneficial in this application if it could learn to estimate effective dose with an uncertainty less than the difference between the different sexes/sizes/ages of a modelled human. The author is not aware of any published work detailing the variance of a directional dose quantity with different ages/sexes/human body dimensions. This non-trivial study would likely become a whole topic of postgraduate research in its own right.

### 9.3.6 Gamma dosimetry

An unexplored area of research with this instrument is the potential to utilise the distribution of gamma radiation in the water phantom to perform directional gamma dosimetry. Currently, using pulse shape discrimination the gamma events are rejected.

However, it is anticipated a pattern relating to energy and direction could be observed by recording the gamma detections. A preliminary experimental measurement was performed. A $^{252}$Cf source was located AP to the detector and then moved to be 45° (midpoint of AP-RLAT) to the detector. The results can be seen in Figure 9.2. The distribution of gamma detections in the water phantom suggests that a directional component of the gamma field can be inferred. The preliminary results suggest that there may be some merit in investigating the gamma distributions.

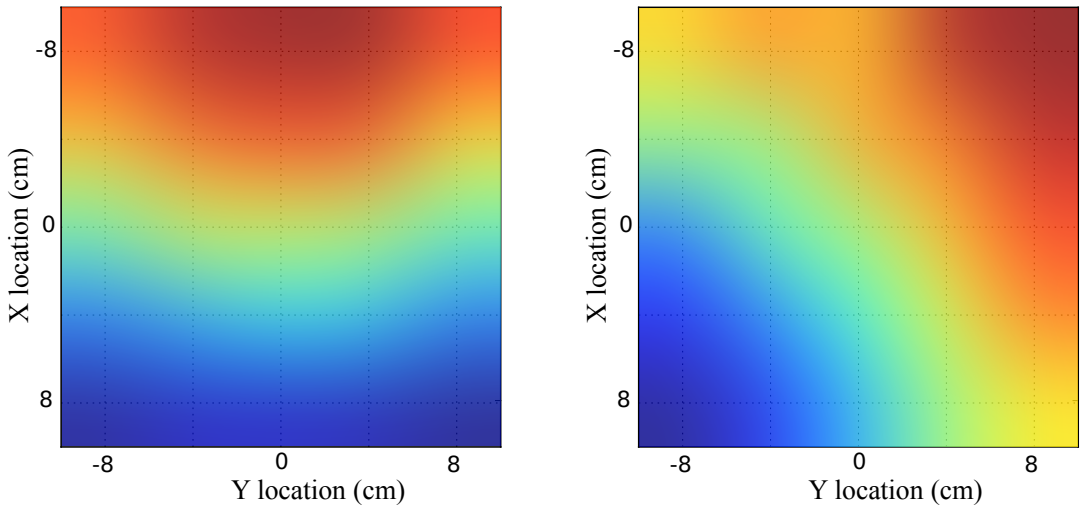


Figure 9.2: Gamma assays were performed at 25 locations in the water phantom. This method is further discussed in chapter 8. The GMM algorithm (described in chapter 7) was used to perform the assays. The heat plot shows measured gamma distributions in the water phantom. For $^{252}$Cf (a) AP (b) midpoint of AP-RLAT.

### 9.3.7 Further instrument testing

Further experimental testing of this instrument would be beneficial to understand further the ANN and the suitability of its training set. In particular higher and lower energy neutron fields beyond those tested in this research.

The instrument would benefit from further testing in neutron workplace fields. To assess the accuracy of the instrument in these environments, an effective dose must be calculated. This would require full Monte Carlo based modelling of the workplace, including the human phantom (as described in chapter 8). To gain confidence in these models, experimental measurements should be performed. This experimental based testing necessitates accounting for complex room scatter and accurate spectroscopy. This would likely result in a complex Bonner sphere measurement campaign being performed. Hence, performing these tests in a true workplace environment is a non-trivial task. However, it would be of great interest, with this experimental workplace testing, to examine the performance of the instrument

in the presence of a strong gamma field, which would likely co-exist with a neutron workplace field.

The *H*(10)* experimental tests performed in this work would benefit from further investigation. Namely, a primary focus should be to perform more directional tests to ensure an isotropic response output from the ANN. These tests could be performed over the $4\pi$ region of the detector for a number of different neutron spectra to understand the magnitude of the anisotropy of the ANN response.

### 9.3.8 Security applications

Two or more of the instruments developed in this work could be configured to provide their assays to a central processing unit. Using machine learning methods similar to the ones used in this research, it may then be possible to infer the location of a neutron source. This would then make the system interesting for security applications monitoring the illicit movement of neutron emitting radionuclide sources. However, a significant amount of further work would be required to characterise this instruments suitability for security applications and the detection of special nuclear materials. Primarily, if these materials can be detected without requiring a 12 hour long scan.

# Appendix A

## Calculating effective dose - a worked example

In this research a number of neutron dosimetry calculations have been performed. A worked example is described in this appendix for the neutron field shown in Figure A1.

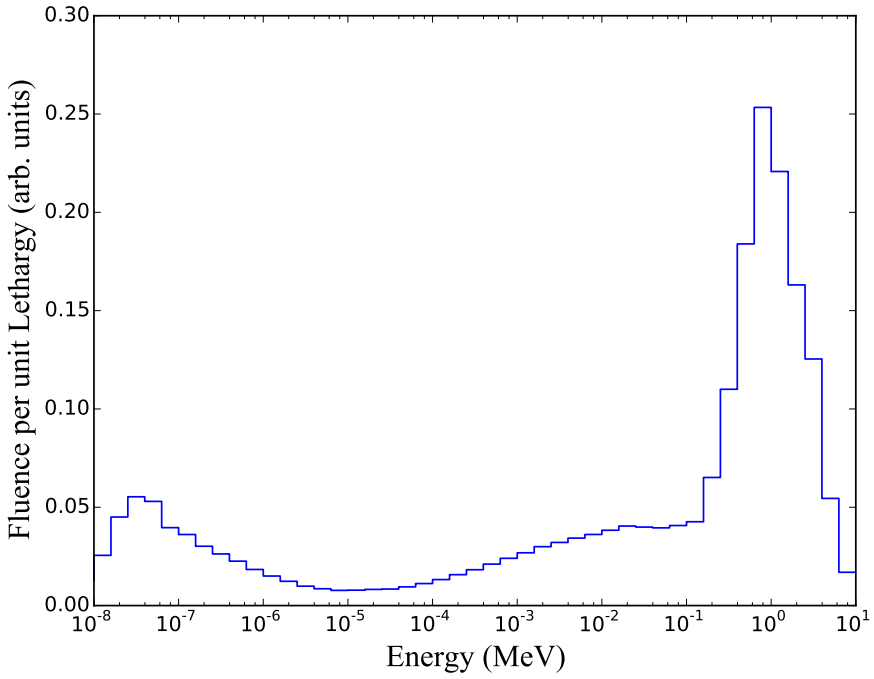


Figure A1: An example neutron spectrum.

The neutron fluences used to generate this plot are shown in Table A1. In this

worked example, the AP effective dose is calculated using ICRP74 AP fluence to effective dose conversion coefficients [30], these are shown in Table A2.

For each energy bin, the mean energy was found using the python code snippet shown below;

```
meanEnergy = exp((log(nEnergy[i+1]) + log(nEnergy[i]))/2)
```

The mean energy of each bin is used to interpolate the fluence to effective dose conversion curve to find the corresponding coefficient for the mean energy shown in the code snippet below;

```
from scipy import interpolate


def calcED(array, value, energyBins):
  x = energyBins
  y = array
  f = interpolate.interp1d(x, y)
  return f(value)
```

The resulting mean energy and interpolated fluence to effective dose conversion coefficient are multiplied by the fluence to find the resulting effective dose for that energy region. This process is repeated for all energy bins in the data.

```
nEffectiveDose[i] = (calcED(coef, meanEnergy, energyBins)) * nFluence[i]
```

In this example, the resulting effective dose has been calculated as 180.3 pSv $cm^2$.

# Appendix A

Table A1: Energy fluence values used to produce the neutron spectrum shown in Figure A1.

| Energy (eV) | Fluence | Energy (eV) | Fluence |
|---|---|---|---|
| 7.94E-04 | 9.30E-05 | 1.26E+02 | 6.11E-03 |
| 1.26E-03 | 2.25E-04 | 2.00E+02 | 7.19E-03 |
| 2.00E-03 | 5.36E-04 | 3.16E+02 | 8.40E-03 |
| 3.16E-03 | 1.25E-03 | 5.01E+02 | 9.71E-03 |
| 5.01E-03 | 2.81E-03 | 7.94E+02 | 1.11E-02 |
| 7.94E-03 | 5.99E-03 | 1.26E+03 | 1.24E-02 |
| 1.26E-02 | 1.18E-02 | 2.00E+03 | 1.37E-02 |
| 2.00E-02 | 2.06E-02 | 3.16E+03 | 1.48E-02 |
| 3.16E-02 | 2.55E-02 | 5.01E+03 | 1.58E-02 |
| 5.01E-02 | 2.44E-02 | 7.94E+03 | 1.67E-02 |
| 7.94E-02 | 1.83E-02 | 1.26E+04 | 1.77E-02 |
| 1.26E-01 | 1.67E-02 | 2.00E+04 | 1.85E-02 |
| 2.00E-01 | 1.38E-02 | 3.16E+04 | 1.84E-02 |
| 3.16E-01 | 1.21E-02 | 5.01E+04 | 1.82E-02 |
| 5.01E-01 | 1.04E-02 | 7.94E+04 | 1.88E-02 |
| 7.94E-01 | 8.48E-03 | 1.26E+05 | 1.97E-02 |
| 1.26E+00 | 6.94E-03 | 2.00E+05 | 2.98E-02 |
| 2.00E+00 | 5.65E-03 | 3.16E+05 | 5.07E-02 |
| 3.16E+00 | 4.55E-03 | 5.01E+05 | 8.47E-02 |
| 5.01E+00 | 3.94E-03 | 7.94E+05 | 1.17E-01 |
| 7.94E+00 | 3.57E-03 | 1.26E+06 | 1.02E-01 |
| 1.26E+01 | 3.62E-03 | 2.00E+06 | 7.46E-02 |
| 2.00E+01 | 3.76E-03 | 3.16E+06 | 5.78E-02 |
| 3.16E+01 | 3.87E-03 | 5.01E+06 | 2.51E-02 |
| 5.01E+01 | 4.38E-03 | 7.94E+06 | 7.82E-03 |
| 7.94E+01 | 5.17E-03 | 1.26E+07 | 4.28E-03 |

Appendix A

Table A2: ICRP74 AP fluence to effective dose conversion coefficients [30].

| Energy (eV) | Fluence | Energy (eV) | Fluence |
|---|---|---|---|
| 1.00E-003 | 5.24 | 5.00E+005 | 188 |
| 1.00E-002 | 6.55 | 7.00E+005 | 231 |
| 2.50E-002 | 7.6 | 9.00E+005 | 267 |
| 1.00E-001 | 9.95 | 1.00E+006 | 282 |
| 2.00E-001 | 11.2 | 1.20E+006 | 310 |
| 5.00E-001 | 12.8 | 2.00E+006 | 383 |
| 1.00E+000 | 13.8 | 3.00E+006 | 432 |
| 2.00E+000 | 14.5 | 4.00E+006 | 458 |
| 5.00E+000 | 15 | 5.00E+006 | 474 |
| 1.00E+001 | 15.1 | 6.00E+006 | 483 |
| 2.00E+001 | 15.1 | 7.00E+006 | 490 |
| 5.00E+001 | 14.8 | 8.00E+006 | 494 |
| 1.00E+002 | 14.6 | 9.00E+006 | 497 |
| 2.00E+002 | 14.4 | 1.00E+007 | 499 |
| 5.00E+002 | 14.2 | 1.20E+007 | 499 |
| 1.00E+003 | 14.2 | 1.40E+007 | 496 |
| 2.00E+003 | 14.4 | 1.50E+007 | 494 |
| 5.00E+003 | 15.7 | 1.60E+007 | 491 |
| 1.00E+004 | 18.3 | 1.80E+007 | 486 |
| 2.00E+004 | 23.8 | 2.00E+007 | 480 |
| 3.00E+004 | 29 | 3.00E+007 | 458 |
| 5.00E+004 | 38.5 | 5.00E+007 | 437 |
| 7.00E+004 | 47.2 | 7.50E+007 | 429 |
| 1.00E+005 | 59.8 | 1.00E+008 | 429 |
| 1.50E+005 | 80.2 | 1.30E+008 | 432 |
| 2.00E+005 | 99 | 1.50E+008 | 438 |
| 3.00E+005 | 133 | 1.80E+008 | 445 |

# Appendix B

## FPGA based pulse processing system

In this research a bespoke FPGA based pulse processing system has been developed. This is described in chapter 7. Some further background details on the system are provided in this appendix.

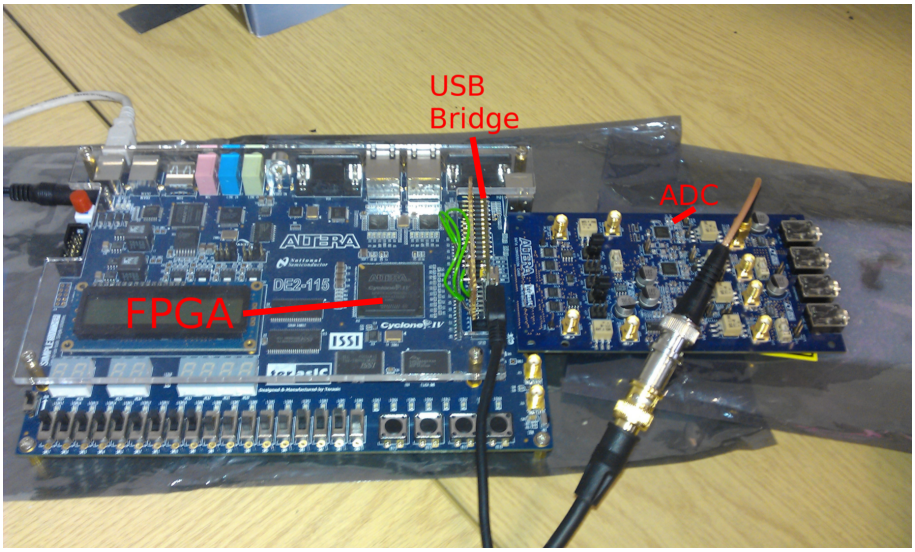


Figure B1: Bespoke FPGA based pulse processing system developed during this research.

The Altera DE2-115 development board was selected for prototype development [152]. The development board and ADC card are shown in Figure B1. This development board contains a number of communications options for transferring the digitised pulses to a PC. Proof-of-concept prototypes were created using Eth-

ernet, and on board USB communications. The USB did not allow a high enough data transfer speed. A UDP packet offload based prototype was developed in VHDL code, however, no reliable method was established using UDP offload.

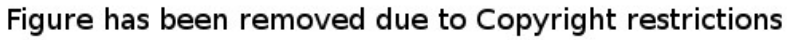


Figure B2: FTDI UM232H development board [153].

Due to time constraints, it was decided to use an FTDI UM232H development board, as shown in Figure B2 [153]. This allowed 8 MBit per second transfer rates using a simple UART within the FPGA. The USB link emulates as a standard PC serial port within Linux/Windows operating systems. This allows for simple data logging without writing specialist bespoke software.

The PMT signal was connected to an Analog Devices AD9254 150 mega-samples-per-second (MS/s), 14 bit analogue-to-digital converter (ADC) [154]. The data were clocked from the ADC with a clock generated within the FPGA. At higher sample rates an external clock would be required.

For development purposes, a digital-to-analogue converter (DAC) was used to generate 200 ns long scintillation type pulses. This was triggered to send pulses at a rate of 200 Hz for initial investigations. This has proved invaluable during the testing of the system. The output of the DAC was fed through a 50 Ω impedance matching transformer.

This connected through a small coaxial patch lead to the input transformer on the ADC circuitry. However, in initial testing it was found that ADC input transformer was configured, such that there was an impedance mismatch between the PMT and the transformer. This resulted in reflections which can be seen in Figure B3 displayed on a 2 GHz oscilloscope.

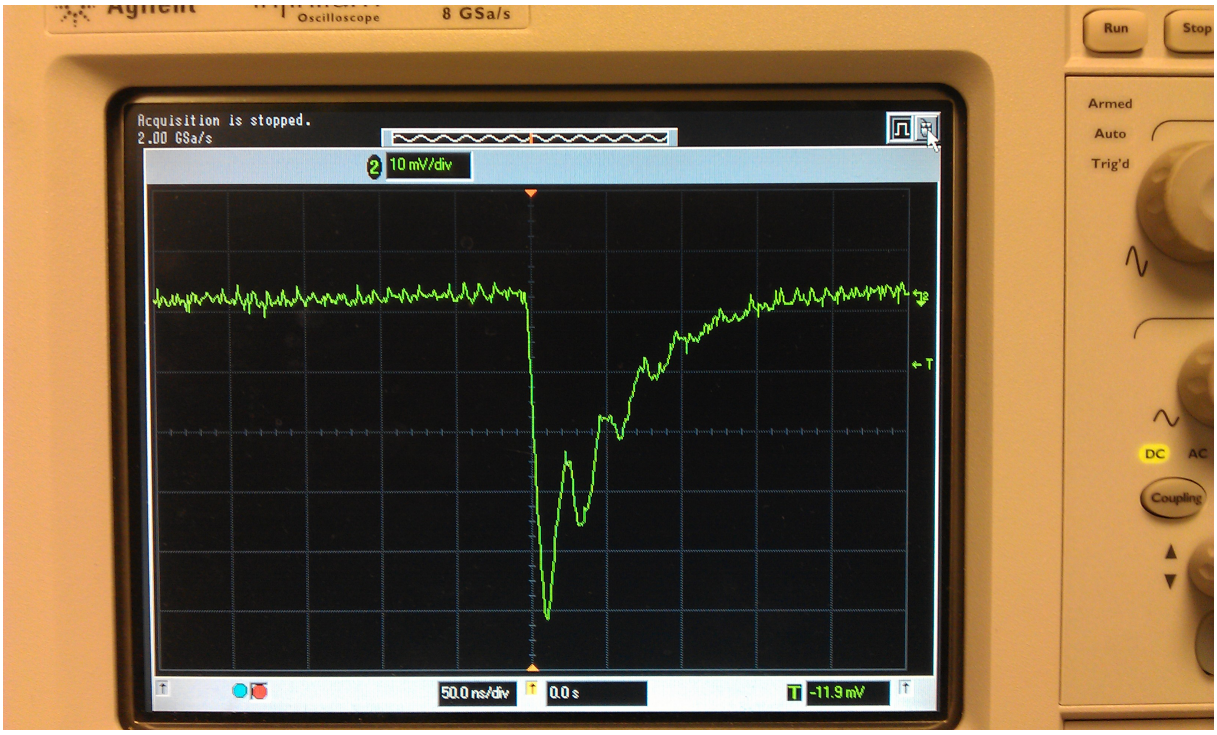


Figure B3: Measured background radiation pulses. Degradation of the pulse shapes occurred due to an impedance mismatch between the PMT anode and ADC input transformer.

Further inspection of the ADC board schematic and the board itself revealed some configuration changes were needed to be made, this can be seen in Figure B4. R117 was removed and installed at the location of R116. These resistor locations are shown in Figure B5.

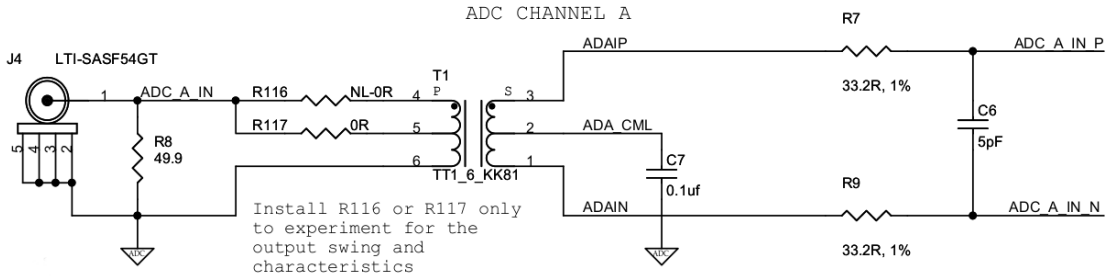


Figure B4: Portion of the schematic of the ADC card used [154].

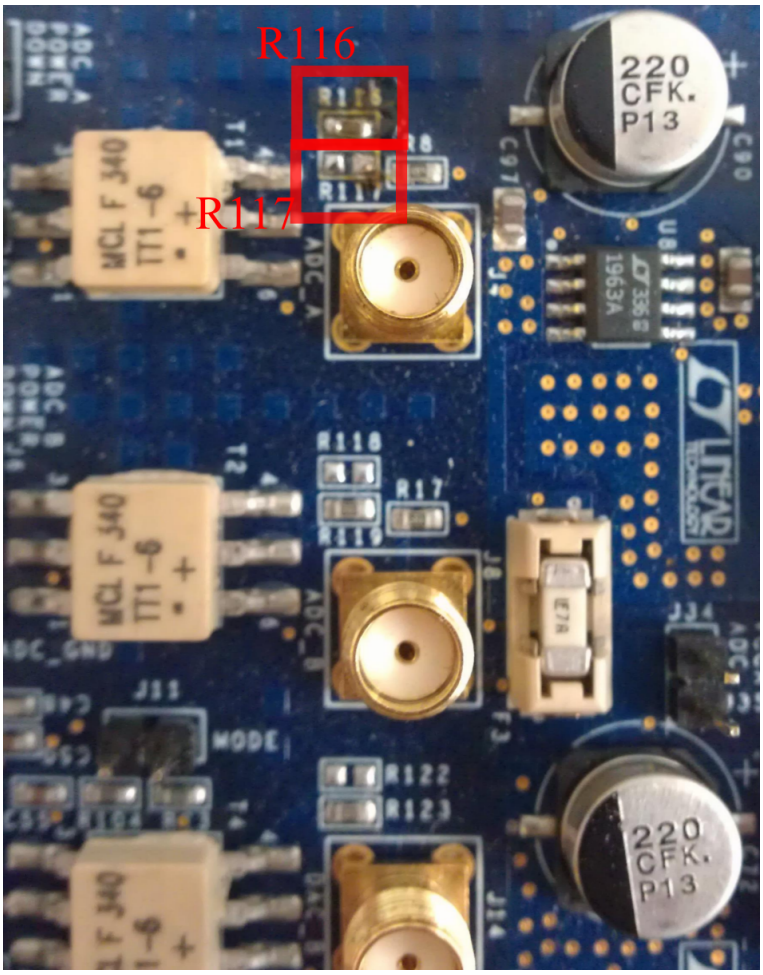


Figure B5: Location of the two resistors which required changing.

Following these changes, the pulse shapes were observed to have no problems with reflections due to impedance mismatch.

# Glossary

| | |
|---|---|
| ADC | Analogue-to-digital converter |
| ANN | Artificial neural network |
| AP | Antero-posterior |
| BSS | Bonner Sphere Spectrometer |
| DAC | Digital-to-analogue converter |
| E | Effective dose |
| FFT | Fast Fourier transform |
| FIR | Finite impulse response |
| FIFO | First in first out |
| FOM | Figure of merit |
| FPGA | Field-programmable gate array |
| FWHM | Full Width at Half Maximum |
| GMM | Gaussian mixtures model |
| H*10 | Ambient dose equivalent |
| ICRP | International Commission on Radiological Protection |
| ICRU | International Commission on Radiation Units and Measurements |
| ISO | Isotropic |
| LLAT | Left-lateral |
| PA | Postero-anterior |
| PC | Personal computer |
| PMT | Photomultiplier Tube |
| PSD | Pulse shape discrimination |
| PTRAC | Particle tracking file |
| RLAT | Right-lateral |
| ROT | Rotational |
| SiPM | Silicon Photomultiplier |
| UART | Universal asynchronous receiver/transmitter |
| UDP | User Datagram Protocol |
| USB | Universal Serial Bus |

# References


[1] Nuclear power in the united kingdom. http://www.world-nuclear.org/info/Country-Profiles/Countries-T-Z/United-Kingdom/. Accessed: 2016-01-05. 1

[2] Nuclear power: Hinkley point. https://www.gov.uk/government/collections/hinkley-point. Accessed: 2016-01-05. 1

[3] Nuclear generation by country. http://www.world-nuclear.org/info/Facts-and-Figures/Nuclear-generation-by-country/. Accessed: 2016-01-05. 1

[4] The ionising radiations regulations 1999. http://www.legislation.gov.uk/uksi/1999/3232/contents/made. Accessed: 2016-01-05. 1

[5] S. Nagataki, N. Takamura, K. Kamiya, and M. Akashi. Measurements of Individual Radiation Doses in Residents Living Around the Fukushima Nuclear Power Plant. *Radiation Research*, 180(5):439–447, November 2013. 2

[6] Proton beam therapy - the christie. http://www.christie.nhs.uk/our-future/our-developments/protons.aspx. Accessed: 2016-01-05. 2

[7] Secondary neutrons in proton and ion therapy. http://www.melodi-online.eu/doc/Stolarczyk_Secondary%20neutrons%20in%20proton%20and%20ion%20therapy.pdf. Accessed: 2016-01-05. 2

[8] R.J. Tanner, C. Molinos, N.J. Roberts, D.T. Bartlett, L.G. Hager, G.C. Taylor, and D.J. Thomas. Practical implications of neutron survey instrument

performance. Technical Report HPA-RPD-016, Health Protection Agency, Chilton, UK, 2006. 3, 22, 38, 39

[9] D.J. Thomas and A.V. Alevra. Bonner sphere spectrometers–a critical review. *Nuclear Instruments and Methods in Physics Research Section A: Accelerators, Spectrometers, Detectors and Associated Equipment*, 476(1–2):12–20, January 2002. 3, 25, 39

[10] H. Schuhmacher. Workplace monitoring of mixed neutron-photon radiation fields and its contribution to external dosimetry. *Radiation Protection Dosimetry*, 144(1–4):599–604, February 2011. 3

[11] F. d'Errico, D. Bartlett, T. Bolognese-Milsztajn, M. Boschung, M. Coeck, G. Curzio, A. Fiechtner, J.-E. Kyllönen, V. Lacoste, L. Lindborg, M. Luszik-Bhadra, M. Reginatto, H. Schuhmacher, R. Tanner, and F. Vanhavere. Evaluation of individual dosimetry in mixed neutron and photon radiation fields (EVIDOS). Part I: Scope and methods of the project. *Radiation Protection Dosimetry*, 125(1-4):275–280, July 2007. 3, 41, 42, 150

[12] F. d'Errico, V. Giusti, M. Reginatto, and B. Wiegel. A telescope-design directional neutron spectrometer. *Radiation Protection Dosimetry*, 110(1-4):533–537, September 2004. 3, 39, 41

[13] M. Luszik-Bhadra, F. d'Errico, O. Hecker, and M. Matzke. A wide-range direction neutron spectrometer. *Nuclear Instruments and Methods in Physics Research Section A: Accelerators, Spectrometers, Detectors and Associated Equipment*, 476(1):291–297, January 2002. xiii, 3, 24, 39, 40, 150

[14] R.J. Tanner, J.S. Eakins, and L.G. Hager. A new design of neutron survey instrument. *Radiation Measurements*, 45(10):1585–1588, December 2010. 3

[15] J.W. Leake. An improved spherical dose equivalent neutron detector. *Nuclear Instruments and Methods*, 63(3):329–332, 1968. 3

[16] The helium-3 shortage: Supply, demand, and options for congress. https://www.fas.org/sgp/crs/misc/R41419.pdf. Accessed: 2016-01-05. 3

[17] P. Peerani, A. Tomanin, S. Pozzi, J. Dolan, E. Miller, M. Flaska, M. Battaglieri, R. De Vita, L. Ficini, G. Ottonello, G. Ricco, G. Dermody, and C. Giles. Testing on novel neutron detectors as alternative to $^3$He for security applications. *Nuclear Instruments and Methods in Physics Research Section A: Accelerators, Spectrometers, Detectors and Associated Equipment*, 696:110–120, December 2012. 3, 23, 24, 43, 110

[18] ICRP. The 2007 Recommendations of the International Commission on Radiological Protection. *Annals of the ICRP*, 37(2-4):49–79, 2007. xii, xiv, 4, 19, 20, 38, 69

[19] D.J. Thomas. The system of radiation protection for neutrons: does it fit the purpose? *Radiation Protection Dosimetry*, 161(1-4):3–10, October 2014. 4, 22, 128

[20] K.A.A. Gamage, M.J. Joyce, and N.P. Hawkes. A comparison of four different digital algorithms for pulse-shape discrimination in fast scintillators. *Nuclear Instruments and Methods in Physics Research Section A: Accelerators, Spectrometers, Detectors and Associated Equipment*, 642(1):78–83, June 2011. 5, 115

[21] I.A. Pawełczak, A.M. Glenn, H.P. Martinez, M.L. Carman, N.P. Zaitseva, and S.A. Payne. Boron-loaded plastic scintillator with neutron-$\gamma$ pulse shape discrimination capability. *Nuclear Instruments and Methods in Physics Research Section A: Accelerators, Spectrometers, Detectors and Associated Equipment*, 751:62–69, July 2014. 6, 125, 155

[22] C.M. Whitney, L. Soundara-Pandian, E.B. Johnson, S. Vogel, B. Vinci, M. Squillante, J. Glodo, and J.F. Christian. Gamma-neutron imaging system utilizing pulse shape discrimination with CLYC. *Nuclear Instruments and Methods in Physics Research Section A: Accelerators, Spectrometers, Detectors and Associated Equipment*, 784:346–351, June 2015. 6, 125

[23] A beginner's guide to uncertainty of measurement. https://www.wmo.int/pages/prog/gcos/documents/gruanmanuals/UK_NPL/mgpg11.pdf. Accessed: 2016-01-05. 8

[24] G.C. Chikkur and N. Umakantha. A new method of determining the compton edge in liquid scintillator. *Nuclear Instruments and Methods*, 107(1):201–202, February 1973. 13

[25] R.D. Evans. *The atomic nucleus*, page 712. McGraw-Hill Book Company Inc., New York, 1955. xii, 13

[26] N.J Carron. *An Introduction to the Passage of Energetic Particles through Matter*, page 308. CRC Press, Boca Raton, 2006. xxi, 14

[27] D. Reilly, N. Ensslin, H. Smith, Los Alamos National Laboratory, and U.S. Nuclear Regulatory Commission. Office of Nuclear Regulatory Research. *Passive Nondestructive Assay of Nuclear Materials*, page 360. NUREG-CR. The Commission, Washington, USA, 1991. xxi, 14

[28] ICRU. Quantities and Units in Radiation Protection Dosimetry. *ICRU Publications: Bethesda*, Report 51, 1993. 18, 19, 22

[29] ICRP. The 1990 Recommendations of the International Commission on Radiological Protection. *Annals of the ICRP*, 21(1-3), 1991. xxi, 20

[30] ICRP. Conversion Coefficients for use in Radiological Protection against External Radiation. *Annals of the ICRP*, 26(3-4):35–81, 1996. xii, xxii, 21, 22, 127, 128, 152, 161, 163

[31] N. Petoussi-Henss, W.E. Bolch, K.F. Eckerman, A. Endo, N. Hertel, J. Hunt, M. Pelliccioni, H. Schlattl, and M. Zankl. ICRP 116 - conversion coefficients for radiological protection quantities for external radiation exposures. *Annals of the ICRP*, 40(2):1–257, 2010. 22, 128

[32] G.F. Knoll. *Radiation detection and measurement, 4th Edition.* John Wiley & Sons, 2010. 23, 88

[33] J.M. Bordy, T. Lahaye, F. Landre, C. Hoflack, S. Lequin, and J. Barthe. Single Diode Detector for Individual Neutron Dosimetry using a Pulse Shape Analysis. *Radiation Protection Dosimetry*, 70(1-4):73–78, April 1997. 24

[34] S. Pospisil, B. Sopko, E. Havránková, Z. Janout, J. Konicek, I. Mácha, and J. Pavlu. Si Diode as a Small Detector of Slow Neutrons. *Radiation Protection Dosimetry*, 46(2):115–118, February 1993. 24

[35] C. Petrillo, F. Sacchetti, O. Toker, and N.J. Rhodes. Solid state neutron detectors. *Nuclear Instruments and Methods in Physics Research Section A: Accelerators, Spectrometers, Detectors and Associated Equipment*, 378(3):541–551, August 1996. 24

[36] J.K. Shultis and D.S. McGregor. Efficiencies of coated and perforated semiconductor neutron detectors. *IEEE Transactions on Nuclear Science*, 53(3):1659–1665, June 2006. 24

[37] D.S. McGregor, S.L. Bellinger, and J.K. Shultis. Present status of microstructured semiconductor neutron detectors. *Journal of Crystal Growth*, 379:99–110, September 2013. 24

[38] A.N. Caruso. The physics of solid-state neutron detector materials and geometries. *Journal of Physics: Condensed Matter*, 22(44):1–32, October 2010. 24

[39] M. Awschalom and R.S. Sanna. Applications of Bonner Sphere Detectors in Neutron Field Dosimetry. *Radiation Protection Dosimetry*, 10(1-4):89–101, January 1985. 25

[40] P. Šujak, P. Čarný, Z. Prouza, and J. Hermanská. Energy Spectra of Stray Neutron Fields at PWR Nuclear Power Plants. *Radiation Protection Dosimetry*, 19(3):179–182, July 1987. 25

[41] Neutron Spektrometer NEMUS (Neutron Multisphere Spectrometer. https://www.ptb.de/cms/en/ptb/fachabteilungen/abt6/fb-64/646-neutron-spectrometry-and-neutron-sources/nemus/neutron-spektrometer-nemus-neutron-multisphere-spectrometer.html. Accessed: 2015-11-02. xii, 25

[42] S. Garny, V. Mares, and W. Rühm. Response functions of a Bonner sphere spectrometer calculated with GEANT4. *Nuclear Instruments and Methods*

*in Physics Research Section A: Accelerators, Spectrometers, Detectors and Associated Equipment*, 604(3):612–617, June 2009. xii, 26

[43] M. Matzke. Unfolding methods. *Germany: Physikalisch-Technische Bundesanstalt*, 2002. 25

[44] R. Bedogni, C. Domingo, A. Esposito, and F. Fernández. FRUIT: An operational tool for multisphere neutron spectrometry in workplaces. *Nuclear Instruments and Methods in Physics Research Section A: Accelerators, Spectrometers, Detectors and Associated Equipment*, 580(3):1301–1309, October 2007. 25

[45] J.T. Routti and J.V. Sandberg. Unfolding Activiation and Multisphere Detector Data. *Radiation Protection Dosimetry*, 10(1-4):103–110, January 1985. 25

[46] M. Matzke. The HEPROW Program System. *NEA1666/01*, 2004. 25

[47] H.R. Vega-Carrillo, J.M. Ortiz-Rodríguez, and M.R. Martínez-Blanco. NSD-UAZ unfolding package for neutron spectrometry and dosimetry with Bonner spheres. *Applied Radiation and Isotopes*, 71:87–91, December 2012. 25

[48] J.M. Ortiz-Rodríguez, A. Reyes Alfaro, A. Reyes Haro, J.M. Cervantes Viramontes, and H.R. Vega-Carrillo. A neutron spectrum unfolding computer code based on artificial neural networks. *Radiation Physics and Chemistry*, 95:428–431, February 2014. 25, 31, 131

[49] J. Yang, X.L. Luo, G.F. Liu, C.B. Lin, Y.L. Wang, Q.Q. Hu, and J.X. Peng. Digital discrimination of neutrons and $\gamma$ rays with organic scintillation detectors in an 8-bit sampling system using frequency gradient analysis. *Chinese Physics C*, 36(6):544–551, June 2012. 28, 90, 91, 92

[50] M. Flaska and S.A. Pozzi. Digital pulse shape analysis for the capture-gated liquid scintillator BC-523A. *Nuclear Instruments and Methods in Physics Research Section A: Accelerators, Spectrometers, Detectors and Associated Equipment*, 599(2-3):221–225, February 2009. 28, 90, 110

[51] S.D. Jastaniah and P.J. Sellin. Digital techniques for n/$\gamma$ pulse shape discrimination and capture-gated neutron spectroscopy using liquid scintillators. *Nuclear Instruments and Methods in Physics Research Section A: Accelerators, Spectrometers, Detectors and Associated Equipment*, 517(1-3):202–210, January 2004. 28, 90, 110

[52] G. Liu, M.D. Aspinall, X. Ma, and M.J. Joyce. An investigation of the digital discrimination of neutrons and $\gamma$-rays with organic scintillation detectors using an artificial neural network. *Nuclear Instruments and Methods in Physics Research Section A: Accelerators, Spectrometers, Detectors and Associated Equipment*, 607(3):620–628, August 2009. 28, 90, 91

[53] C. Hellesen, M. Skiba, G. Ericsson, E. Andersson Sundén, F. Binda, S. Conroy, J. Eriksson, and M. Weiszflog. Impact of digitization for timing and pulse shape analysis of scintillator detector signals. *Nuclear Instruments and Methods in Physics Research Section A: Accelerators, Spectrometers, Detectors and Associated Equipment*, 720:135–140, August 2013. 28, 106

[54] D. Cester, M. Lunardon, G. Nebbia, L. Stevanato, G. Viesti, S. Petrucci, and C. Tintori. Pulse shape discrimination with fast digitizers. *Nuclear Instruments and Methods in Physics Research Section A: Accelerators, Spectrometers, Detectors and Associated Equipment*, 748:33–38, June 2014. 28, 106

[55] R. Tessier, K. Pocek, and A. DeHon. Reconfigurable Computing Architectures. *Proceedings of the IEEE*, 103(3):332–354, March 2015. 29

[56] E.M. Becker and A.T. Farsoni. Wireless, low-cost, FPGA-based miniature gamma ray spectrometer. *Nuclear Instruments and Methods in Physics Research Section A: Accelerators, Spectrometers, Detectors and Associated Equipment*, 761:99–104, October 2014. 29

[57] R.T. Schiffer, M. Flaska, S.A. Pozzi, S. Carney, and D.D. Wentzloff. A scalable FPGA-based digitizing platform for radiation data acquisition. *Nuclear Instruments and Methods in Physics Research Section A: Accelerators, Spectrometers, Detectors and Associated Equipment*, 652(1):491–493, October 2011. 29

[58] N.V. Kornilov, V.A. Khriatchkov, M. Dunaev, A.B. Kagalenko, N.N. Semenova, V.G. Demenkov, and A.J.M. Plompen. Neutron spectroscopy with fast waveform digitizer. *Nuclear Instruments and Methods in Physics Research Section A: Accelerators, Spectrometers, Detectors and Associated Equipment*, 497(2-3):467–478, February 2003. 29

[59] M. Faisal, R.T. Schiffer, M.J. Haling, M. Flaska, S.A. Pozzi, and D.D. Wentzloff. A Data Processing System for Real-Time Pulse Processing and Timing Enhancement for Nuclear Particle Detection Systems. *IEEE Transactions on Nuclear Science*, 60(2):619–623, April 2013. 29

[60] J.M. Cardoso, J.B. Simoes, C.M.B.A. Correia, A. Combo, R. Pereira, J. Sousa, N. Cruz, P. Carvalho, and C.A.F. Varandas. A high performance reconfigurable hardware platform for digital pulse processing. *IEEE Transactions on Nuclear Science*, 51(3):921–925, June 2004. 29

[61] A. Pullia and R. Grimoldi. Design rules for optimization of digital spectrometers. In *Nuclear Science Symposium Conference Record*, volume 2, pages 1004–1008. IEEE, November 2001. 29

[62] M.J. Joyce, M. D. Aspinall, F.D. Cave, K. Georgopoulos, and Z. Jarrah. The Design, Build and Test of a Digital Analyzer for Mixed Radiation Fields. *IEEE Transactions on Nuclear Science*, 57(5):2625–2630, October 2010. 29

[63] C.M. Bishop. *Pattern recognition and machine learning*. Springer, New York, 2006. xiii, 31, 32, 116

[64] R. Koohi-Fayegh, S. Green, N.M.J. Crout, G.C. Taylor, and M.C. Scott. Neural network unfolding of photon and neutron spectra using an NE-213 scintillation detector. *Nuclear Instruments and Methods in Physics Research Section A: Accelerators, Spectrometers, Detectors and Associated Equipment*, 329(1-2):269–276, May 1993. 31, 131

[65] M.R. Kardan, S. Setayeshi, R. Koohi-Fayegh, and M. Ghiassi-Nejad. Neutron spectra unfolding in Bonner spheres spectrometry using neural networks. *Radiation Protection Dosimetry*, 104(1):27–30, April 2003. 31, 131

[66] S. Avdic, S.A. Pozzi, and V. Protopopescu. Detector response unfolding using artificial neural networks. *Nuclear Instruments and Methods in Physics Research Section A: Accelerators, Spectrometers, Detectors and Associated Equipment*, 565(2):742–752, September 2006. 31, 131

[67] A. Sharghi Ido, M.R. Bonyadi, G.R. Etaati, and M. Shahriari. Unfolding the neutron spectrum of a NE213 scintillator using artificial neural networks. *Applied Radiation and Isotopes*, 67(10):1912–1918, October 2009. 31, 131

[68] Q. Zhu, F. Song, J. Ren, X. Chen, and B. Zhou. The criteria for selecting a method for unfolding neutron spectra based on the information entropy theory. *Radiation Measurements*, 62:22–27, March 2014. 31

[69] R. Hecht-Nielsen. Theory of the backpropagation neural network. In *International Joint Conference on Neural Networks, 1989. IJCNN*, pages 593–605. IEEE, 1989. 31, 76

[70] G Bertuccio and A. Pullia. A method for the determination of the noise parameters in preamplifying systems for semiconductor radiation detectors. *Review of Scientific Instruments.*, 64(11):3294–3298, November 1993. 33

[71] V.T. Jordanov and G.F. Knoll. Digital pulse-shape analyzer based on fast sampling of an integrated charge pulse. *IEEE Transactions on Nuclear Science*, 42(4):683–687, August 1995. 34

[72] S. Marrone, D. Cano-Ott, N. Colonna, C. Domingo, F. Gramegna, E.M. Gonzalez, F. Gunsing, M. Heil, F. Käppeler, P.F. Mastinu, P.M. Milazzo, T. Papaevangelou, P. Pavlopoulos, R. Plag, R. Reifarth, G. Tagliente, J.L. Tain, and K. Wisshak. Pulse shape analysis of liquid scintillators for neutron studies. *Nuclear Instruments and Methods in Physics Research Section A: Accelerators, Spectrometers, Detectors and Associated Equipment*, 490(1–2):299–307, September 2002. xiii, 34, 35, 91

[73] M.D. Aspinall, B. D'Mellow, R.O. Mackin, M.J. Joyce, Z. Jarrah, and A.J. Peyton. The empirical characterization of organic liquid scintillation detectors by the normalized average of digitized pulse shapes. *Nuclear Instruments and*

*Methods in Physics Research Section A: Accelerators, Spectrometers, Detectors and Associated Equipment*, 578(1):261–266, July 2007. xiii, 34, 35

[74] M Nakhostin. A new digital method for high precision neutron-gamma discrimination with liquid scintillation detectors. *Journal of Instrumentation*, 8(05):1–11, May 2013. 35, 91, 100

[75] J. Kamleitner, S. Coda, S. Gnesin, and Ph. Marmillod. Comparative analysis of digital pulse processing methods at high count rates. *Nuclear Instruments and Methods in Physics Research Section A: Accelerators, Spectrometers, Detectors and Associated Equipment*, 736:88–98, February 2014. 35, 107

[76] D.T. Bartlett, P. Drake, F. d'Errico, M. Luszik-Bhadra, M. Matzke, and R.J. Tanner. The importance of the direction distribution of neutron fluence, and methods of determination. *Nuclear Instruments and Methods in Physics Research Section A: Accelerators, Spectrometers, Detectors and Associated Equipment*, 476(1-2):386–394, January 2002. 38, 52, 152

[77] F. d'Errico, A. Di Fulvio, M. Maryañski, S. Selici, and M. Torrigiani. Optical readout of superheated emulsions. *Radiation Measurements*, 43(2-6):432–436, February 2008. xiii, 42

[78] F. d'Errico and A. Di Fulvio. Superheated emulsions for the detection of special nuclear material. *Radiation Measurements*, 46(12):1690–1693, December 2011. 43

[79] D.T. Bartlett, R.J. Tanner, and D.G. Jones. A new design of neutron dose equivalent survey instrument. *Radiation protection dosimetry*, 74(4):267–271, December 1997. 43

[80] S.D. Monk, M.J. Joyce, Z. Jarrah, D. King, and M. Oppenheim. A portable energy-sensitive cosmic neutron detection instrument. *Review of Scientific Instruments*, 79(2):023301–8, February 2008. 43

[81] M.J. Selwood and S.D. Monk. Development of a portable isotropic neutron spectrometer. *Applied Radiation and Isotopes*, 70(7):1145–1149, July 2012. 43

[82] J.M. Gómez-Ros, R. Bedogni, I. Palermo, A. Esposito, A. Delgado, M. Angelone, and M. Pillon. Design and validation of a photon insensitive multidetector neutron spectrometer based on dysprosium activation foils. *Radiation Measurements*, 46(12):1712–1715, December 2011. 43

[83] J.M. Gómez-Ros, R. Bedogni, M. Moraleda, A. Delgado, A. Romero, and A. Esposito. A multi-detector neutron spectrometer with nearly isotropic response for environmental and workplace monitoring. *Nuclear Instruments and Methods in Physics Research Section A: Accelerators, Spectrometers, Detectors and Associated Equipment*, 613(1):127–133, January 2010. 43

[84] G.C. Taylor. Design of a direction-dependent neutron dosimeter. *Radiation Measurements*, 45(10):1301–1304, December 2010. 44, 46, 52, 70, 129, 150

[85] J. Iwanowska, L. Swiderski, and M. Moszynski. Liquid scintillators and composites in fast neutron detection. *Journal of Instrumentation*, 7(04):C04004:1–9, April 2012. 45

[86] L. Swiderski, M. Moszynski, D. Wolski, T. Batsch, A. Nassalski, A. Syntfeld-Kazuch, T. Szczesniak, F. Kniest, M. R. Kusner, G. Pausch, J. Stein, and W. Klamra. Boron-10 loaded BC523A liquid scintillator for neutron detection in the border monitoring. *IEEE Transactions on Nuclear Science*, 55(6):3710–3716, December 2008. 45, 52, 110

[87] J. Glodo, R. Hawrami, and K.S. Shah. Development of Cs2LiYCl6 Scintillator. *Journal of Crystal Growth*, 379:73–78, September 2013. 45, 52, 155

[88] A General Monte Carlo N-Particle Transport Code, version 5. 45, 56, 73, 112, 129

[89] P. Ramachandran and G. Varoquaux. Mayavi: 3D Visualization of Scientific Data. *Computing in Science & Engineering*, 13(2):40–51, April 2011. xiv, 47, 71

[90] M.J.I. Balmer, K.A.A. Gamage, and G.C. Taylor. Critical review of directional neutron survey meters. *Nuclear Instruments and Methods in Physics Research*

*Section A: Accelerators, Spectrometers, Detectors and Associated Equipment*, 735:7–11, January 2014. 52, 63, 74, 79, 129

[91] C.W.E van Eijk. Inorganic scintillators for thermal neutron detection. *IEEE Transactions on Nuclear Science*, 59(5):2242–2247, October 2012. 52

[92] B. Ayaz-Maierhafer, J.P. Hayward, K.P. Ziock, M.A. Blackston, and L. Fabris. Transmission and signal loss in mask designs for a dual neutron and gamma imager applied to mobile standoff detection. *Nuclear Instruments and Methods in Physics Research Section A: Accelerators, Spectrometers, Detectors and Associated Equipment*, 712:1–8, June 2013. 52

[93] R.D. Breukers, C.M. Bartle, and A. Edgar. Transparent lithium loaded plastic scintillators for thermal neutron detection. *Nuclear Instruments and Methods in Physics Research Section A: Accelerators, Spectrometers, Detectors and Associated Equipment*, 701:58–61, February 2013. 53

[94] L. Swiderski, M. Moszynski, D. Wolski, T. Batsch, J. Iwanowska, A. Nassalski, A. Syntfeld-Kazuch, T. Szczesniak, F. Kniest, M.R. Kusner, G. Pausch, J. Stein, W. Klamra, P. Schotanus, and C. Hurlbut. Further Study of Boron-10 Loaded Liquid Scintillators for Detection of Fast and Thermal Neutrons. *IEEE Transactions on Nuclear Science*, 57(1):375–380, February 2010. 54, 110

[95] S.C. Wang, C.C. Hsu, R.W.S. Leung, S.L. Wang, C.Y. Chang, C.P. Chen, K.C. Cheng, T.I. Ho, W.P. Lai, H.M. Liu, Z.P. Mao, I.C. Shih, and Z.Q. Wong, H.T. and.Yu. A feasibility study of boron-loaded liquid scintillator for the detection of electron anti-neutrinos. *Nuclear Instruments and Methods in Physics Research Section A: Accelerators, Spectrometers, Detectors and Associated Equipment*, 432(1):111–121, August 1999. 54, 61

[96] B.M. Fisher, J.N. Abdurashitov, K.J. Coakley, V.N. Gavrin, D.M. Gilliam, J.S. Nico, A.A. Shikhin, A.K. Thompson, D.F. Vecchia, and V.E. Yants. Fast neutron detection with $^{6}$Li-loaded liquid scintillator. *Nuclear Instruments and Methods in Physics Research Section A: Accelerators, Spectrometers, Detectors and Associated Equipment*, 646(1):126–134, August 2011. 55

[97] C.D. Bass, E.J. Beise, H. Breuer, C.R. Heimbach, T.J. Langford, and J.S. Nico. Characterization of a $^{6}$Li-loaded liquid organic scintillator for fast neutron spectrometry and thermal neutron detection. *Applied Radiation and Isotopes*, 77:130–138, July 2013. 55, 62, 72

[98] J. Allison, K. Amako, J. Apostolakis, H. Araujo, P.A. Dubois, M. Asai, G. Barrand, R. Capra, S. Chauvie, R. Chytracek, G.A.P. Cirrone, G. Cooperman, G. Cosmo, G. Cuttone, G.G. Daquino, M. Donszelmann, M. Dressel, G. Folger, F. Foppiano, J. Generowicz, V. Grichine, S. Guatelli, P. Gumplinger, A. Heikkinen, I. Hrivnacova, A. Howard, S. Incerti, V. Ivanchenko, T. Johnson, F. Jones, T. Koi, R. Kokoulin, M. Kossov, H. Kurashige, V. Lara, S. Larsson, F. Lei, O. Link, F. Longo, M. Maire, A. Mantero, B. Mascialino, I. McLaren, P.M. Lorenzo, K. Minamimoto, K. Murakami, P. Nieminen, L. Pandola, S. Parlati, L. Peralta, J. Perl, A. Pfeiffer, M.G. Pia, A. Ribon, P. Rodrigues, G. Russo, S. Sadilov, G. Santin, T. Sasaki, D. Smith, N. Starkov, S. Tanaka, E. Tcherniaev, B. Tome, A. Trindade, P. Truscott, L. Urban, M. Verderi, A. Walkden, J.P. Wellisch, D.C. Williams, D. Wright, and H. Yoshida. Geant4 developments and applications. *IEEE Transactions on Nuclear Science*, 53(1):270–278, February 2006. 56, 74

[99] S. Agostinelli, J. Allison, K. Amako, J. Apostolakis, H. Araujo, P. Arce, M. Asai, D. Axen, S. Banerjee, G. Barrand, F. Behner, L. Bellagamba, J. Boudreau, L. Broglia, A. Brunengo, H. Burkhardt, S. Chauvie, J. Chuma, R. Chytracek, G. Cooperman, G. Cosmo, P. Degtyarenko, A. Dell'Acqua, G. Depaola, D. Dietrich, R. Enami, A. Feliciello, C. Ferguson, H. Fesefeldt, G. Folger, F. Foppiano, A. Forti, S. Garelli, S. Giani, R. Giannitrapani, D. Gibin, J.J. Gómez Cadenas, I. González, G. Gracia Abril, G. Greeniaus, W. Greiner, V. Grichine, A. Grossheim, S. Guatelli, P. Gumplinger, R. Hamatsu, K. Hashimoto, H. Hasui, A. Heikkinen, A. Howard, V. Ivanchenko, A. Johnson, F.W. Jones, J. Kallenbach, N. Kanaya, M. Kawabata, Y. Kawabata, M. Kawaguti, S. Kelner, P. Kent, A. Kimura, T. Kodama, R. Kokoulin, M. Kossov, H. Kurashige, E. Lamanna, T. Lampén, V. Lara, V. Lefebure, F. Lei, M. Liendl, W. Lockman, F. Longo, S. Magni, M. Maire, E. Medernach, K. Minamimoto, P. Mora de Freitas, Y. Morita,

K. Murakami, M. Nagamatu, R. Nartallo, P. Nieminen, T. Nishimura, K. Ohtsubo, M. Okamura, S. O'Neale, Y. Oohata, K. Paech, J. Perl, A. Pfeiffer, M.G. Pia, F. Ranjard, A. Rybin, S. Sadilov, E. Di Salvo, G. Santin, T. Sasaki, N. Savvas, Y. Sawada, S. Scherer, S. Sei, V. Sirotenko, D. Smith, N. Starkov, H. Stoecker, J. Sulkimo, M. Takahata, S. Tanaka, E. Tcherniaev, E. Safai Tehrani, M. Tropeano, P. Truscott, H. Uno, L. Urban, P. Urban, M. Verderi, A. Walkden, W. Wander, H. Weber, J.P. Wellisch, T. Wenaus, D.C. Williams, D. Wright, T. Yamada, H. Yoshida, and D. Zschiesche. Geant4 - a simulation toolkit. *Nuclear Instruments and Methods in Physics Research Section A: Accelerators, Spectrometers, Detectors and Associated Equipment*, 506(3):250–303, July 2003. 56, 74

[100] S.F. Naeem, S.D. Clarke, and S.A. Pozzi. Validation of Geant4 and MCNPX-PoliMi simulations of fast neutron detection with the EJ-309 liquid scintillator. *Nuclear Instruments and Methods in Physics Research Section A: Accelerators, Spectrometers, Detectors and Associated Equipment*, 714:98–104, June 2013. 56

[101] N. Patronis, M. Kokkoris, D. Giantsoudi, G. Perdikakis, C.T. Papadopoulos, and R. Vlastou. Aspects of GEANT4 Monte-Carlo calculations of the BC501A neutron detector. *Nuclear Instruments and Methods in Physics Research Section A: Accelerators, Spectrometers, Detectors and Associated Equipment*, 578(1):351–355, July 2007. 56

[102] C Guardiola, K Amgarou, F García, C Fleta, D Quirion, and M Lozano. Geant4 and MCNPX simulations of thermal neutron detection with planar silicon detectors. *Journal of Instrumentation*, 6(09):T09001–15, September 2011. 56, 62, 64

[103] H.Y. Xing, L. Wang, J.J. Zhu, C.J. Tang, and Q. Yue. Simulation of large-scale fast neutron liquid scintillation detector. *Chinese Physics C*, 37(2):026003–1–8, February 2013. 62

[104] M.J.I Balmer, K.A.A Gamage, and G.C. Taylor. An investigation into a suitable scintillator for localising neutron capture within a detector. *Journal of Instrumentation*, 9(01):P01007–1–13, January 2014. 71, 74

[105] S. Nissen. Implementation of a Fast Artificial Neural Network library (FANN), 2003. 76, 132

[106] M. Riedmiller and H. Braun. A direct adaptive method for faster backpropagation learning: The RPROP algorithm. In *IEEE International Conference on Neural Networks, 1993*, pages 586–591. IEEE, 1993. 78, 132

[107] N. Zaitseva, A. Glenn, H. Paul Martinez, L. Carman, I. Pawełczak, M. Faust, and S. Payne. Pulse shape discrimination with lithium-containing organic scintillators. *Nuclear Instruments and Methods in Physics Research Section A: Accelerators, Spectrometers, Detectors and Associated Equipment*, 729:747–754, November 2013. xv, 88, 89, 92, 93, 111, 114, 129, 133

[108] F.D. Brooks. A scintillation counter with neutron and gamma-ray discriminators. *Nuclear Instruments and Methods*, 4(3):151–163, April 1959. 90

[109] T.K. Alexander and F.S. Goulding. An amplitude-insensitive system that distinguishes pulses of different shapes. *Nuclear Instruments and Methods*, 13:244–246, October 1961. 90, 114, 133

[110] M.L. Roush, M.A. Wilson, and W.F. Hornyak. Pulse shape discrimination. *Nuclear Instruments and Methods*, 31(1):112–124, December 1964. 90

[111] M. Nakhostin. Recursive algorithms for digital implementation of neutron/gamma discrimination in liquid scintillation detectors. *Nuclear Instruments and Methods in Physics Research Section A: Accelerators, Spectrometers, Detectors and Associated Equipment*, 672:1–5, April 2012. 90, 97

[112] B. D'Mellow, M.D. Aspinall, R.O. Mackin, M.J. Joyce, and A.J. Peyton. Digital discrimination of neutrons and $\gamma$-rays in liquid scintillators using pulse gradient analysis. *Nuclear Instruments and Methods in Physics Research Section A: Accelerators, Spectrometers, Detectors and Associated Equipment*, 578(1):191–197, July 2007. 90

[113] N.P. Hawkes, K.A.A. Gamage, and G.C. Taylor. Digital approaches to field neutron spectrometry. *Radiation Measurements*, 45(10):1305–1308, December 2010. 91

[114] T. Tambouratzis, D. Chernikova, and I. Pazsit. A comparison of artificial neural network performance: The case of neutron/gamma pulse shape discrimination. In *2013 IEEE Symposium on Computational Intelligence for Security and Defense Applications (CISDA)*, pages 88–95, 2013. 91

[115] T.S. Sanderson, C.D. Scott, M. Flaska, J.K. Polack, and S.A. Pozzi. Machine learning for digital pulse shape discrimination. In *Nuclear Science Symposium and Medical Imaging Conference (NSS/MIC), 2012 IEEE*, pages 199–202. IEEE, 2012. 91

[116] D. Savran, B. Löher, M. Miklavec, and M. Vencelj. Pulse shape classification in liquid scintillators using the fuzzy c-means algorithm. *Nuclear Instruments and Methods in Physics Research Section A: Accelerators, Spectrometers, Detectors and Associated Equipment*, 624(3):675–683, December 2010. 91

[117] S.D. Ambers, M. Flaska, and S.A. Pozzi. A hybrid pulse shape discrimination technique with enhanced performance at neutron energies below 500 kev. *Nuclear Instruments and Methods in Physics Research Section A: Accelerators, Spectrometers, Detectors and Associated Equipment*, 638(1):116–121, May 2011. 91

[118] V. Esmaeili-sani, A. Moussavi-zarandi, N. Akbar-ashrafi, B. Boghrati, and H. Afarideh. Neutron-gamma discrimination based on bipolar trapezoidal pulse shaping using FPGAs in NE213. *Nuclear Instruments and Methods in Physics Research Section A: Accelerators, Spectrometers, Detectors and Associated Equipment*, 694:113–118, December 2012. 91

[119] S. Li, X. Xu, H. Cao, G. Yuan, Q. Yang, and Z. Yin. A real-time n/$\gamma$ digital pulse shape discriminator based on FPGA. *Applied Radiation and Isotopes*, 72:30–34, February 2013. 91

[120] D.I. Shippen, M.J. Joyce, and M.D. Aspinall. A wavelet packet transform inspired method of neutron-gamma discrimination. *IEEE Transactions on Nuclear Science*, 57(5):2617–2624, October 2010. 91

[121] G. Liu, J. Yang, X.L. Luo, C.B. Lin, J.X. Peng, and Y. Yang. A comparison of different discrimination parameters for the DFT-based PSD method in fast scintillators. *Radiation Measurements*, 58:12–17, November 2013. 91, 92

[122] S. Yousefi, L. Lucchese, and M.D. Aspinall. Digital discrimination of neutrons and gamma-rays in liquid scintillators using wavelets. *Nuclear Instruments and Methods in Physics Research Section A: Accelerators, Spectrometers, Detectors and Associated Equipment*, 598(2):551–555, January 2009. 91, 92

[123] X.L. Luo, Y.K Wang, J. Yang, G. Liu, C.B. Lin, Q.Q. Hu, and J.X. Peng. Neutron/gamma discrimination employing the power spectrum analysis of the signal from the liquid scintillator BC501A. *Nuclear Instruments and Methods in Physics Research Section A: Accelerators, Spectrometers, Detectors and Associated Equipment*, 717:44–50, July 2013. 92

[124] F. Pedregosa, G. Varoquaux, A. Gramfort, V. Michel, B. Thirion, O. Grisel, M. Blondel, P. Prettenhofer, R. Weiss, V. Dubourg, J. Vanderplas, A. Passos, D. Cournapeau, M. Brucher, M. Perrot, and E. Duchesnay. Scikit-learn: Machine Learning in Python. *Journal of Machine Learning Research*, 12:2825–2830, October 2011. 94

[125] A.A. Naqvi, H. Al-Juwair, and K. Gul. Energy resolution tests of 125 mm diameter cylindrical NE213 detector using monoenergetic gamma rays. *Nuclear Instruments and Methods in Physics Research Section A: Accelerators, Spectrometers, Detectors and Associated Equipment*, 306(1-2):267–271, August 1991. 96

[126] M.U.A. Bromba and H. Ziegler. Application hints for Savitzky-Golay digital smoothing filters. *Analytical Chemistry*, 53(11):1583–1586, September 1981. 100

[127] G. Liu, M.J. Joyce, X. Ma, and M.D. Aspinall. A digital method for the discrimination of neutrons and $\gamma$ rays with organic scintillation detectors using frequency gradient analysis. *IEEE Transactions on Nuclear Science*, 57(3):1682–1691, June 2010. 103

[128] G.F. Liu, X.L. Luo, J. Yang, C.B. Lin, Q.Q. Hu, and J.X. Peng. Baseline drift effect on the performance of neutron and $\gamma$ ray discrimination using frequency gradient analysis. *Chinese Physics C*, 37(6):066201–14, June 2013. 103

[129] J.D. Hunter. Matplotlib: A 2D graphics environment. *Computing in Science and Engineering*, 9(3):90–95, June 2007. 107, 125, 149

[130] Y.H. Chen, X.M. Chen, X.D. Zhang, J.R. Lei, L. An, J.X. Shao, P. Zheng, X.H. Wang, C.X. Zhu, T. He, and J. Yang. Study of n-$\gamma$ discrimination in low energy range (above 40 keVee) by charge comparison method with a BC501a liquid scintillation detector. *Chinese Physics C*, 38(3):036001–5, March 2014. 109

[131] R.A. Cecil, B.D. Anderson, and R. Madey. Improved predictions of neutron detection efficiency for hydrocarbon scintillators from 1 MeV to about 300 MeV. *Nuclear Instruments and Methods*, 161(3):439–447, May 1979. 109

[132] F. Posny, J.L. Chartier, and M. Buxerolle. Neutron spectrometry system for radiation protection: Measurements at work places and in calibration fields. *Radiation Protection Dosimetry*, 44(1-4):239–242, November 1992. xvii, 109

[133] D.J. Thomas, A.J. Waker, J.B. Hunt, A.G. Bardell, and B.R. More. An intercomparison of neutron field dosimetry systems. *Radiation Protection Dosimetry*, 44(1-4):219–222, November 1992. xvii, 109

[134] S.A. Pozzi, R.B. Oberer, and J.S. Neal. Analysis of the response of capture-gated organic scintillators. *IEEE Transactions on Nuclear Science*, 52(6):3141–3146, December 2005. 110

[135] P. Holm, K. Peräjärvi, S. Ristkari, T. Siiskonen, and H. Toivonen. A capture-gated neutron spectrometer for characterization of neutron sources and their shields. *Nuclear Instruments and Methods in Physics Research Section A: Accelerators, Spectrometers, Detectors and Associated Equipment*, 751:48–54, July 2014. 110

[136] F. Pino, L. Stevanato, D. Cester, G. Nebbia, L. Sajo-Bohus, and G. Viesti. Detecting fast and thermal neutrons with a boron loaded liquid scintillator, EJ-339A. *Applied Radiation and Isotopes*, 92:6–11, September 2014. 110

[137] N.S. Bowden, M. Sweany, and S. Dazeley. A note on neutron capture correlation signals, backgrounds, and efficiencies. *Nuclear Instruments and Methods in Physics Research Section A: Accelerators, Spectrometers, Detectors and Associated Equipment*, 693:209–214, November 2012. 113

[138] A.P Dempster, N.M Laird, and D.B Rubin. Maximum Likelihood from Incomplete Data via the EM Algorithm. *Journal of the Royal Statistical Society. Series B (Methodological)*, 39(1):1–38, 1977. 116

[139] M.J.I. Balmer, K.A.A. Gamage, and G.C. Taylor. doi:10.17635/lancaster/researchdata/7. 125

[140] M.J.I. Balmer, K.A.A. Gamage, and G.C. Taylor. Neutron assay in mixed radiation fields with a $^{6}$Li-loaded plastic scintillator. *Journal of Instrumentation*, 10(08):P08012–1–14, August 2015. 129, 133, 135, 142

[141] M.J.I. Balmer, K.A.A. Gamage, and G.C. Taylor. Detecting energy dependent neutron capture distributions in a liquid scintillator. *Nuclear Instruments and Methods in Physics Research Section A: Accelerators, Spectrometers, Detectors and Associated Equipment*, 776:1–7, March 2015. 129

[142] Computerized man model. http://cmpwg.ans.org/phantoms.html. Accessed: 2015-11-23. 130

[143] M.J.I. Balmer, K.A.A. Gamage, and G.C. Taylor. doi:10.17635/lancaster/researchdata/56. 131, 138, 141, 149

[144] O.F. Naismith and D.J. Thomas. MCNP Calculation of Neutron Scatter in the Main Bay of the Chadwick Building, NPL. *NPL Report - CIRA004*, 1996. 131

[145] G.C. Taylor and D.J. Thomas. Neutron scatter characteristics of the low-scatter facility of the Chadwick Building, NPL. *NPL Report - CIRM17*, 1998. 131

[146] ICRU. Microdosimetry - ICRU report 36. *International Commission on Radiation Units and Measurements - report 36*, 1983. 131

[147] C. Igel and M. Hüsken. Empirical evaluation of the improved rprop learning algorithms. *Neurocomputing*, 50:105–123, 2003. 132

[148] A.N. Mabe, A.M. Glenn, M. Leslie Carman, N.P. Zaitseva, and S.A. Payne. Transparent plastic scintillators for neutron detection based on lithium salicylate. *Nuclear Instruments and Methods in Physics Research Section A: Accelerators, Spectrometers, Detectors and Associated Equipment*, 806:80–86, January 2016. 155

[149] R. Preston, J.E. Eberhardt, R. Bencardino, and J. Tickner. Software-based digital pulse processing for silicon photomultiplier radiation detectors. In *Nuclear Science Symposium and Medical Imaging Conference (NSS/MIC), 2012 IEEE*, pages 462–467. IEEE, 2012. 156

[150] R.M. Preston, J.E. Eberhardt, and J.R. Tickner. Neutron generator burst timing measured using a pulse shape discrimination plastic scintillator with silicon photomultiplier readout. *Journal of Instrumentation*, 8(12):P12005–1–12, December 2013. 156

[151] B.S. Budden, A.J. Couture, L.C. Stonehill, A.V. Klimenko, J.R. Terry, and J.O. Perry. Analysis of Cs2LiYCl6:$Ce^{3+}$(CLYC) waveforms as read out by solid state photomultipliers. In *Nuclear Science Symposium and Medical Imaging Conference (NSS/MIC), 2012 IEEE*, pages 347–350. IEEE, 2012. 156

[152] De2-115 manual. ftp://ftp.altera.com/up/pub/.../DE2-115/DE2_115_User_Manual.pdf. Accessed: 2015-12-14. 164

[153] Ftdi um232h. http://www.ftdichip.com/Support/Documents/DataSheets/Modules/DS_UM232H.pdf. Accessed: 2015-12-14. xx, 165

[154] De2-115 manual. https://www.altera.com/en_US/pdfs/literature/manual/rm_data_conversion_hsmc.pdf. Accessed: 2015-12-14. xx, 165, 166